Spin and correlation induced effects in mesoscopic transport and noise

Dissertation
zur Erlangung des Doktorgrades
des Fachbereichs Physik
der Universität Hamburg

vorgelegt von

Fabio Cavaliere

aus Genova (Italien)

Hamburg
2005

Abstract

In this thesis, we will investigate the role of spin, interactions and orbital degrees of freedom in the transport properties of quantum dots and quantum rings created in correlated one-dimensional electron systems. The description of these systems will employ the Luttinger liquid model for interacting electrons in one dimension. The tunneling will be modeled with the aid of the Bosonization technique. The current and noise will be analyzed in the sequential tunneling regime using a master equation formalism. Several results will be discussed.

We firstly deal with the transport properties of a one-dimensional quantum dot. In the linear regime, a spin-induced even-odd effect in the conductance peaks position is found for zero-temperature. Increasing the latter, the peaks positions shift until, in the high temperature regime, a uniform spacing is found. The peak shifting is affected by interactions in the leads. A power law scaling of the linear conductance peaks, as a function of the temperature, is found: in the low temperature regime the exponent is determined by the leads interactions only, while in the high temperature regime interactions within the quantum dot lead to its renormalization. In the nonlinear transport regime a novel negative differential conductance mechanism will be discussed. We will show that this effect is induced by the peculiar non-Fermi-liquid interactions in the dot and is connected to a dynamical trapping of excited states with a high total spin which occurs when the tunneling barriers are asymmetric. The influence of spin-flip relaxation processes and interacting external leads will be studied.

Subsequently, we will study the charge- and angular momentum-resolved currents noise of a quantum ring. We will concentrate firstly on the zero-frequency regime and will show that, in an interacting ring, the charge current noise can be driven to values exceeding the Poissonian limit in the presence of asymmetric tunneling barriers. We will show that the origin of super-Poissonian charge noise is the inhomogeneity of the dot states dwell time. We will discuss the sensitivity of the noise with respect to leads interactions and point out the possibility to achieve super-Poissonian angular current noise for leads with attractive interactions. We will analyze these results with the aid of a Monte Carlo simulation and show that, in the presence of super-Poissonian charge noise, a bunching of the tunneling events occurs. The angular noise is insensitive to the bunching phenomenon. Employing an external magnetic flux piercing the ring, we will show that an interacting ring can exhibit transi-

3

tions between sub- and super-Poissonian regimes for the charge current noise, in sharp contrast with the case of a noninteracting ring.

Zusammenfassung

In dieser Arbeit untersuchen wir den Einfluß von Spin, Wechselwirkung und orbitalen Freiheitsgraden auf die Transporteigenschaften von in korrelierten eindimensionalen Elektronensystemen erzeugten Quantenpunkten und Quantenringen. Die Beschreibung dieser Systeme erfolgt im Modell der Luttiger-Flüssigkeit für wechselwirkende Elektronen in einer Dimension. Tunnelprozesse werden mit Hilfe der Bosonisierungstechnik modelliert. Strom und Rauschen untersuchen wir für den Fall von sequentiellem Tunneln unter Verwendung von Mastergleichungen. Wir diskutieren verschiedene Ergebnisse.

Zunächst behandeln wir Transporteigenschaften eines eindimensionalen Quantenpunktes. Wir finden bei Temperatur $T = 0$ im linearen Bereich einen spininduzierten "even-odd"-Effekt in den Peak-Positionen des Leitwerts. Bei Temperaturerhöhung verschieben sich die Peak-Positionen, bis sich im Bereich hoher Temperaturen ein einheitlicher Abstand einstellt. Diese Verschiebung wird von Wechselwirkungen in den Zuleitungen beeinflusst. Wir beobachten, dass die linearen Leitwert-Peaks als Funktion der Temperatur gemäß eines Potenzgesetzes skalieren: Im Bereich niedriger Temperaturen ist der Exponent allein durch die Wechselwirkungen in den Zuleitungen bestimmt, während im Bereich hoher Temperaturen Wechselwirkungen innerhalb des Quantenpunktes den Exponenten renormieren.

Im nichtlinearen Transportregime diskutieren wir einen neuartigen Mechanismus, der zu einem negativen diferentiellen Leitwert führt. Wir zeigen, dass dieser Effekt durch die besonderen, nicht mit der Fermiflüssigkeitstheorie im Einklang stehenden Wechselwirkungen im Quantenpunkt erzeugt wird und einem dynamischen Einfangen von angeregten Zuständen mit hohem Gesamtspin entspricht, das bei asymmetrischen Tunnelbarrieren auftritt. Weiterhin untersuchen wir den Einfluss von Spinflip-Relaxationsprozessen und wechselwirkenden externen Zuleitungen.

Desweiteren studieren wir das Rauschen von Ladungs- und drehimpulsaufgelösten Strömen in einem Quantenring. Dabei konzentrieren wir uns zunächst auf das statische Regime und zeigen, dass in einem wechselwirkendem Ring mit asymmetrischen Tunnelbarrieren das Rauschen des Ladungsstroms die Poissonverteilung überschreitende ("super-Poissonian") Werte annehmen kann. Ursache dafür ist die inhomogene Verteilung der Verweilzeiten der Quantenpunktzustände. Wir diskutieren die Empfindlichkeit des Rauschens bezüglich der Wechselwirkungen in den Zuleitungen und zeigen die Möglichkeit auf, mit attraktiven Wechselwirkunden in den Zuleitungen auch die Poisson-

verteilung überschreitende drehimpulsaufgelöste Ströme zu erhalten.

Wir analysieren diese Ergebnisse mit einer Monte-Carlo-Simulation und zeigen für Ladungsrauschen im Bereich "super-Poissonian" das Auftreten von gebündelten Tunnelereignissen. Das Rauschen im drehimpulsaufgelösten Strom ist unabhänging von diesem Bündelungsphänomen. Durchdringt ein externer magnetischer Fluß den wechselwirkenden Ring, können Übergänge zwischen "sub-" und "super-Poissonian"-Regimes auftreten, in scharfem Gegensatz zum Verhalten im nicht-wechselwirkenden Ring.

Introduction

In one of his most famous speeches [1], Richard Patrick Feynman said: "When we get to the very, very small world – say circuits of seven atoms – we have a lot of new things that would happen that represent completely new opportunities for design. Atoms on a small scale behave like nothing on a large scale, for they satisfy the laws of quantum mechanics [...] We can use, not just circuits, but some system involving the quantized energy levels, or the interactions of quantized spin [...]". In the last twenty years, the technology employed to fabricate low-dimensional electronic systems has improved to such an extent that Feynman's predictions are becoming reality. The race to miniaturization provides some astonishing figures: nowadays ordinary personal computer parts such as CPUs have reached the impressive level of 230 millions of transistors, on a dye size of about 200 mm^2 [2]. At the same time, the physics of low-dimensional geometrically confined electron systems has achieved impressive results. It is nowadays possible to realize semiconducting heterostructures in which a two-dimensional high-mobility electron gas is created. In these systems, the discovery of the integer [3] and of the fractional [4] Hall effects has been made. By employing electrostatically biased metallic gates or chemical etching, it is possible to shape the 2DEG in order to create narrow one dimensional channels called quantum wires [5], or even small islands of electrons, confined in all the three dimensions, called quantum dots [6]. Quantum wires exhibit a strongly nonlinear, step-like current-voltage curve: in these systems the conductance is quantized in integer multiples of e^2/h. In quantum dots the effects due to electronic interactions are particularly evident, for instance in the well-known Coulomb blockade effect [6,7]. Recently, novel methods have been devised to create one-dimensional electron systems. In channels created by the cleaved-edge overgrowth technique [8] and in carbon nanotubes [9], signatures of correlations beyond the Fermi liquid picture have been found. Very recently, single molecules have been contacted to metallic leads creating a quantum dot [10,11]. In all of these systems, the strong interplay of electronic interactions and the spin degree of freedom give rise to a wealth of intriguing physical effects. Among the theoretical tools devised to analyze these effects, the analysis of transport properties has clearly emerged as one of the most powerful. While the investigation of current and conductance has been the subject of in-depth studies for quite a long time, recently the noise – statistical analysis of the second moment in the current fluctuations – has attracted a considerable interest [12,13].

In this thesis we will study the interplay of electronic interactions, spin, orbital degrees of freedom and geometrical confinement in strongly correlated one-dimensional systems. We will employ the Luttinger liquid model [14], which allows to treat accurately electronic interactions in these systems, and will calculate the current and the shot noise in the sequential tunneling regime employing a master equation approach. The structure of the thesis is as follows.

Part one is divided into two chapters. In the first chapter, a short overview of some of the most important features of one-dimensional systems and quantum dots will be given. We will briefly describe carbon nanotubes and cleaved-edge overgrowth heterostructures since they represent two of the most important realizations of quantum wires. The fundamental concepts of Coulomb blockade and Coulomb oscillations will be introduced within the framework of the orthodox theory for quantum dots. This will allow us to interpret recent experimental results for quantum dots embedded in one-dimensional electronic channels.

In the second chapter, the properties of the Luttinger liquid model will be reviewed following [14]. Assuming a zero-range forward scattering, we will describe both the cases of periodic and open boundary conditions for the case of spinful and spinless electrons. The bosonization identity will be discussed as it provides a necessary tool in order to calculate the correlation functions of the Luttinger liquid.

Part two deals with the transport properties of a quantum dot embedded in a one-dimensional electron channel [15–19]. Experimental realizations of such a system are for instance described in [8, 20]. In the third chapter, a model for a spinful quantum dot embedded inside a one-dimensional channel will be described in details. The relevant energy scales will be introduced and the different kinds of excitations of the system will be discussed. The master equation for the transport in the sequential tunneling regime will be analyzed and the calculation of the transition rates within the framework of the Fermi golden rule will be set up. The case of non-relaxed collective charge and spin density waves will be introduced and some recent results [18] will be analyzed. Transition rates in the case of thermally relaxed collective modes will be derived and an extension to the master equation will be made, in order to take into account spin-flip relaxation processes.

In the fourth chapter, analytic and numerical results for the differential conductance of the one-dimensional quantum dot in the sequential tunneling regime will be presented. In the linear tunneling regime, a spin-induced even-odd effect in the conductance peaks position will be shown. The interactions-induced power law scaling of the conductance maximum will be analyzed, and the positions of the peaks as a function of the temperature will be studied. In the nonlinear regime, a spectroscopic analysis of the differential conductance behavior in the gate voltage-bias voltage plane is performed. A novel mechanism for negative differential conductance will be described. This effect will be analyzed in great detail: the role of asymmetric tunneling barriers, spin-charge separation and high-spin excited states will be discussed. Also, the influence of interacting leads and spin-flip relaxation processes will be analyzed.

Part three deals with the noise properties of a one-dimensional quantum ring [21], realized for instance as described in [22, 23]. In chapter five, a short introduction to noise in low-dimensional electron systems will be given. Partic-

ular emphasis is put on the connection between noise, statistics and Coulomb interactions. The Hanbury-Brown and Twiss experiment with photons and electrons will be sketched. Subsequently, the results of some recent studies on the noise in double-barrier systems will be reported.

In chapter six, the noise of a one-dimensional quantum ring will be discussed. The description is made in terms of a spinless Luttinger liquid in the presence of periodic boundary conditions, and the transport will be considered in the tunneling regime. The technique employed in the noise calculation will be described and some numerical and analytic results are presented. Charge- and angular-current noise will be considered. The zero-frequency regime will be addressed, studying the influence of electronic interactions on the noise both without or in the presence of an external magnetic flux. Transitions between sub- and super-Poissonian noise regimes will be discussed. The role of the typical transport time scales on the noise will be underlined, employing also a Monte Carlo simulation.

Part I

Introduction

Low dimensional systems

"I call our world Flatland, not because we call it so, but to make its nature clearer to you, my happy readers, who are privileged to live in Space."
(**E. A. Abbott**)

In this chapter, a short overview of low dimensional electronic systems will be made. After a premise on two-dimensional electronic gases (section 1.1), one-dimensional systems are described, either in the form of confined two-dimensional electron gases (section 1.2) or as carbon nanotubes (section 1.3). We then introduce quantum dots (section 1.4), discuss briefly their transport properties and describe some recent experimental result on quantum dots created in one-dimensional electron channels (section 1.5).

1.1 The two dimensional electron gas

The two dimensional electron gas has been available since about thirty years, the first realization being the inversion layers in silicon MOSFETs [24]. More recently, high quality 2DEGs are created at the interface of a GaAs/AlGaAs heterostructures. These 2DEGs show excellent properties such as extremely long mean free paths, in the range of $10 \div 100$ μm, and high mobilities (of the order of $10^6 \mathrm{cm}^2/\mathrm{sV}$). Therefore, they are ideal systems both from the point of view of applications – high speed electronics being the first candidate – and for basic research purposes. The interface between GaAs and AlGaAs is created with monolayer precision by means of molecular beam epitaxy techniques. A layer of about 100 nm of high band gap AlGaAs is grown in the z-direction ontop of the lower bandgap GaAs substrate. Subsequently, a modulation doping scheme is employed, where As atoms are substituted with Si donors. As a result, the conduction band shape near the junction plane is modified as shown in Fig. 1.1. The band structure of the 2DEG can be obtained solving self-consistently the Poisson equation for the electron sheet density. The confining potential has an almost triangular shape. Neglecting spin and electron-electron
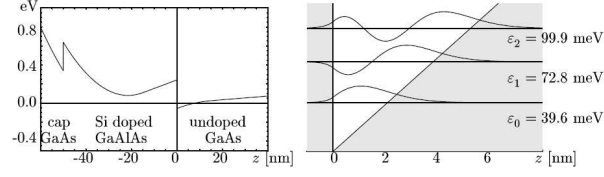
Figure 1.1: (Left) Conduction band in a GaAs/AlGaAs heterostructure. The energy is measured with respect to the Fermi level $E_{\rm F}$. (Right) Schematic depiction of the triangular potential well which develops at the interface ($z = 0$). The first three energy levels and a sketch of the corresponding wavefunctions $\zeta_n(z)$ are given. (After [25]).

interactions, the spectrum of the system can be approximated by

$$\varepsilon_{\vec{k},n} = \frac{\hbar^2}{2m^*}k^2 + \epsilon_n \tag{1.1}$$

where $m^* = 0.067 m_{\rm e}$ is the effective mass of electrons in GaAs and $\vec{k} \equiv (k_x, k_y)$. The wavefunction is given by

$$\psi_{\vec{k},n}(\vec{r}) = \frac{1}{\sqrt{A}}e^{i\vec{k}\cdot\vec{r}}\zeta_n(z)$$

where $\vec{r} \equiv (x, y)$. We have assumed the confining potential acting along the z coordinate and a free system in the (x, y) plane. The energies ϵ_n are due to the strong energy quantization imposed by the triangular well. The system effectively behaves as two-dimensional if the Fermi energy $E_{\rm F}$ is such that only the lowest subband is populated: $\epsilon_0 < E_{\rm F} < \epsilon_1$. Assuming typical parameters for GaAs/AlGaAs structures, the Fermi energy can be estimated as $E_{\rm F} \approx 10$ meV and the average level spacing is $\Delta\epsilon \approx 20$ meV [25]. Therefore, at temperatures $k_{\rm B}T < \Delta E - E_{\rm F}$, the system is effectively "frozen" in the state with $n = 0$ and we can talk about a 2DEG. Therefore, for a nowadays easily accessible temperatures $T < 100$K, a truly 2D electron system can be created.

1.2   1D electron systems

By means of an additional confinement procedure, the 2DEG can give rise to one-dimensional (1D) systems. Suppose the confinement acts on the y-direction: in general terms, still neglecting spin and electron-electron interaction, because of the external confining potential $V(y)$ the spectrum of the system develops subbands similar to (1.1)

$$\varepsilon_{k_x,n'} = \frac{\hbar^2}{2m^*}k_x^2 + \tilde{\epsilon}_{n'}. \tag{1.2}$$

The effectiveness of the confinement procedure is given by the number of populated lateral subbands, labeled by the index n'. In the extreme limit when only the subband with $n' = 0$ is occupied, the lateral degree of freedom is lost

and the system behaves as 1D. Many techniques have been employed to create 1D electron systems, employing for instance electron beam lithography and chemical etching of semiconducting GaAs/AlGaAs heterostructures.

In chemically etched heterostructures, the 2DEG is effectively cut in "slices", giving rise to a *quantum wire*. In Fig. 1.2 (left), an array of such quantum wires is
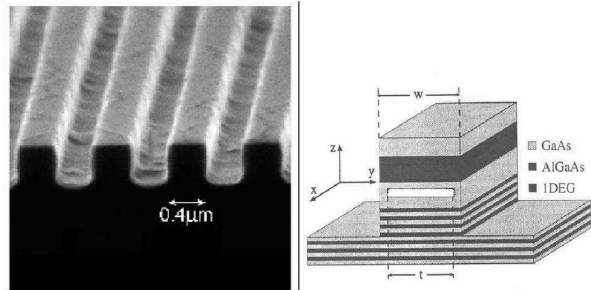
Figure 1.2: (Left panel) Chemically etched quantum wires. (Right panel) Section scheme of one quantum wire, the white rectangle represent the section of the portion of cut 2DEG. (After [5]).

shown. The 1DEG position is shown in Fig. 1.2 (right). The effectiveness of the confinement is quite good: indeed the etched pattern induces a depletion region and the real conducting width of the 1DEG, which is normally unknown, is often much smaller than external structure width. As of today, the state-of-the-art resolution allows to create channels whose external width is around 20 nm, which is often enough to reach the 1D limit at experimentally accessible temperatures. These samples are extremely useful when optical measurements have to be performed, since the large number of structures that can be stacked in an array makes it possible to obtain very high signal intensities.

Alternatively, deposing metallic gates ontop of a semiconducting heterostructure and applying suitable negative voltages on them, it is possible to deplete the 2DEG lying below the gates, thus effectively shaping the electron gas. This technique is extremely flexible, allowing to change continuously the shape of the confining potential by tuning the external voltages. Using a split-gate geometry (see Fig. 1.3) for the patterning, the first measurement of a quantized conductance for a ballistic quantum point contact (QPC) was performed in 1988 [26]. A ballistic QPC is a narrow constriction in a 2DEG, induced by the potential applied to the split-gate geometry, where the linear dimension L is smaller than the distance required to the electrons to deviate from a ballistic motion. It is possible to modify the width W of the lateral confinement tuning the voltage of the metallic gates V_g until a transversal dimension comparable with the Fermi wavelength λ_F is reached. A source-drain voltage V is then applied to the point contact to drive a current through the channel. The linear conductance $G = \lim_{V \to 0} I/V$ is then measured, as a function of V_g. The results of such an experiment are presented in Fig. 1.3, and show a clear deviation from the classical linear $I(V)$ characteristics. The conductance assumes quantized values which are multiples of the doubled conductance quantum $2e^2/h$ (e electron charge, h Planck constant). To explain this phenomenon, we can refer to (1.2). Consider the $T = 0$ case. The subband structure of the 1DEG is
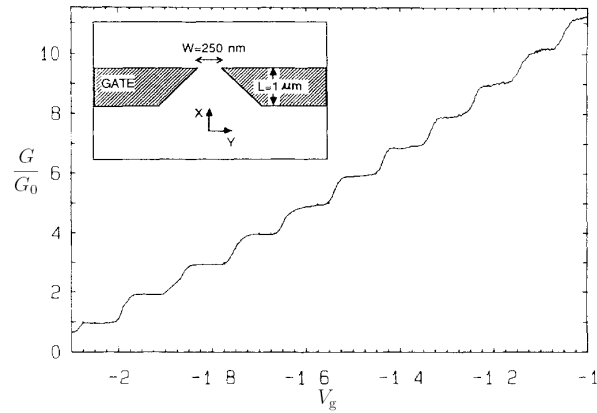
Figure 1.3: Conductance of the QPC shown in the inset, normalized to the doubled conductance quantum $2e^2/h$ (*e* electron charge, *h* Planck constant) as function of the gate voltage. (Inset) Sample geometry of the QPC. The shaded areas are the metallic gates, the point contact is defined where the two gates have the minimal distance *W*. (After [26]).
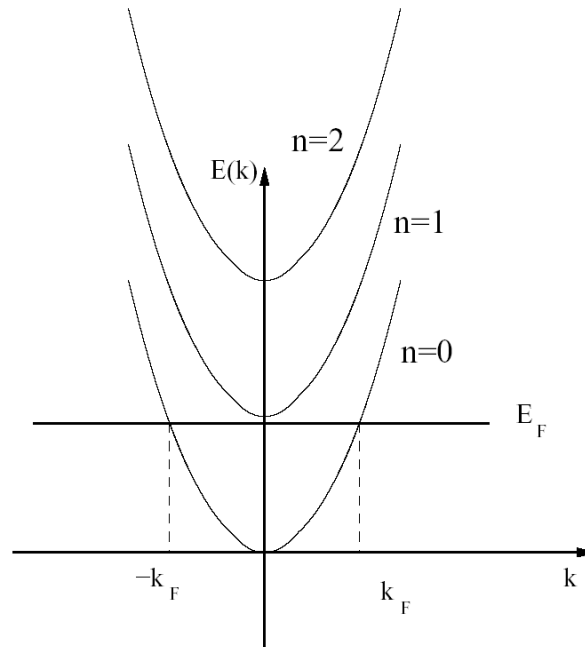
Figure 1.4: Electron bands in a 1D channel. The subband spacing increases increasing the strength of the confinement: in the case of the QPC as in Fig. 1.3, for decreasing negative values of V_g. The Fermi energy in this case is such that only the lowest subband is filled.

schematically depicted in Fig. 1.4. The motion along the x axis is free, while the subband spacing increases when decreasing the channel width W (tuning V_g towards more negative values). For a fixed Fermi level E_F, tuning V_g is therefore possible to change the number of populated subbands (since no magnetic field is present, each subband is doubly degenerate because of spin). In a simplified picture, which does not take into account disorder along the QPC, each subband acts as a "transport channel" whose conductance is e^2/h, therefore one has a total conductance

$$G = 2N(V_g)\frac{e^2}{h}$$

where $N(V_g)$ is the number of populated channels at a given gate voltage. A more refined result, which allows to treat also the case of disordered QPC, can be derived by means of the Landauer-Büttiker transport formalism [27–29]. In this framework, the conductance is determined by the *transmission probabilities* T_n for each channel as

$$G = 2\frac{e^2}{h}\sum_n T_n\,.$$

In the clean case, or with of nonzero temperature, the T_n are either 1 (occupied subband), or 0 (empty subband). In the disordered case, the transmission probabilities acquire an energy dependence, thus $0 \leq T_n(V_g) \leq 1$.

1.3   Carbon nanotubes

Recently, carbon nanotubes (CNT) [30] have attracted much interest for their outstanding mechanical and electronic properties. Since the discovery of the allotropic modification of carbon known as fullerene [31], in 1985, the research on carbon nanostructures gained much momentum. In 1991, Iijima [32] observed and identified for the first time CNTs and opened a new era for the carbon nanostructures. Roughly speaking, both fullerenes and CNTs are deformations of a graphene sheet: the former tend to assume an almost "spherical" configuration in which some of the hexagons which form the honeycomb structure of the graphene are substituted by pentagons, while CNTs are obtained by folding the graphene sheet effectively obtaining a tubular structure. Although fascinating, a complete description of the physics of CNTs is beyond the scope of this introduction and can be found in many books available in literature as, for instance [33]. Here, we limit to some very basic facts. The graphene sheet is a 2D honeycomb lattice of hexagons. Each vertex of this lattice is occupied by a carbon atom. The four valence band electrons of carbon are subdivided between sp_2 and π orbitals. The former extend perpendicularly to the graphene sheet and are responsible for the weak attraction between the graphene sheets (which form the graphite), while the latter give rise to a band structure that was calculated in the tight binding approximation by Wallace [34] in 1946. As a result, the graphene is a gapless semiconductor. In order to obtain CNTs, the graphene sheet must be "wrapped up". Referring to Fig. 1.5, the "folding vector" $\vec{C}$ (lying on the lattice space), which defines the direction along which the sheet is wrapped, can be introduced. This vector can be represented on a basis of the honeycomb, shown in Fig. 1.5, as $\vec{C} = n\vec{a}_1 + m\vec{a}_2$.
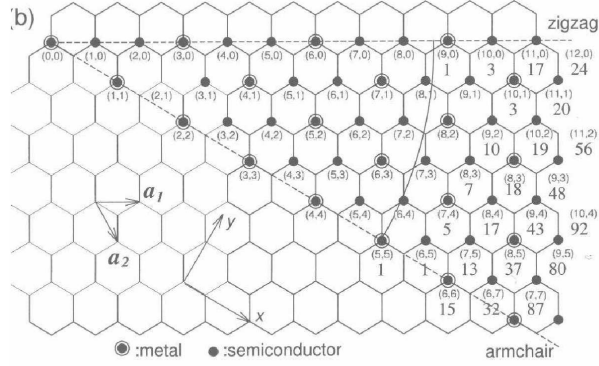
Figure 1.5: The graphene lattice and its basis $\vec{a}_1, \vec{a}_2$. Folding from the atom labeled $(0,0)$, the possible types of obtainable CNTs are shown, depending on the folding vector $\vec{C} = n\vec{a}_1 + m\vec{a}_2$. The folding vector is denoted in figure by its components on the given basis. (After [33])

The electronic properties of the resulting nanotube are defined exclusively by the folding vector (n, m) [33]. In particular, the wrapping procedure "slices" the two-dimensional graphene band structure, giving rise to one-dimensional subbands which are approximately given by

$$E_p(k) = \pm \frac{2\hbar v_{\mathrm{F}}}{d} \sqrt{\left(\frac{m - n}{3} + p\right)^2 + \left(\frac{dk}{2}\right)^2} \qquad (1.3)$$

where p is the band index, k is the longitudinal momentum along the CNT, d is its radius and v_{F} the Fermi velocity. Since the Brillouin zone of the graphene contains two equivalent points $\vec{K}$ and $-\vec{K}$ [33], the subband structure (1.3) must be duplicated. The index p comes from the quantization of the transverse momentum along the CNT, imposed by the wrapping. If $n - m = 3j$, with j an integer, we have a *chiral* CNT, for $n = m$ we talk about *armchair* nanotubes, while if $m = 0$ we have a *zig-zag* nanotube. These structures are rendered in Fig. 1.6. In all cases, when $n - m = 3j$ with j integer, we obtain *gapless metallic* nanotubes. Interestingly, they have two linear bands which cross around $E_p(k) = 0$, corresponding to a flat density of states. When $(n - m)/3$ is not an integer, the nanotube is semiconducting. A sketch of the discussed band structures is given in Fig. 1.7.

1.4   Quantum dots

When an electron system is confined in all the spatial dimensions to a size of the order of the Fermi wavelength, we obtain a zero-dimensional electron system, which is called quantum dot [6]. Several techniques can be exploited to create quantum dots: pillar type qdots can be fabricated by chemically etching a semiconducting heterostructure – an example is shown in Fig. 1.8. Alternatively, using metallic gates a droplet of electrons can be created depleting the 2DEG in
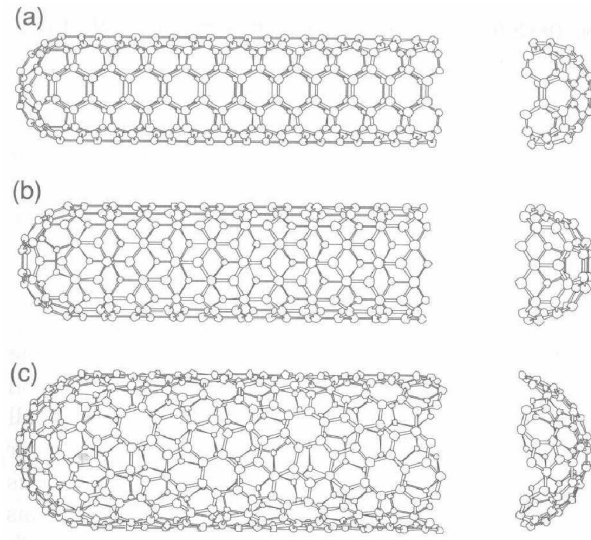
Figure 1.6: Three different nanotubes: (a) Armchair nanotube $(5,5)$ (metallic); (b) Zig-zag nanotube $(9,0)$ (metallic); (c) Chiral nanotube $(10,5)$ (semiconducting). (After [33])

GaAs/AlGaAs. Fig. 1.9 shows an example of such systems [35]. In section 1.5 we will show some examples of quantum dots embedded in one-dimensional systems. Semiconducting quantum dots are very interesting systems: quantum effects such as the presence of a discrete excitation spectrum cannot generally be neglected and electron-electron interactions strongly affect their properties. Connecting external source and drain leads, a current can be injected through the quantum dot, thus performing transport experiments. As we will see in this section and in the following of this thesis (see chapters 3,4), the study of current and differential conductance is an extremely powerful spectroscopic tool by means of which one can gain a lot of informations about the quantum dot itself. Due to charge quantization and confinement the quantum dot exhibits a typical energy scale E_C, the *charging energy*, which is the typical increase in energy due to the addition of one electron in the structure. In order to detect charging effects due to the tunneling of a single electron, the condition $k_B T < E_C$ must be fulfilled. In the following, we will assume the quantum dot has a discrete excitation spectrum. In semiconducting quantum dots as those formed in CEO heterostructures (see section 1.5) the typical level spacing is of the order of the μeV, sufficiently large to be detected in a transport measurement if the temperature T is not too high. In semiconducting dots, the maximum allowable temperature is of the order of 1 K. The maximum temperature in order to resolve charge quantization is of the same order of magnitude. Such temperatures are nowadays experimentally available. Consider a transport experiment: the quantum dot is coupled to external leads via tunneling barriers and suitable voltages are applied. In order to detect charge quantization effects in the transport, the tunneling resistance of the source (+) and drain
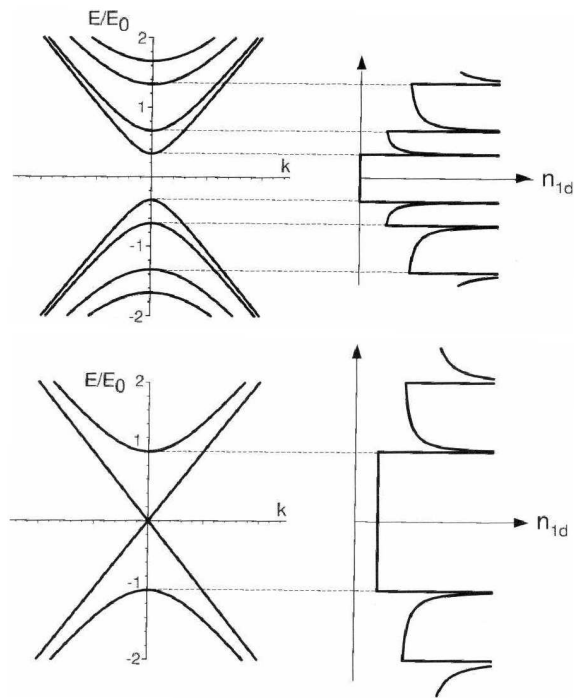
Figure 1.7: (Top) Band structure and density of states of a semiconducting CNT; (Bottom) Band structure and density of states of a metallic CNT. (After [33])
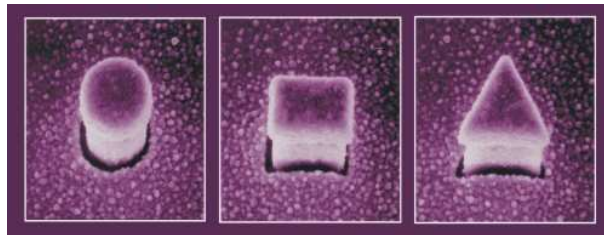
Figure 1.8: Electron microscope images of chemically etched quantum dots ("pillar dots"). (After Kouwenhoven's group homepage (Delft University))
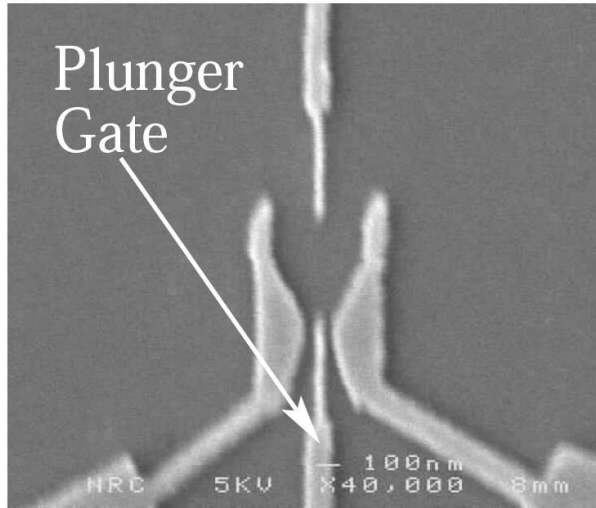
Figure 1.9: SEM image of a planar quantum dot: the gate geometry enables a precisely known number of electrons (N=0,...,50) to be trapped employing a special "plunger" gate. (After [35])

$(-)$ barriers must be sufficiently high; $R_\pm \gg R_K = h/e^2$ [36]. The schematic setup of a transport experiment on quantum dots is described in Fig. 1.10. The tunneling barriers are characterized by tunneling resistances $R_\pm$ and possibly different capacitances $C_\pm$. For the sake of simplicity, in the rest of this section we will assume a symmetric configuration for the capacitances $C_- = C_+$. Source and/or drain leads are connected to external voltage sources. In the figure, a symmetric voltage configuration has been assumed. In addition, a third external lead (the *gate* lead) is only capacitively coupled to the dot. The gate capacitance is such that $C_g \ll C_\pm$. No electrons tunnel through the gate lead. However, applying an external voltage V_g it is possible to change the effective charge of the dot in a *continuous* manner. In the *orthodox theory* [6, 36], the total energy $U(N)$ of a quantum dot with N electrons is estimated as

$$U(N) = \frac{e^2}{2C}\left(N - N_0 - N_g\right)^2 + \sum_{i=1}^{N} \epsilon_i \tag{1.4}$$

where $C = C_- + C_+ + C_g$ is the total capacitance of the quantum dot, N_0 is the number of the electrons in neutrality conditions, N is the number of *excess* electrons in the dot, $N_g = C_g V_g/e$ is the charge induced by the gate lead and ϵ_i is the single particle discrete excitation spectrum of the dot. $U(N)$ is composed by a semiclassical electrostatic contribution (first term) and a purely quantum second term. To have a finite current flowing through the system, we apply a source-drain voltage V: in terms of the electrochemical potentials of source and lead terminals it holds $\mu_- - \mu_+ = eV$ (-e is the electron charge). We assume here $T = 0$. Defining the electrochemical potential of the dot as

$$\mu_d(N) = U(N+1) - U(N) \tag{1.5}$$
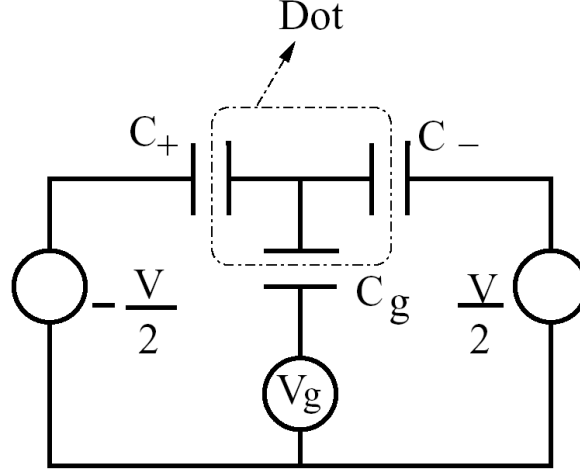
Figure 1.10: Schematic setup of a quantum dot, connected to source, drain, and gate leads. Source (+) and drain (−) tunneling barriers are characterized by tunneling resistances $R_\pm$ and capacitances $C_\mp$. A possible setup of bias and gate voltages are shown.

the condition for a current flowing from the source lead, through the dot, to the drain lead is

$$\mu_+ \leq \mu_d(N) \leq \mu_- \,. \tag{1.6}$$

Let us consider the *linear transport regime*, i.e. the limit $V \to 0$. The transport is allowed only when $\mu_d(N) = 0$, otherwise the quantum dot is in the *Coulomb blockade* regime and no current flows. The resonance condition can be achieved by suitably tuning the gate voltage V_g so that

$$N_g = N + \frac{1}{2} + \frac{\epsilon_{N+1}}{e^2/C} \equiv \bar{N}_g(N) \,. \tag{1.7}$$

When $\bar{N}_g(N-1) < N_g < \bar{N}_g(N)$, the quantum dot is *blocked* in the ground state for N excess electrons (measured w.r.t. the average number N_0), therefore tuning the gate voltage it is possible to select the ground state of the quantum dot. When (1.7) is fulfilled, the dot state oscillates between the ground states of N and $N+1$ electrons: the linear conductance $G = I/V$ ($V \to 0$) exhibits a δ-like peak. At nonzero temperature, the conductance peaks are smeared as shown in Fig. 1.11. Suppose now to keep a fixed gate voltage inside the the Coulomb blockade region and to increase the voltage V. At zero temperature and small voltages the transport is interdicted because tunneling through the source or the drain barrier is interdicted. Increasing the voltage, however, it is possible to fulfill (1.6) with increasing N: the current changes in a step-like fashion and a *Coulomb staircase* is observed [37]. In Fig. 1.12, the results of a non-linear transport experiment in a quantum dot are shown. This is the *nonlinear transport regime*, whose description critically depends on the details of the specific quantum dot. Increasing the source-drain voltage, between ground state
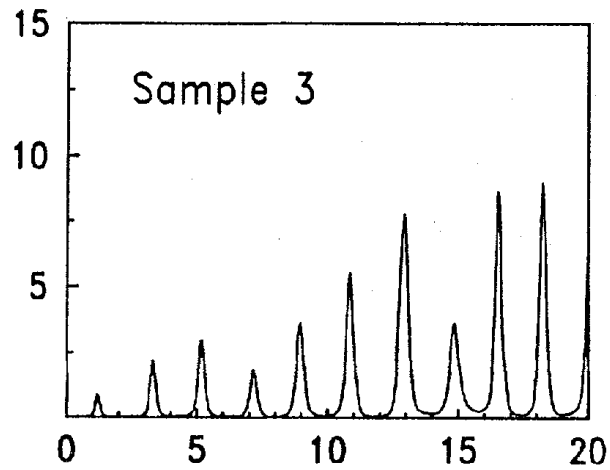
Figure 1.11: Conductance (a.u.) of a planar quantum dot in the linear transport regime as a function of the gate voltage (in mV). (After [7])
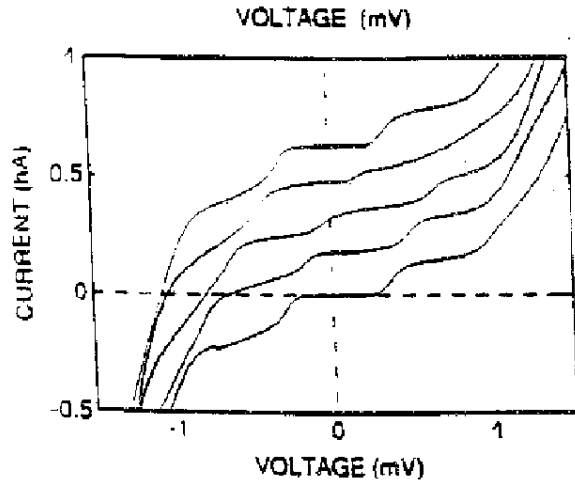
Figure 1.12: Coulomb staircase in the current of a quantum dot in the nonlinear transport regime. Curves for different gate voltages V_g have been offset for clarity. (After [37])
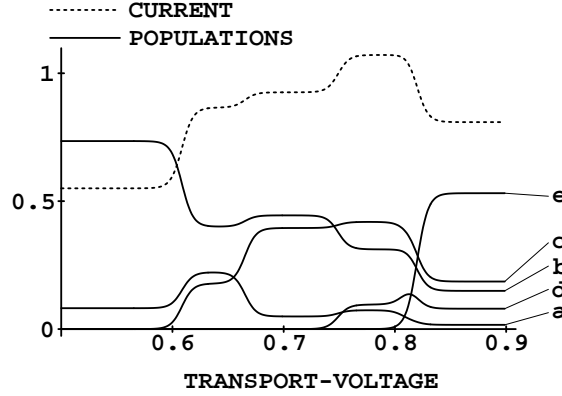
Figure 1.13: Nonlinear current (dotted curve, arbitrary units) and stationary occupation probabilities (solid lines, labelled **a**,...,**e**) of the states involved in the transport for a quantum dot as a function of the source-drain voltage (arbitrary units). (After [42])

and excited state and between different excited states can be observed. The latter are detectable if the quantum dot excited states have lifetimes comparable to the average time scales of the current [38]. Their description goes beyond the orthodox theory. Increasing the bias voltage, the number of possible transitions which support the transport (*transport channels*) increases. Although intuitively this should lead to an increase of the current, this is not always the case. The most celebrated example of a *decreasing* current when increasing the number of transport channels is the *spin blockade effect* [39,40], which has recently been observed in planar quantum dot created by metallic gate patterning [41]. This gives rise to a *negative differential conductance* $G = dI/dV$. The spin blockade effect is shown in Fig. 1.13, where the nonlinear current I for a quasi-one dimensional quantum dot is shown as a function of the bias voltage (arbitrary units). In this regime, the quantum dot oscillates between the charge states $n = 2$ and $n = 3$ (here, $n = N - N_0$ represents the charge unbalance w.r.t. the neutral condition). Increasing the voltage, the current exhibits a step-like behavior. Each step onset corresponds to the opening of a new transport channel. For $V \approx 0.8$, the current sharply decreases. In Fig. 1.14 a scheme of the states relevant to the transport in this region are shown. The quantum dot is in the *sequential tunneling* regime, which means that after each tunneling event the electron coherence is lost, preventing virtual transitions inside the quantum dot. Around $V \approx 0.8$, the transport channel corresponding to the transition

$$|n = 2, S = 1\rangle \rightarrow |n = 3, S = 3/2\rangle$$

opens up. As it is clear from inspecting Fig. 1.13, the state $|n = 3, S = 3/2\rangle$ (**e**) acquires most of the occupation probability, signalling that its occupation time is much longer than that of all the other states. Inspecting the scheme in Fig. 1.14, which represents the allowed transitions between dot states, it is clear that the state **e** has only one escape transition, because of the spin selection rules preventing the direct decay $|n = 3, S = 3/2\rangle \rightarrow |n = 2, S = 0\rangle$,
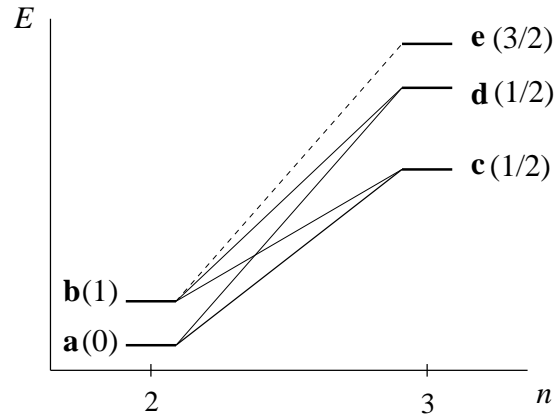
Figure 1.14: Scheme of the states involved in the transport for $V \approx 0.8$ (see Fig. 1.13). On the horizontal axis is the charge unbalance $n = N - N_0$, on the vertical axis the state energy. The total spin S for the various states is shown (units $\hbar/2$). (After [42])

while all the other states have at least two escape transitions. This gives rise to a "dynamical trapping" of the state **e** leading to an overall decrease in the current. Because of spin selection rules, this effect may happen each time an excited state of the dot with maximal total spin is occupied. A similar effect, induced by interactions and not specifically related to spin selection rules, will be discussed in chapter 4.

1.5   Quantum dots in 1D structures

Quantum dots can be created also in one-dimensional systems. In the following we will show two examples of such systems and analyze some transport experiment performed on them.

1.5.1   Quantum dots in CEO heterostructures

The Cleaved Edge Overgrowth (CEO) technique [43] has been developed to create an atomically sharp edge in 2DEGs created in semiconducting heterostructures. The 2DEG, formed in a GaAs (white layer inside the gray AlGaAs wafer in Fig. 1.15 (a)) quantum well heterostructure is cleaved in ultrahight vacuum along the (011) direction. Subsequently, another sequence of AlGaAs (thin) and n^+ GaAs (thick) is overgrown in the (011) direction (Fig. 1.15 (b)). The doped overgrowth sequence injects electrons at the edge of the quantum well (Fig. 1.15 (d)). The strong overlap between the 2DEG and the states formed at the edge strongly couples both systems along the latter [44, 45]. Applying a suitable negative voltage to a metallic gate deposed ontop of the structure (W gate in Fig. 1.15 (a)), the underlying 2DEG is depleted (Fig. 1.15 (e)). Employing a positive bias on the side gate S, electrons are tightly confined on the
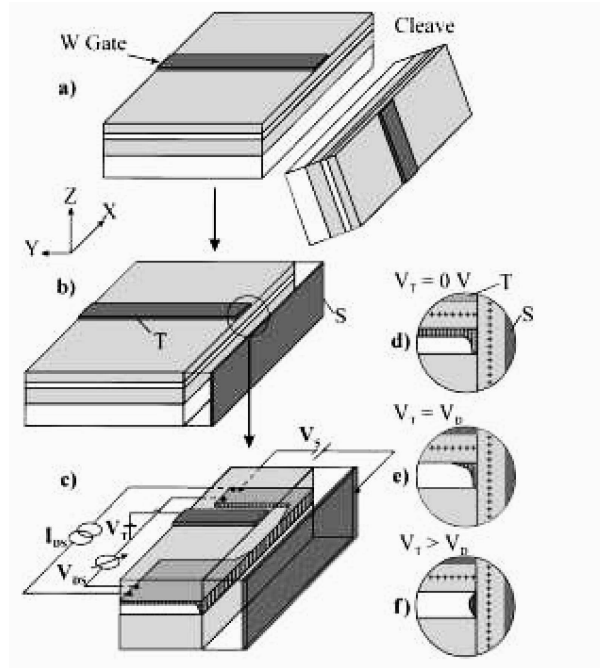
Figure 1.15: The creation of a CEO sample and the experimental setup for transport measurements. (After [44])

edge of the overgrowth side (Fig. 1.15 (f)). Tuning voltages on gates W and S makes it possible to create a 1DEG in the region below the W gate and to control its electron density. Outside this region, the 1D states are strongly coupled to the 2DEG, allowing to perform transport measurements applying suitable source-drain voltages to the wires using the 2DEGs as contacts (Fig. 1.15 (c)). CEO channels have been employed firstly to study 1D transport features such as conductance quantization [44]. Subsequently, the regime of extremely low density for the 1D channel has been investigated [8]. In Fig. 1.16 the linear ($V_{sd} \approx 0$) conductance of a CEO channel is shown as a function of the top gate voltage. Tuning the latter to increasingly negative values, the density of the channel is decreased. Signatures of a non perfect quantization of the conductance plateaux are present. The wide oscillations can be attributed to the presence of impurities along the channel. More striking is the leftmost part of the graph, where the conductance drops to zero, signalling the depopulation of the lowest 1D subband of the channel. Indeed, as shown in the inset, almost-equidistant conductance peaks are present. An interpretation of this result can be given with the aid of Fig. 1.17: along the one-dimensional channel an impurity potential landscape is present. As long as the density of the channel is high enough (a), the system displays a one-dimensional behavior with a quantized conductance. When the density is reduced, however, the chemical potential of the system can cross the impurity levels landscape. When two impurity levels cross the Fermi level, the system is effectively cut in three pieces. The two "external" regions are still adiabatically connected to the two-dimensional
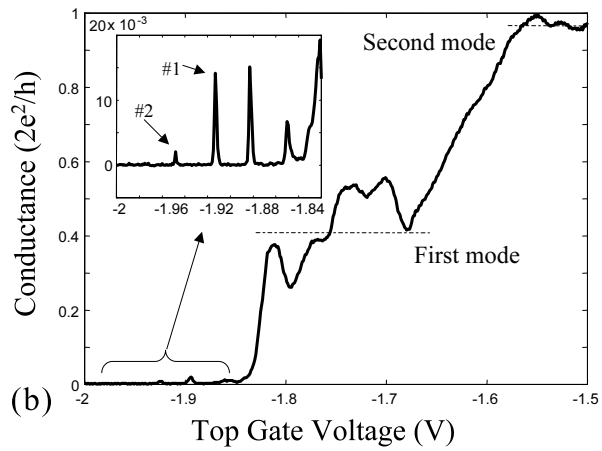
Figure 1.16: Main: Linear conductance measurement ($V_{\mathrm{sd}} \approx 0$) in the CEO sample studied by O. M. Auslaender *et al.* [8] as a function of the top-gate voltage. Inset: zoom of the region where the lowest 1D subband is depopulated, showing the presence of almost equidistant conductance peaks, which are interpreted as the Coulomb blockade peaks of a quantum dot in the linear transport regime. (After [8]).
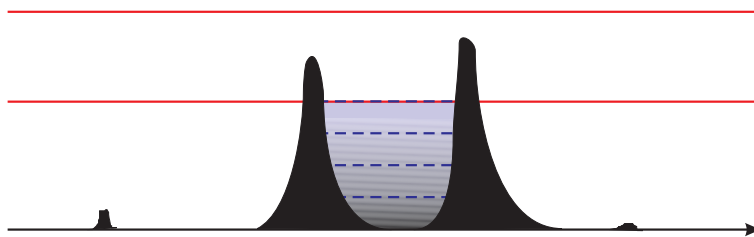
Figure 1.17: Sketch of the one-dimensional channel realized at the edge of the GaAs-AlGaAs heterostructure. The impurity potential landscape is shown, and the red lines represent different electrochemical potentials of the system.

electronic system, while the confined one-dimensional region between the two impurities can be thought of as a *1D quantum dot*. Therefore, keeping $V_{sd} \approx 0$ and sweeping the top voltage can be interpreted as a *linear conductance measurement* performed on a 1D quantum dot. The peaks found in the inset of Fig. 1.16 are therefore explained as the linear conductance peaks that occur whenever the ground states for N and $N+1$ electrons in the dot become degenerate. The
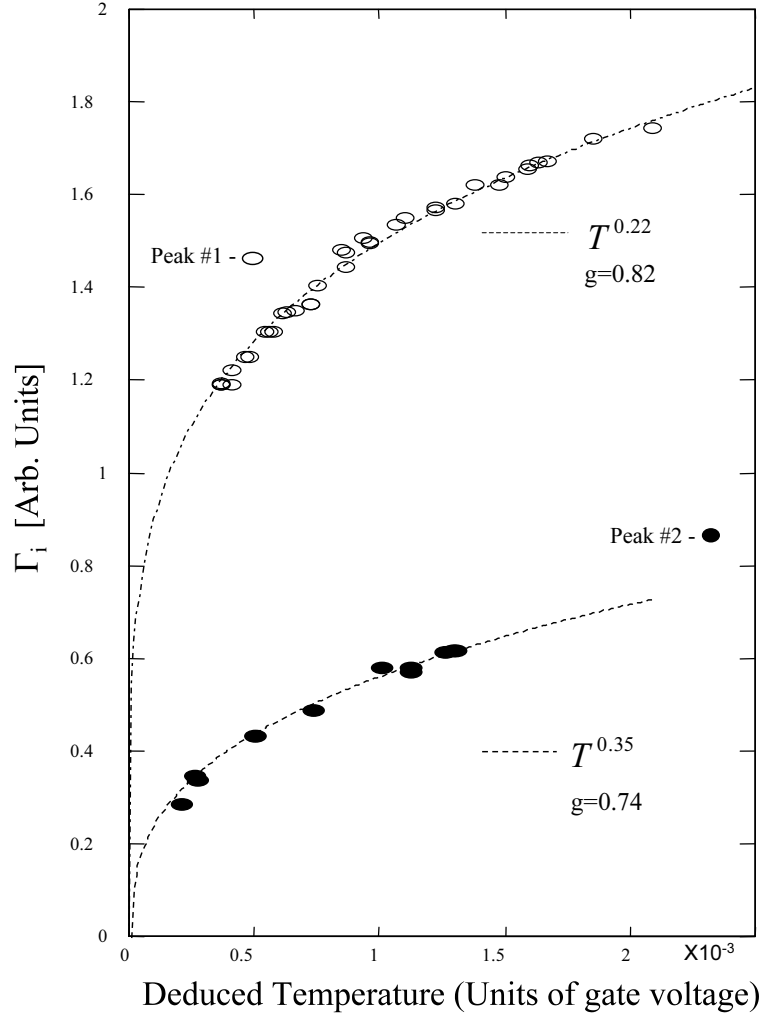
Figure 1.18: Integrated area Γ_i under the conductance peaks #1 (empty dots) and #2 (solid dots) – see Fig. 1.16 as a function of the temperature. The dotted lines are fits of the theoretical prediction $\Gamma_i \propto T^{(g^{-1}-1)}$, where g is the (spinless) LL interaction parameter [14]. (After [8]).

transport properties of this one-dimensional quantum dot display some peculiar feature: analyzing the temperature dependence of the area under the linear conductance peaks (Fig. 1.18), a power law scaling as a function of the temperature T^α is found, in sharp contrast with the predictions of the Fermi liquid

picture that would imply a temperature-independent area [46]. This behavior has been interpreted as the signature of a Luttinger liquid[14] (see chapter 2). The latter is a model for interacting one-dimensional electronic systems which indeed predicts a power-law scaling of the linear conductance (see also chapter 4).

1.5.2 Quantum dots in carbon nanotubes

Quantum dots can be created also by means of metallic carbon nanotubes. They are especially appealing because of their linear dispersion relation in a low-energy sector around the Fermi energy. Since the higher subbands are sufficiently separated in energy [33], they can be considered "frozen out" at easily achievable experimental temperatures, so that a truly one-dimensional channel is achievable. This system can be theoretically described by a "four branches" LL model [47]: therefore peculiar power-law features can be expected in transport properties. In the top part of figure 1.19, a single wall carbon nanotube
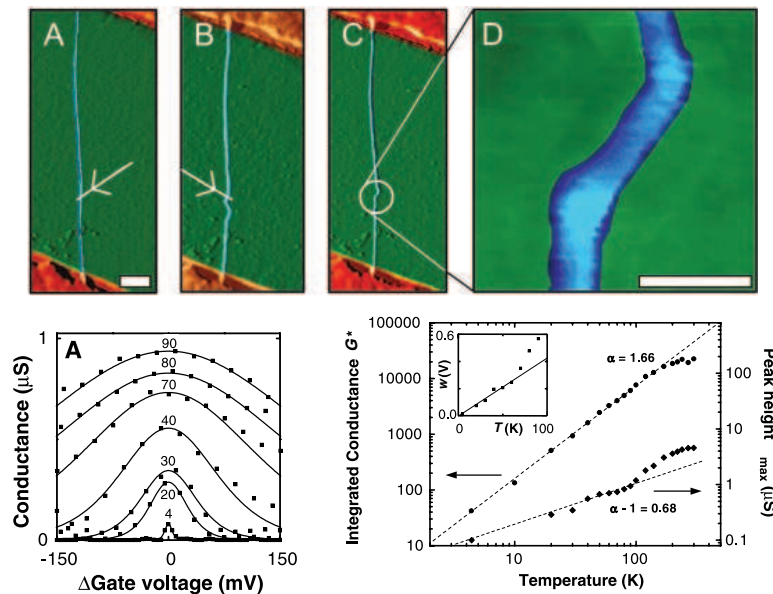
Figure 1.19: Top: atomic force microscopy images of a single wall carbon nanotube (blue) ontop a Si/SiO_2 substrate (green), contacted to metallic gates (brown). After the deposition of the nanotube (A, white bar: 200nm), whose radius is 20-50 nm, two buckles are created by using the AFM tip (B, C), thus defining a short region in between, of length $\approx$20 nm (white bar: 20nm). Bottom left: linear conductance peaks for different temperature values ranging from 4K to 90K – dots: experimental data, solid line: theoretical fit. Bottom right: maximum (right scale) and area (left scale) for the linear conductance peaks as a function of the temperature in double logarithmic scale, shows clearly a power-law behavior. (After [20]).

(blue) is shown ontop of a Si/SiO_2 substrate (green) [20]. The tube has a length

of several μm, a radius of about 20 nm, and is connected to metallic gates (brown). By manipulation with an AFM tip, it is possible to create two buckles in the nanotube, giving rise to the situation indicated in the panel (D), where a region with a length of $\approx$20 nm is defined along the nanotube. It can be demonstrated [33] that a strong geometrical deformation of a nanotube introduces pentagonal and heptagonal defects in the reticular structure of the system. These defects act as impurity potentials along the nanotube. Thus, if these impurity levels emerge above the Fermi level of the system, a one-dimensional quantum dot can be created, as in the case of disordered CEO channels. By applying a small voltage to the metallic gates, it is possible to perform a transport experiment in such a system. If the potential of the substrate is varied, the density of the channel can be tuned so that a linear transport measurement can be performed. Linear conductance peaks have been found (Fig. 1.19, bottom left) and studied at various temperatures. Indeed, striking evidence of power law scaling both for the peak area and the peak maximum have been found (Fig. 1.19, bottom right), whose validity extends over one decade in temperature.

The Luttinger liquid

"It is a mistake to think you can solve any major problems just with potatoes." (**D. Adams**)

In this chapter, the description of a 1D system of interacting electrons is addressed. After a brief survey of the properties of the Fermi liquid in 3D and 2D [48] (section 2.1), the Luttinger liquid model is introduced [14]. After the study of a spinful system with forward-scattering interactions and periodic boundary conditions (sections 2.2.2), the bosonization identity is introduced (2.2.3). The case of open boundary conditions is then considered analyzed (2.2.4), before turning to the special case of a spinless LL (with periodic boundary conditions), in section 2.2.5. Here, and in the rest of this thesis, we set $\hbar = 1$.

2.1 Landau Fermi liquid theory breakdown

Consider a translationally invariant non-interacting Fermi gas consisting of N *noninteracting* spin-degenerate electrons with mass m at temperature $T = 0$. Each electron is characterized by its momentum $\vec{k}$ and the projection of the spin along a quantization axis $\sigma = \pm 1$ in units $\hbar/2$. The ground state of the gas is found by minimizing the electrons kinetic energy, subject to the Pauli exclusion principle constraint. This gives rise to the well-known *Fermi sea*, e.g. the set of states in the k-space which fulfill the condition $k \leq k_{\mathrm{F}}$, where $k \equiv |\vec{k}|$ and the Fermi wavevector k_{F} has been defined as the modulus of the highest occupied momentum. The *distribution function* of the occupied states $n_{\vec{k},\sigma} = 2\vartheta(k_{\mathrm{F}} - k)$ is characterized by a discontinuity at $k = k_{\mathrm{F}}$, which is the hallmark of the Fermi surface. The total energy of the configuration is simply given by

$$E = \sum_{\vec{k}\sigma} n_{\vec{k},\sigma} k^2 / 2m \,. \tag{2.1}$$

Introducing the second-quantized creation (annihilation) operators for an electron with momentum $\vec{k}$ and spin σ, $c^{\dagger}_{\vec{k},\sigma}$ ($c_{\vec{k},\sigma}$), the Fermi sea is the state $|\Omega_N\rangle$ such that $c^{\dagger}_{\vec{k},\sigma}|\Omega_N\rangle = 0$ if $k \leq k_F$ and $c_{\vec{k},\sigma}|\Omega_N\rangle = 0$ if $k > k_F$. The addition to the ground state of N particles of one electron in the lowest available momentum state, *right at the Fermi surface*, gives rise to the ground state of $N + 1$ electrons $|\Omega_{N+1}\rangle$. An *excited state* of the N electrons is composed by a neutral superposition of M particle-hole pairs

$$|\Omega_N^*\rangle = \sum_{i=1}^{M} c^{\dagger}_{\vec{k}_i + \vec{q}_i, \sigma} c_{\vec{k}_i, \sigma} |\Omega\rangle \, , \tag{2.2}$$

provided that $|\vec{k}_i| \leq k_F$ and $|\vec{k}_i + \vec{q}_i| > k_F$. The state $|\Omega_N^*\rangle$ is characterized by a new distribution function $n^*_{\vec{k},\sigma} = n_{\vec{k},\sigma} + \delta n_{\vec{k},\sigma}$. The energy of such an excited state is simply given by Eq. 2.1 with $n_{\vec{k},\sigma}$ replaced with $n^*_{\vec{k},\sigma}$. Consider the case of a single particle-hole pair, as is depicted in Fig. 2.1: $\delta n_{\vec{k},\sigma} = (\delta_{\vec{k},\vec{q}_1} - \delta_{\vec{k},\vec{q}_2})\delta_{\sigma,\sigma'}$ ($q_1 > k_F$, $q_2 < k_F$). Denoting $\vec{q} = \vec{q}_1 - \vec{q}_2$ the transferred momentum, the
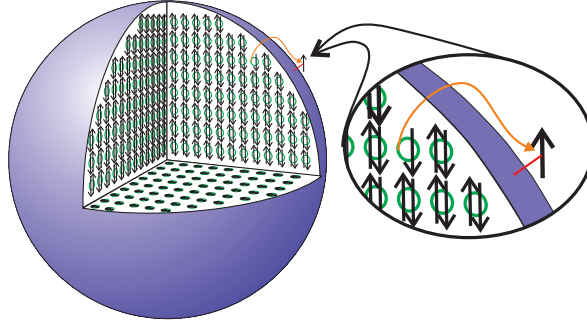
Figure 2.1: Sketch of the Fermi sphere in the momentum space for a three-dimensional electron gas. An electron-hole excitation is shown – see the zoom. (After [49])

excitation energy for such a pair is given by

$$\delta E = \frac{1}{m}\vec{q} \cdot \left(\frac{\vec{q}_1 + \vec{q}_2}{2}\right)$$

At low temperature, and without any additional external perturbation, the particle-hole pairs can be formed only in a small region of the order $k_B T$ around the Fermi surface. This leads to the prediction of a specific heat which grows linearly with the temperature [50].

This prediction, as well as other consequences of the Fermi gas picture have been confirmed surprisingly well in ordinary metals. This is far from an obvious result, in view of the fact that electrons are scattered by the Coulomb interaction. However, a rough estimate of the potential Coulomb energy leads to $E_{pot} \approx e^2/\bar{r}$, where e is the electron charge and $\bar{r}$ is the average electron distance. One has $E_{pot} \propto n^{1/D}$, where n is the density of the electron gas,

and $D = 3$ is the dimensionality of the system. By comparing the Coulomb potential energy with the average kinetic energy of the electrons $E_{\text{kin}} \propto n^{2/D}$ one finds $E_{\text{pot}}/E_{\text{kin}} \propto n^{-1/D}$. This result supports the validity of the noninteracting theory in the thermodynamic limit and is a consequence of the Pauli exclusion principle which becomes increasingly important in the high density limit, thus favoring the kinetic energy in comparison with the potential one.

It was one of the greatest achievements of Lev. D. Landau [51] to point out that in "normal" metals, most of the properties of the interacting N-electrons system greatly resemble those of a free Fermi gas with renormalized parameters, such as an effective mass. To clarify this point, let us consider a noninteracting electron gas and suppose to *include adiabatically* the interaction among the electrons from the time $t = -\infty$ to the time $t = 0$

$$H = H_0 + e^{\eta t} H_1 \tag{2.3}$$

where H is the total Hamiltonian, H_0 is that of the free electrons, H_1 the interaction term and $\eta \to 0^+$. Under the adiabatical approximation, the eigenvalues $|\phi_i\rangle$ of the Fermi gas will evolve continuously into the eigenstates $|\tilde{\phi}_i\rangle$ of the interacting system. In a normal metal, it is assumed that all the eigenvalues of the interacting system can be created starting from some eigenvalue of the noninteracting gas. Let us add a particle with momentum $p > k_{\text{F}}$ to the noninteracting ground state $|\Omega_N\rangle$ and, as above, turn on adiabatically the interaction. If momentum is conserved by the scattering among the particles, an excited state with the same momentum p will be obtained at the time $t = 0$. In the real space, upon the adiabatic inclusion of the interactions, the electron "dresses up" with a cloud of electron-density fluctuations, therefore acting as a composite particle with renormalized mass called a quasiparticle. Because a quasiparticle can be created only if its momentum lies above the Fermi surface, their distribution function exhibits a sharp jump of the order of $\sqrt{Z} < 1$ at the Fermi momentum, which decreases with increasingly strong interactions. Despite a generally weak residual interaction, these quasiparticles can be considered essentially as free objects. However the weak scattering due to residual interactions gives rise to a *finite lifetime τ* of the quasiparticles. If the latter is longer than the characteristic time of the adiabatic inclusion of interactions η^{-1}, then quasiparticles are essentially well-defined objects. From simple phase-space arguments, Landau has remarkably shown that in $D = 3$, at zero temperature the quasiparticle lifetime diverges at the Fermi surface

$$\tau(\varepsilon) \propto \frac{1}{(\varepsilon - \varepsilon_{\text{F}})^2},$$

where $\varepsilon_{\text{F}} = k_{\text{F}}^2/2m$ is the Fermi energy. Therefore, the quasiparticle description is not likely to run into trouble around the Fermi surface, since there one has $\tau(\varepsilon \approx \varepsilon_{\text{f}}) > \eta^{-1}$. Therefore the quasiparticles "survive" the inclusion of interaction. The Landau theory, which can be confirmed by a rigorous perturbation theory in the interaction Hamiltonian, is neither restricted to electronic systems, nor to weakly interacting ones, its main conclusions being essentially due to very general phase-space arguments [48].

It must be noticed that the quasiparticle excitation are not the only excitations of an interacting electron system. Indeed, one can define collective modes

that describe the response of the system *as a whole* to an external disturbance. For instance, with short-range interacting fermions (e.g. ^{3}He), the collective excitations of the charge density are called zero sound. With long-range interactions (as in conventional metals, for instance) the collective excitations are plasmons. Essentially analogous arguments can be made about the validity of the Landau picture of interacting electrons in $D = 2$. However, things are very different when dealing with the $D = 1$ case. Even from a very intuitive
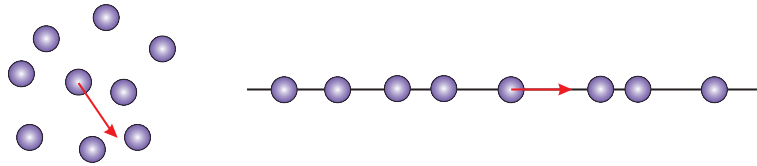
Figure 2.2: (Left) In a $D \geq 2$ interacting fermionic system, nearly-free quasiparticles that behave qualitatively like individual particles are possible; (Right) In a $D = 1$ interacting fermionic system all the excitations become collective.

argument, in a one-dimensional interacting electron system (Fig. 2.2 right) the motion of each electrons affects dramatically all the other electrons. This is in sharp contrast with the situation found in higher dimensionality (see, e.g., Fig. 2.2 left – for $D = 2$) where quasiparticle excitations can propagate nearly freely, without affecting dramatically the system. Indeed, the calculation of the quasiparticle lifetime in $D = 1$ leads to the rather discomforting result $\tau = 0$. This means that the quasiparticles are not well-defined objects, not even on the time scale of the adiabatic inclusion of interactions! This means that the adiabatic inclusion of interactions is a troublesome concept in 1D fermionic systems. The failure of the quasiparticle concept, in turns, implies that the excitations of 1D fermionic systems may have a different character. Indeed, it can be demonstrated that in the low-energy sector all the excitations of the 1D fermionic systems have collective character, being formed by charge density waves (CDW) and spin density waves (SDW). In the next section, a model for interacting one-dimensional electrons will be introduced.

2.2 Tomonaga-Luttinger liquids

2.2.1 A short introduction

The Tomonaga-Luttinger liquid model for interacting, 1D electrons has been introduced in 1950 by S. Tomonaga [52] and subsequently reconsidered by J. M. Luttinger [53] in 1963. Although exactly solvable within the forward-scattering approximation, this model has shown its full potential only after the bosonization identity has been demonstrated [54]. Many good review papers on the subject have been published, among which one of the most famous and extensive is the one by J. Voit [14]. Very recently, T. Giamarchi has published a monograph book on the quantum physics of 1D system, where the Luttinger liquid is studied in great detail together with many examples and extensions [55].

2.2.2   Periodic Luttinger liquids

In this section, we follow [14]. Consider a system of free electrons in one dimension, with the Hamiltonian

$$H_0 = \sum_{k,s} \varepsilon_k c_{k,s}^\dagger c_{k,s} \tag{2.4}$$

where $\varepsilon_k = k^2/2m$ represents the kinetic energy of the electrons, m is their mass, and $c_{k,s}$ ($c_{k,s}^\dagger$) destroys (creates) an electron with momentum k and spin projection along a quantization axis $s = \pm 1$ (units $\hbar/2$). We want to describe
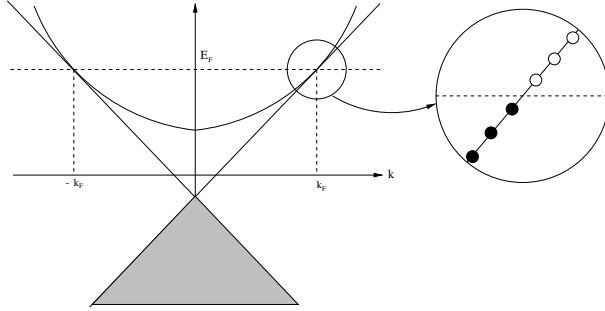
Figure 2.3: Parabolic energy spectrum of free electrons in one dimension and linearization around the Fermi energy. A zoom of the region around k_F is displayed in the right part. The infinite Dirac sea of states with negative energies is shaded in gray.

the low-energy dynamics of the system around the Fermi energy E_F. Therefore, we linearize the dispersion relation around $k_\mathrm{F}^{(\pm)} \equiv \pm\sqrt{2m\varepsilon_\mathrm{F}}$ (see Fig. 2.3). This leads to the creation of two branches $\varepsilon_{r,k} = v_\mathrm{F}(rk - k_\mathrm{F})$ of right ($r = +1$) and left-moving ($r = -1$) electrons. Introducing right and left-moving electrons destruction (creation) operators as $c_{r,k,s}$ ($c_{r,k,s}^\dagger$), we can rewrite the free Hamiltonian as

$$H_0 \approx \sum_{r,s=\pm 1} \sum_{k=-\infty}^{\infty} \varepsilon_{r,k} : c_{r,k,s}^\dagger c_{r,k,s} : \tag{2.5}$$

where we have introduced the normal-ordering operator : $\hat{O} := O - \langle \hat{O} \rangle_0$ to take care of the fictitious Dirac sea that we have introduced linearizing the spectrum. We can introduce density fluctuation operators for the r branch as

$$\rho_{r,s}(q) = \sum_p : c_{r,q+p,s}^\dagger c_{r,p,s} : \tag{2.6}$$

and observe that the above defined operators obey the Kac-Moody algebra constitutive relation

$$\left[\rho_{r,s}(q), \rho_{r',s'}(-q') \right] = -\delta_{r,r'}\delta_{s,s'}\delta_{q,q'}\frac{rqL}{2\pi} \tag{2.7}$$

where L is the length of the system. Here, we assume periodic boundary conditions. In the next section, the case of open boundary conditions will be ad-

dressed. It is crucial to observe that the operators (2.6) satisfy also the commutation relation

$$[H_0, \rho_{r,s}(q)] = r v_{\mathrm{F}} q \rho_{r,s}(q) \tag{2.8}$$

which allows to write

$$H_0 = \frac{\pi v_{\mathrm{F}}}{L} \sum_{r,q \neq 0, s} : \rho_{r,s}(q) \rho_{r,s}(-q) : + \mathrm{const}. \tag{2.9}$$

For a fixed number of particles, (2.5) and (2.9) are equivalent by virtue of the Kronig's identity [56]. The (up to now) undetermined constant is fixed considering the addition energy of $N_{r,s}$ electrons with spin s in the r branch. One then has

$$H_0 = \frac{\pi v_{\mathrm{F}}}{L} \sum_{r,q \neq 0, s} : \rho_{r,s}(q) \rho_{r,s}(-q) : + \frac{\pi v_{\mathrm{F}}}{L} \sum_{r,s} N_{r,s}^2. \tag{2.10}$$

Treating a system of interacting electrons, the Hamiltonian becomes $H = H_0 + H_{\mathrm{int}}$, where

$$H_{\mathrm{int}} = \frac{1}{2L} \sum_{s_1, s_2} \sum_{k_1, k_2, q} V(q) c_{k_1+q, s_1}^\dagger c_{k_2-q, s_2}^\dagger c_{k_2, s_2} c_{k_1, s_1}. \tag{2.11}$$

This Hamiltonian describes the most generic translationally invariant interaction among electrons. However, in order to be able to solve the Luttinger model, it is necessary to make some approximation on the type of interactions that shall be considered. In particular, we are interested in rewriting H_{int} using the density fluctuation operators. It turns out that it is possible, if we restrict to the case of forward scattering where the interacting electons do not change branch. After some algebraic rearrangement, we can rewrite H_{int} as

$$H_{\mathrm{int}} = \frac{1}{2L} \sum_{q,s} V(q) \left\{ \frac{1}{2} \left[\rho_{+,s}(q) \rho_{-,s}(-q) + \rho_{+,s}(q) \rho_{-,-s}(-q) \right] \right.$$
$$\left. + \sum_{r=\pm 1} \left[: \rho_{r,s}(q) \rho_{r,s}(-q) : + : \rho_{r,s}(q) \rho_{r,-s}(-q) : \right] \right\}. \tag{2.12}$$

It is convenient to switch to charge (ρ) and spin (σ) variables

$$\rho_r(q) = \frac{1}{\sqrt{2}} \left[\rho_{r,+}(q) + \rho_{r,-}(q) \right] \qquad N_{r,\rho} = \frac{1}{\sqrt{2}} \left[N_{r,+} + N_{r,-} \right] \tag{2.13}$$

$$\sigma_r(q) = \frac{1}{\sqrt{2}} \left[\rho_{r,+}(q) - \rho_{r,-}(q) \right] \qquad N_{r,\sigma} = \frac{1}{\sqrt{2}} \left[N_{r,+} - N_{r,-} \right] \tag{2.14}$$

obtaining the equivalent form of $H = H_0 + H_{\mathrm{int}}$, with $H_0 = H_{0,\rho} + H_{0,\sigma}$ and

$$H_0 = \frac{\pi v_{\mathrm{F}}}{L} \sum_{\nu=\rho,\sigma} \sum_{r=\pm 1} \sum_{q \neq 0} : \nu_r(q) \nu_r(-q) : + \frac{\pi v_{\mathrm{F}}}{L} \sum_{\nu=\rho,\sigma} \sum_{r=\pm 1} N_{r,\nu}^2 \tag{2.15}$$

$$H_{\mathrm{int}} = \frac{1}{L} \sum_q V(q) \left[2 \rho_+(q) \rho_-(-q) + \sum_{r=\pm 1} : \rho_r(q) \rho_r(-q) : \right]. \tag{2.16}$$

Writing the Hamiltonian in this form, it is immediately clear that, under the hypothesis of forward scattering, the spin variables are free. The charge sector,

on the contrary, can be easily diagonalized with a Bogoljubov transformation [57]. Under this transformation, the charge operators transform as

$$\tilde{\rho}_r(q) = r\rho_r(q)\cosh[\xi(q)] - r\rho_{-r}(q)\sinh[\xi(q)] \qquad (2.17)$$

with

$$4\xi(q) = -\ln\left(1 + \frac{2V(q)}{\pi v_F}\right). \qquad (2.18)$$

For $H_\rho = H_{0,\rho} + H_{int}$ we have

$$H_\rho = \frac{\pi v_F}{L}\sum_{r=\pm 1}\sum_{q\neq 0} g_\rho^{-1}(q) : \tilde{\rho}_r(q)\tilde{\rho}_r(-q) : + \frac{\pi v_F}{2Lg_\rho^2(q\to 0)}N_\rho^2 + \frac{\pi v_F}{2L}J_\rho^2 \quad (2.19)$$

where we have introduced the total charge $N_\rho \equiv N_{+,\rho} + N_{-,\rho}$ and the topologic current $J_\rho \equiv N_{+,\rho} - N_{-,\rho}$ which describes the imbalance between left- and right-moving charges. The factor

$$g_\rho^{-1}(q) = e^{-2\xi(q)} = \sqrt{1 + \frac{2V(q)}{\pi v_F}} \qquad (2.20)$$

describes the renormalizing effect of the interactions on the dispersion relation of the system. In the noninteracting case, $g_\rho(q) = 1$. It is possible to define bosonic operators

$$b_\rho^\dagger(q) = \sqrt{\frac{2\pi}{L|q|}}\sum_r \vartheta(rq)\rho_r(q) \qquad (2.21)$$

which satisfy canonical commutation relations $\left[b_\rho(q), b_\rho^\dagger(q')\right] = \delta_{q,q'}$. With this, we can finally rewrite H_ρ as

$$H_\rho = \sum_{q\neq 0}\omega_\rho(q)b_\rho^\dagger(q)b_\rho(q) + \frac{\pi v_F}{2Lg_\rho^2}N_\rho^2 + \frac{\pi v_F}{2L}J_\rho^2 \qquad (2.22)$$

where we have introduced $\omega_\rho(q) = v_F|q|/g_\rho(q)$ and $g_\rho = g_\rho(q\to 0)$. The spin sector can be rewritten in the same form

$$H_\sigma = \sum_{q\neq 0}\omega_\sigma(q)b_\sigma^\dagger(q)b_\sigma(q) + \frac{\pi v_F}{2Lg_\sigma^2}N_\sigma^2 + \frac{\pi v_F}{2L}J_\sigma^2 \qquad (2.23)$$

with analogous notations. In the spin sector, we have of course $g_\sigma \equiv 1$. The two Hamiltonians are completely decoupled: $[H_\rho, H_\sigma] = 0$. Some comments are in order.

First of all the charge and spin excitations propagate at different velocities: in the forward scattering approximation $v_\nu(q) = v_F/g_\nu(q)$. As can be shown with the bosonization procedure, the injection of one electron in the Luttinger liquid excites collective charge and spin density waves which are the *only* possible excitations of the system. After some time, charge and spin density waves will be spatially separated: this is the real-space manifestation of the spin-charge separation, which is the hallmark of the Luttinger liquid. Recently, experimental evidences of this phenomenon have been reported [58–61].

Of course the excitations spectrum depends on the form of $V(q)$, the Fourier transform of the projected real interaction between Fermions. For instance, for

a Yukawa potential $V(\vec{r}) = V_0 \exp(-\alpha|\vec{r}|)/|\vec{r}|$ in a cylindrical wire of radius R one has

$$V(q) = V_0 e^{R^2(q^2+\alpha^2)} E_1 \left[R^2(q^2 + \alpha^2) \right] \qquad (2.24)$$

with $E_1(z)$ the exponential integral function [62]. The resulting dispersion rela-
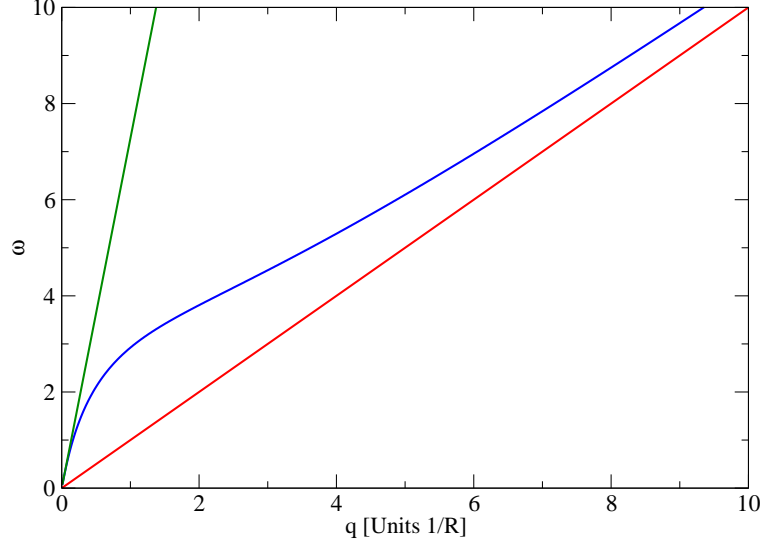
Figure 2.4: Dispersion relations $\omega_\nu(q)$ in units v_F/R as a function of q in units R^{-1} for the case of a Yukawa-type electron interaction. The parameters are $V_0/v_F = 91$ and $\alpha^{-1} = 10R$. The red curve is dispersion of the noninteracting spin density waves, the blue one that of the charge density waves. The linearized dispersion law for $q \to 0$, $\omega_\rho(q) = qv_F/g_\rho$ with $g_\rho = 0.13$, is displayed in green.

tions are displayed in Fig. 2.4. The strong renormalization of the charge sector (blue curve) with respect to the spin one (red curve) is clearly visible. It is important to observe that for $q \to 0$, the charge spectrum may in general be linearized to yield $\omega_\rho(q) = v_F|q|/g_\rho$. Therefore, for the low-energy excitations around $q \approx 0$, one can linearize the real $\omega_\rho(q)$ (green curve), defining an effective g_ρ. This procedure becomes exact in the extreme limit of zero range interactions $V(x - x') = V_0 \delta(x - x')$ where one gets $g_\rho^{-2} = 1 + 2V_0/\pi v_F$. This is the limit we will consider from now on.

2.2.3 Bosonization

The Luttinger liquid model allows to express the real-space representation of the Fermionic creation (annihilation) operators for the branch r and spin s, $\Psi_{r,s}^\dagger(x)$ ($\Psi_{r,s}(x)$), in terms of the bosonic density operators $\rho_{r,s}(q)$. This procedure, going under the name of bosonization, has been formalized by Haldane [54] in the case of spinless electrons. Here, we follow a similar approach [14]. Suppose to start with a noninteracting system. The first step towards the construction of the creation operator is the definition of a ladder operator $U_{r,s}^\dagger$,

whose action is to increase by one the number of electrons in branch r with spin s

$$U_{r',s'}^{\dagger}|\{N_{r,s}\}\rangle = |\{N_{r,s} + \delta_{r,r'}\delta_{s,s'}\}\rangle \tag{2.25}$$

where $|\{N_{r,s}\}\rangle$ represents the state with $N_{r,s}$ extra electrons with respect to the filled Fermi sea, with spin s and in branch r. The extra electrons are supposed to be stacked starting from the Fermi momentum k_F, each $\delta k = 2\pi/L$ apart in the momentum space. As a first guess one can assume to put the extra electron in the lowest available momentum state in the most trivial way

$$U_{r,s}^{\dagger} = L^{-1/2}\sum_{k} c_{r,k,s}^{\dagger}\,\delta\left(k - r\left[k_F + \frac{(2N_{r,s}+1)\pi}{L}\right]\right) \tag{2.26}$$

or, exploiting the position representation for $c_{r,k,s}$,

$$U_{r,s}^{\dagger} = L^{-1/2}\int_0^L dx\, e^{irk_F x} e^{-i\phi_{r,s}^{\dagger}(x)}\Psi_{r,s}^{\dagger}(x)e^{-i\phi_{r,s}(x)} \tag{2.27}$$

where $\phi_{r,s}(x) = -r\pi N_{r,s}x/L$. This operator, however, does not commute with the bosonic operators as it can be checked straightforwardly. A suitable modification to the field $\phi_{r,s}(x)$ allows to take care of this fact. Indeed, with

$$\phi_{r,s}(x) = -r\frac{\pi N_{r,s}}{L}x + \lim_{\alpha\to 0}\frac{2\pi i}{L}\sum_{p\neq 0}\frac{e^{-\alpha|p|/2}e^{-ipx}}{|p|}\theta(rp)\rho_{r,s}(-p) \tag{2.28}$$

the operator $U_{r,s}^{\dagger}$ satisfies $[\rho_{r,s}(q \neq 0), U_{r,s}^{\dagger}] = 0$. Moreover, expanding the operator $\exp[-i\phi_{r,s}^{\dagger}(x)]$ in (2.27) with the definition (2.28) it can be checked [54] that the ladder operator has the required property (2.25). Upon defining the usual charge- and spin-resolved linear combinations

$$\Phi_{\rho,\sigma}(x) = \frac{1}{\sqrt{2}}\sum_{r}[\phi_{r,+}(x) \pm \phi_{r,-}(x)]$$

and inverting (2.27), one gets the bosonized form of the creation operator $\Psi_{r,s}^{\dagger}(x)$, which correctly satisfies the canonical commutations,

$$\Psi_{r,s}^{\dagger}(x) = \lim_{\alpha\to 0}\frac{e^{-ir(k_F-\pi/L)x}}{\sqrt{2\pi\alpha}}U_{r,s}^{\dagger}\exp\left\{\frac{i}{\sqrt{2}}[\Lambda_{\rho}(x) + s\Lambda_{\sigma}(x)]\right\} \tag{2.29}$$

with

$$\Lambda_{\nu}(x) = r\Phi_{\nu}(x) - \pi\int_{-\infty}^{x} dx'\,\Pi_{\nu}(x')\,.$$

The fermionic operator has been expressed in terms of two canonically conjugated bosonic fields

$$\Phi_{\nu}(x) = -\frac{\pi x}{L}N_{\nu} - i\frac{\pi}{L}\sum_{p\neq 0}\frac{e^{-\alpha|p|/2}e^{-ipx}}{p}\left[\sum_{r}\nu_r(p)\right] \tag{2.30}$$

$$\Pi_{\nu}(x) = \frac{1}{L}J_{\nu} + \frac{1}{L}\sum_{p\neq 0}e^{-\alpha|p|/2}e^{-ipx}\left[\sum_{r}r\nu_r(p)\right]\,, \tag{2.31}$$

satisfying

$$[\Phi_\nu(x), \Pi_{\nu'}(y)] = i\delta_{\nu,\nu'}\delta(x-y).$$

The total charge and spin densities $d_\nu(x)$ are readily obtained:

$$d_\nu(x) = -\frac{\sqrt{2}}{\pi}\partial_x\Phi_\nu(x). \tag{2.32}$$

Note that the density can be decomposed as $d_\nu(x) = d_\nu^0 + \tilde{d}_\nu(x)$. The term d_ν^0 stems from the zero modes N_ν in $\Phi_\nu(x)$, while the term $\tilde{d}_\nu(x)$ is the zero-average density waves contribution. From the continuity equation $\partial_t d_\nu(x) = -\partial_x j_\nu(x)$, we can obtain the current density operators

$$j_\nu(x) = -\frac{\sqrt{2}}{\pi}\dot{\Phi}_\nu(x). \tag{2.33}$$

Turning to the interacting case – and restricting to the case of point-like interactions – under the Bogoljubov transformation the fields $\Phi_\nu(x)$ and $\Theta_\nu(x)$ undergo the transformation

$$\Phi_\nu(x) \quad \rightarrow \quad \tilde{\Phi}_\nu(x) = \Phi_\nu(x)\sqrt{g_\nu} \tag{2.34}$$

$$\Theta_\nu(x) \quad \rightarrow \quad \tilde{\Theta}_\nu(x) = \frac{\Theta_\nu(x)}{\sqrt{g_\nu}}, \tag{2.35}$$

therefore the bosonized form of the Fermionic operator is simply (2.29), with the substitutions $\Phi_\nu(x) \rightarrow \tilde{\Phi}_\nu(x)$ and $\Theta_\nu(x) \rightarrow \tilde{\Theta}_\nu(x)$. Exploiting the bosonic fields it is possible to rewrite the Hamiltonian of the interacting system in an extremely symmetric fashion

$$H = \frac{v_F}{2\pi}\sum_\nu \int_0^L dx \left[(\partial_x\Theta_\nu(x))^2 + \frac{1}{g_\nu^2}(\partial_x\Phi_\nu(x))^2\right] \tag{2.36}$$

2.2.4 Open boundary Tomonaga-Luttinger liquid

In this section we will describe a Luttinger liquid with open-boundary conditions [63–65]. Namely, we will suppose the system to be confined in the finite region $[0, L]$ by infinite walls, imposing therefore the boundary conditions

$$\psi_s(0) = \psi_s(L) \equiv 0 \tag{2.37}$$

on the annihilation operator for an electron with spin s. Taking the Fourier transform of $\psi_s(x)$ and exploiting the boundary conditions, we get $\psi_s(x) = \sqrt{2/L}\sum_p \sin(px)c_{p,s}$ where $c_{p,s}$ is the annihilation operator for an electron with momentum p and spin s and $p \equiv p_n = \pi n/L$, with n a positive integer. Expanding $\psi_s(x)$ around the Fermi momentum k_F we obtain

$$\psi_s(x) = \sum_r e^{irk_Fx}\psi_{r,s}(x) \tag{2.38}$$

with

$$\psi_{r,s}(x) = -\frac{ir}{\sqrt{2L}}\sum_{p>0} e^{irpx}c_{k_F+p,s}. \tag{2.39}$$

In contrast with the periodic boundary case, the fields (2.39) are linearly dependent, satisfying $\sum_r \psi_{r,s}(-rx) = 0$. Therefore, it is possible to describe the model using only one of the two $\psi_{r,s}(x)$: in the following we will work with right-moving ($r = +$) operators. In doing so, we notice that from the condition $\psi_s(L) = 0$ we obtain $\psi_{+,s}(-L) = \psi_{+,s}(L)$. It is tempting to regard the model as a single-branch LL, defined on the whole x axis, with periodic boundary conditions. Although this approach is straightforward in the case of a noninteracting system, things get slightly more involved when electronic interactions are considered. The position representation of the density operators for electrons in branch r and spin s is simply $\tilde{\rho}_{r,s} = \psi_{r,s}^\dagger(x)\psi_{r,s}(x)$. Notice that $\tilde{\rho}_{+,s}(x) = \tilde{\rho}_{-,s}(-x)$. We can define as well the charge-resolved ($\rho_r(x)$) and spin-resolved ($\sigma_r(x)$) density operators as in section 2.2.2

$$\rho_r(x) = \frac{1}{\sqrt{2}}\left[\tilde{\rho}_{r,+}(x) + \tilde{\rho}_{r,-}(x)\right]$$

$$\sigma_r(x) = \frac{1}{\sqrt{2}}\left[\tilde{\rho}_{r,+}(x) - \tilde{\rho}_{r,-}(x)\right].$$

$$(2.40)$$

We consider zero-range interactions $V(x - x') = V_0\delta(x - x')$ and restrict to forward scattering. In the charge sector one can rewrite the interaction term (2.16) in position representation

$$H_{\text{int}} = V_0 \int_0^L dx \sum_r \rho_r(x)\rho_r(x) + 2V_0 \int_0^L dx\, \rho_+(x)\rho_-(x) \qquad (2.41)$$

with V_0 the interaction strength. The first term in (2.41) can be simply rewritten, using boundary conditions, as a local interaction

$$H_{\text{int}}^{(1)} = V_0 \int_{-L}^L dx\, \rho_+(x)\rho_+(x) \qquad (2.42)$$

while the second term in (2.41) is recast as a nonlocal interaction

$$H_{\text{int}}^{(2)} = V_0 \int_{-L}^L dx\, \rho_+(x)\rho_+(-x). \qquad (2.43)$$

Notice that the bosonic part of (2.15) can be rewritten in the same fashion as (2.42)

$$H_{0,\rho} = \pi v_{\text{F}} \int_{-L}^L dx\, \rho_+(x)\rho_+(x) \qquad H_{0,\sigma} = \pi v_{\text{F}} \int_{-L}^L dx\, \sigma_+(x)\sigma_+(x).$$

Going back to the momentum representation we obtain the Hamiltonian of the system, rewritten in terms of the right-moving electrons only, defined on a set of double length $L \to 2L$

$$\begin{aligned}
H &= \frac{\pi v_{\text{F}} + V_0}{2L}\sum_{q \neq 0}\rho_+(q)\rho_+(-q) + \frac{V_0}{2L}\sum_{q \neq 0}\rho_+(q)\rho_+(q) + \frac{\pi v_{\text{F}} + 2V_0}{4L}N_\rho^2 \\
&+ \frac{\pi v_{\text{F}}}{2L}\sum_{q \neq 0}\sigma_+(q)\sigma_+(-q) + \frac{\pi v_{\text{F}}}{4L}N_\sigma^2 \qquad (2.44)
\end{aligned}$$

Note that we have explicitly separated the $q \to 0$ modes of the $\rho_+(q)$ operators, $N_{\rho,\sigma}$. In analogy with (2.21) we can define (properly normalized) bosonic operators $b_\nu^\dagger(q) = \sqrt{\pi/Lq}\, \nu_+(q)$. We can recast the Hamiltonian in the form

$$
H = \sum_\nu \sum_{q>0} \left\{ q \left[(v_{\mathrm{F}} + \alpha_\nu)\, b_\nu^\dagger(q) b_\nu(q) + \beta_\nu \left(b_\nu^\dagger(q) b_\nu^\dagger(q) + b_\nu(q) b_\nu(q) \right) \right] \right\} +
$$
$$
\frac{\pi v_{\mathrm{F}} + \gamma_\nu}{4L} N_\nu^2 \tag{2.45}
$$

with

$$
\begin{aligned}
\alpha_\rho &= \frac{V_0}{\pi} & \beta_\rho &= \frac{V_0}{2\pi} & \gamma_\rho &= 2V_0 \\
\alpha_\sigma &= 0 & \beta_\sigma &= 0 & \gamma_\sigma &= 0\,.
\end{aligned}
$$

Eq. (2.45) is readily diagonalized with a Bogoljubov transform obtaining a result formally similar to (2.22,2.23)

$$
H = \sum_\nu \left[\sum_{q>0} \omega_\nu(q) b_\nu^\dagger b_\nu(q) + \frac{\pi v_{\mathrm{F}}}{4L g_\nu^2} N_\nu^2 \right], \tag{2.46}
$$

where $\omega_\nu(q) = v_{\mathrm{F}} q/g_\nu$, $g_\rho = 1/\sqrt{1 + 2V_0/\pi v_{\mathrm{F}}}$ and $g_\sigma = 1$. The zero mode operators eigenvalues satisfy the constraint $N_\rho + N_\sigma = $ even [64]. Important differences with the periodic boundary condition case must be stressed. First of all, the sum over momenta is restricted to the positive values only. This is a direct consequence of the symmetry $\sum_r \psi_{r,s}(-rx) = 0$, which allows to describe the system using only one type of movers. This, in turn, leads to the presence of *only one zero-mode term* in either the charge and the spin sector, namely N_ν, in contrast with the periodic boundary case. Indeed, the topologic currents $(\nu = \rho, \sigma)$

$$
J_\nu = \nu_+(q \to 0) - \nu_-(q \to 0) \equiv \int_0^L \mathrm{d}x \, \left[\nu_+(x) - \nu_-(-x) \right]
$$

are not conserved in this model, as it becomes clear re-writing them in full detail

$$
J_\nu = 2i \sum_{q>0} \sqrt{\frac{L}{\pi q}} \left[\cos(qL) - 1 \right] \left[b_\nu^\dagger(q) - b_\nu(q) \right]. \tag{2.47}
$$

The dynamical separation of spin and charge velocities, however, is not affected by the boundary conditions, as can be understood from the explicit form of the spectrum of excitations.

Also this model can be bosonized, in the same spirit as the periodic boundary conditions case [63]. We first of all quote the bosonized expression for the spin-resolved density operator for the branch $r = +$

$$
\rho_{+,s}(x) = \frac{N_s}{2L} + \frac{\partial_x \Xi_s(x)}{2\pi} \tag{2.48}
$$

where $\Xi(x)$ is a phase field defined as

$$
\Xi_s(x) = \sum_{q>0} \sqrt{\frac{\pi}{qL}} e^{-\alpha q/2} \left(e^{iqx} b_q + \mathrm{h.c.} \right) \tag{2.49}
$$

and α^{-1} is a momentum cutoff. Because of the open boundary conditions $\Xi(x + 2L) = \Xi(x)$. For the creation operator of a Fermion with spin s, one has

$$\psi_s^\dagger(x) = \lim_{\alpha \to 0} \frac{U_s^\dagger}{\sqrt{2\pi\alpha}} e^{-i[\lambda_\rho(x) + s\lambda_\sigma(x)]} \tag{2.50}$$

with

$$\lambda_\nu(x) = \frac{\pi N_\nu x}{2L} + \left(\sqrt{\frac{g_\nu}{2}} - \frac{1}{\sqrt{2g_\nu}} \right) \frac{\Xi_\nu(x)}{2} + \left(\sqrt{\frac{g_\nu}{2}} + \frac{1}{\sqrt{2g_\nu}} \right) \frac{\Xi_\nu(-x)}{2} \tag{2.51}$$

2.2.5   Spinless periodic Tomonaga-Luttinger liquid

In this section, a few results for a spinless LL with periodic boundary conditions are summarized. The derivation goes along the same lines of section 2.2.2, therefore all the details will be omitted. The system still has two branches of left ($r = -1$) and right ($r = +1$) moving electrons. We denote the excess number of these electrons by N_r. We can as well define a density operator $\rho_r(p) \equiv \sum_k c_{r,k+p}^\dagger c_{r,k}$ for the branch r, where $c_{r,k}$ ($c_{r,k}^\dagger$) is the annihilation (creation) operator for an electron with momentum k in a given branch. The total Hamiltonian including interactions reads

$$\begin{aligned} H = &\frac{\pi v_{\mathrm{F}}}{L} \left[\sum_{r,p} : \rho_r(p)\rho_r(-p) : + \frac{N^2 + J^2}{2} \right] + \\ &\frac{1}{L} \sum_p V(p) \left[\rho_+(p)\rho_-(-p) + \frac{1}{2} \sum_r : \rho_r(p)\rho_r(-p) : \right] \end{aligned} \tag{2.52}$$

where the total excess electrons number $N \equiv N_+ + N_-$ and the imbalance between right- and left-moving extra electrons $J = N_+ - N_-$ operators have been defined. Their eigenvalues satisfy $N + J =$ even voit. The Hamiltonian (2.52) is diagonalized by a Bogoljubov transformation. Defining bosonic creation operators

$$b^\dagger(p) = \sqrt{\frac{2\pi}{L|p|}} \sum_r \theta(rp)\rho_r(p) \tag{2.53}$$

the diagonal form of (2.52) is

$$H = \sum_{p \neq 0} \omega(p) b^\dagger(p) b(q) + \frac{\pi v_{\mathrm{F}}}{2Lg^2} N^2 + \frac{\pi v_{\mathrm{F}}}{2L} J^2 \tag{2.54}$$

where $\omega(p) = v_{\mathrm{F}}|p|/g(p)$ and

$$g(p)^{-1} = \sqrt{1 + \frac{2V(p)}{\pi v_{\mathrm{F}}}}$$

is the spinless interaction parameter. The bosonization procedure can be performed, obtaining the fermionic creation operator in branch r

$$\Psi_r^\dagger(x) = \lim_{\alpha \to 0} \frac{e^{-ir(k_{\mathrm{F}} - \pi/L)x}}{\sqrt{2\pi\alpha}} U_r^\dagger \exp \left\{ i \left[r\Phi(x) - \pi \int_{-\infty}^x dx'\, \Pi(x') \right] \right\}, \tag{2.55}$$

where $U_r^\dagger$ is the increasing ladder operator acting on N_r and

$$\Phi(x) \;=\; -\frac{\pi x}{L}N - i\frac{\pi}{L}\sum_{p\neq 0}\frac{e^{-\alpha|p|/2}e^{-ipx}}{p}\left[\sum_r \rho_r(p)\right] \tag{2.56}$$

$$\Pi(x) \;=\; \frac{\pi}{L}J + \frac{1}{L}\sum_{p\neq 0}e^{-\alpha|p|/2}e^{-ipx}\left[\sum_r r\rho_r(p)\right] \tag{2.57}$$

are canonically conjugated bosonic fields. In the zero-range interaction approximation, to which we will stick in the following, the Hamiltonian can be rewritten as

$$H = \frac{v_{\rm F}}{2\pi}\int_0^L \mathrm{d}x \left[(\partial_x\Theta(x))^2 + \frac{1}{g^2}(\partial_x\Phi(x))^2\right]. \tag{2.58}$$

Part II

Spin-charge separation and transport

One-dimensional quantum dot

"No man is an island" (**J. Donne**)

In this chapter, we will develop a model for a spinful quantum dot embedded in a one-dimensional electron system. The system will be modeled using a LL with spin, introduced in chapter 2. After a general description of the system (section 3.1), the energy scales of the quantum dot will be introduced (section 3.2). The sequential tunneling through the dot will be addressed: a master equation for the occupation probability of the states of the dot will be described and transition rates will be calculated, addressing the very recent [18] issue of the relaxation of the collective excitations in the dot (section 3.3). A phenomenological extension, to include spin-flip effects in the master equation, will close this chapter.

3.1 The dot model

The system we are going to consider is schematically depicted in Fig. 3.1 (left). It consists of a one-dimensional quantum dot, which we will describe as a finite-size LL ($|x| < a/2$) with charge and spin interaction parameters g_ρ and g_σ, connected to one-dimensional left ("L") and right ("R") leads ($-L < x < -a/2$ and $a/2 < x < L$ respectively, with $L \to \infty$) via tunneling barriers placed at $x = \mp a/2$. We assume the possibility to have interacting 1D leads and we adopt for them a LL description as well, with a different charge interaction parameter g_0. For simplicity, we assume the charge interaction parameter to be the same for both the wires, and we assume to have $g_\sigma^{(\text{leads})} \equiv 1$. Possible experimental realizations of such a system could be the low-density 1D CEO channels, where a behavior consistent with the presence of a quantum dot defined by two impurities has been observed [8] (see section 1.5.1). Despite the fact that the quantum dot is embedded in the same 1D system defining the leads, the interaction parameters in different regions can have different values because of inhomogeneities along the channel or other effects

such as the presence of external metallizations [67]. Also, the one-dimensional channels will be unavoidably connected to circuital metallic gates. In order to still detect interaction effects in the 1D leads, the temperature must be not too low [67]. The system is coupled to external gate (V_g) and bias (V) voltages.
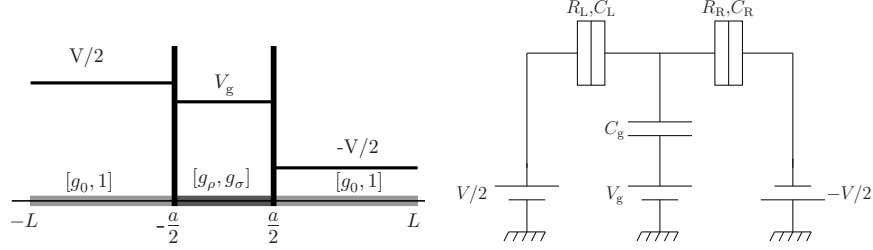
Figure 3.1: (Left) Scheme of the LL quantum dot ($|x| < a/2$) connected to semi-infinite, eventually interacting, one-dimensional wires. The charge (g_ρ) and spin (g_σ) interaction parameters in the dots and those in the leads are assumed to be different (see text). The gate voltage V_g affects the chemical potential of the quantum dot, while the bias voltage V defines the chemical potential difference of the leads. (Right) Circuital setup for the quantum dot with asymmetric tunneling barriers, where the L,R tunneling barriers are parametrized by resistances $R_{L,R} = \omega_c^2/\pi e^2 |t_{L,R}|^2$ (see text) and capacitances $C_{L,R}$. Here, ω_c is the cutoff energy of the leads, e the modulus of the charge of the electron and $t_{L,R}$ the transmission amplitudes of the L,R barriers.

The tunneling barriers can in principle be asymmetric, having different transparencies. The circuital setup corresponding to this system is shown in Fig. 3.1 (right). The total Hamiltonian of the system reads $H = H_0 + H_t + H_c$. The first term is the sum of the Hamiltonians of the uncoupled dot and leads: $H_0 = H_0^{(d)} + H_0^{(L)} + H_0^{(R)}$. The second term ($H_t$) describes the tunneling through the barriers, while H_c models the coupling to the external voltages. The dot is described as an open-boundary LL with spin (see section 2.2.4). This description relies on the linearization of the spectrum around the Fermi energy, which gives rise to the bare constant level spacing $\varepsilon_0 = \pi v_F/a$. In order for the linearization to be meaningful one needs to fulfill $E_F \gg \varepsilon_0$ (E_F Fermi energy), which can be rephrased as $k_F \gg \pi/a$. Moreover, we require $k_B T \ll \varepsilon_0$ in order to clearly resolve the level spacing. The Hamiltonian for the dot reads

$$H_0^{(d)} = \sum_\nu \sum_{q>0} \omega_\nu(q) b_\nu^\dagger(q) b_\nu(q) + \frac{\pi}{4a}\left[\frac{v_\rho}{g_\rho}\hat{n}^2 + \frac{v_\sigma}{g_\sigma}\hat{s}^2\right],\qquad(3.1)$$

with $q = \pi m/a$ ($m \geq 1$ is an integer). The collective excitations spectrum reads

$$\omega_\nu(q) = \frac{v_F}{g_\nu}q.\qquad(3.2)$$

The zero modes operators $\hat{n}$, $\hat{s}$ have eigenvalues n,s representing the excess total number of charge and spin (z component) with respect to their average values on the ground state. The latter correspond to $n_0 = 2k_F a/\pi - 1$ and $s_0 = 0$, since we are not considering external magnetic fields. The zero modes

eigenvalues are subject to the constraint $n + s =$ even. The energy contribution due to the zero modes represents the energy needed to change the total charge and/or spin with respect to the neutral condition.

The Hamiltonian for the leads ($\lambda = $ L, R) is ($L \gg a$)

$$H_0^{(\lambda)} = \sum_\nu \sum_{k>0} \Omega_\nu(k) b_{\nu,\lambda}^\dagger(q) b_{\nu,\lambda}(q) + \frac{\pi \bar{v}_F}{4L} \left[\frac{1}{g_0^2} \hat{n}_\lambda^2 + \hat{s}_\lambda^2 \right] , \qquad (3.3)$$

where $\bar{v}_F$ is the Fermi velocity of the leads and $k = \pi m / L$ with m a positive integer. All the leads operators have a λ suffix. The energy spectra for the collective excitations in the leads are $\Omega_\rho(k) = \bar{v}_F k / g_0$ and $\Omega_\sigma(k) = \bar{v}_F k$ respectively.

The tunneling Hamiltonian is given by

$$H_t = \sum_{s=\pm 1} \sum_{\lambda=L,R} \left[t_\lambda \psi_s^{(\lambda)\dagger}(x_\lambda) \psi_s^{(d)}(x_\lambda) + \text{h.c.} \right] \qquad (3.4)$$

where $x_L = -a/2$, $x_R = a/2$ and $t_{L,R}$ is the transmission amplitude. Note that in (3.4) the *right-movers'* operators are involved [63] (see section 2.2.4).

The Hamiltonian describing the coupling to the external voltages, which takes into account the circuital setup depicted in Fig. 3.1 (right), is

$$H_c = \frac{eV}{2} [\hat{n}_R - \hat{n}_L] - e \left[\frac{\delta C}{C_\Sigma} \frac{V}{2} + \frac{C_g}{C_\Sigma} V_g \right] \hat{n} , \qquad (3.5)$$

where we have denoted $\delta C = C_L - C_R$ and the total capacitance $C_\Sigma = C_L + C_R + C_g$.

3.2 Energy scales

Since the energy scales of the quantum dot play a fundamental role in defining its transport properties, especially in connection with the spin-charge separation phenomenon, it is useful to give here a detailed discussion. An eigenstate of the Hamiltonian (3.1), which identifies a state of the 1D quantum dot, is determined by

$$|\mathcal{S}\rangle = \left| n, s, \left\{ l_q^{(\rho)} \right\}, \left\{ l_q^{(\sigma)} \right\} \right\rangle , \qquad (3.6)$$

namely by n and s, the zero modes eigenvalues describing the number of excess charges and the excess spin, together with the occupation numbers $\left\{ l_q^{(\rho,\sigma)} \right\}$ describing the harmonic collective charge and spin modes. The total energy of such a state is readily obtained as

$$\mathcal{U}(\mathcal{S}) = \frac{E_\rho}{2} n^2 + \frac{E_\sigma}{2} s^2 + \varepsilon_\rho l_\rho + \varepsilon_\sigma l_\sigma \qquad (3.7)$$

where, upon inspection of (3.1), we identify the *charge ($\nu = \rho$) and spin ($\nu = \sigma$) addition energies* $E_\nu = \pi v_\nu / 2 a g_\nu$ and $\varepsilon_\nu = \pi v_\nu / a$, the CDW/SDW excitation quanta. Here, we have defined $l_\nu = \sum_q q l_q^\nu$. The linearity of the dispersion relations of CDWs and SDWs gives rise to a degeneracy in the energies of the dot

collective modes which increases with increasing energy. Recalling the noninteracting constant levelspacing $\varepsilon_0 = \pi v_{\mathrm{F}}/a$, we have

$$E_\nu = \frac{\varepsilon_0}{2g_\nu^2}\,. \tag{3.8}$$

Because of the Pauli exclusion principle, even in the noninteracting ($g_\nu = 1$) case the addition energies are nonzero. Despite a theoretical estimate for the charge addition energy E_ρ is provided directly within the LL model, many physical effects such as the influence of external metallic gates or inhomogeneous interactions are missed by this simple model. Since these effects might cause strong deviations to the above result, in the following we will treat E_ρ as a free parameter, assuming it as the largest of the four energy scales introduced independent of the interaction parameters. The spin addition energy is

$$E_\sigma = \frac{\varepsilon_0}{2}\,. \tag{3.9}$$

In the following, in order to emphasize the spin-charge separation effects, a weakly interacting spin sector will be considered ($g_\sigma \gtrsim 1$): this slightly depresses the value of E_σ and weakly renormalizes the charge sector. The CDW and SDW quanta are given respectively by

$$\varepsilon_\sigma = 2E_\sigma g_\sigma \qquad\qquad \varepsilon_\rho = \varepsilon_\sigma \frac{g_\sigma}{g_\rho}\,. \tag{3.10}$$

It is important to notice that, in a noninteracting system ($g_\rho = g_\sigma = 1$) $\varepsilon_\rho \equiv \varepsilon_\sigma \equiv \varepsilon_0$. The presence of interactions gives rise to the spin-charge phenomenon. One of its manifestations is the removal of the degeneracy between the energy of CDWs and SDWs. A sort of hierarchy in the four energy scales arises (the equalities holding in the noninteracting case)

$$E_\sigma < \varepsilon_\sigma \leq \varepsilon_0 \leq \varepsilon_\rho < E_\rho\,,$$

from which is clear that E_σ has the natural role of the energy scale for the system under investigation. In the following we will always assume this. From a phenomenological point of view, it is usual to identify E_ρ with the total electrostatic energy of a dot with one extra electron: $E_\rho = e^2/C_\Sigma$. With this identification, we notice that the term $-eC_{\mathrm{g}}V_{\mathrm{g}}\hat{n}/C_\Sigma$ in (3.5) can be rewritten as $-E_\rho n_{\mathrm{g}}\hat{n}$, where $n_{\mathrm{g}} = C_{\mathrm{g}}V_{\mathrm{g}}/e$ is the number of charges induced by the gate voltage. Since in the following we will be interested in energy differences among states with different n, it is possible to combine this latter term with the charge addition term, in order to obtain the total energy of a dot state

$$\mathcal{U}\left(\mathcal{S}, n_{\mathrm{g}}\right) = \frac{E_\rho}{2}\left(n - n_{\mathrm{g}}\right)^2 + \frac{E_\sigma}{2}s^2 + \varepsilon_\rho l_\rho + \varepsilon_\sigma l_\sigma\,. \tag{3.11}$$

Some examples of dot states $|\mathcal{S}\rangle$ are displayed in Fig. 3.2. Figures 3.2 (a,b) represent respectively one of the two degenerate ground states for $n = 1$ extra electrons, and the ground state for $n = 2$. The reference value is gray-shaded in the plot. It is clear, from (3.7,3.11), that two different states with the same extra electrons number n but opposite spin are degenerate. Therefore, there exist two degenerate ground states for an *odd* number of extra electrons in the dot,
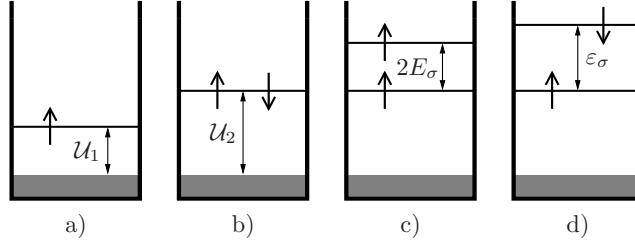
Figure 3.2: Some examples of dot states $|\mathcal{S}\rangle$. The gray-shaded region represents the dot reference state, with $n_0 = 2k_F a/\pi - 1$ and $s_0 = 0$. a) The state $\left|1, 1, \vec{0}, \vec{0}\right\rangle$, one of the two degenerate ground states for a dot with one extra electron; b) The state $\left|2, 0, \vec{0}, \vec{0}\right\rangle$, ground state for a dot with two extra electrons; c) The spin-polarized excited state $\left|2, 2, \vec{0}, \vec{0}\right\rangle$; d) One of the components of the lowest lying SDW built ontop of the ground state for two extra electrons, $|2, 0, \{0, 0, \ldots\}, \{1, 0, \ldots\}\rangle$. The energies of these states are respectively a) $\mathcal{U}_1 = (E_\rho + E_\sigma)/2$; b) $\mathcal{U}_2 = 2E_\rho$; c) $\mathcal{U} = 2E_\rho + 2E_\sigma$; d) $\mathcal{U} = 2E_\rho + \varepsilon_\sigma$. Here we have put $n_g = 0$ for ease of notation.

with spin $s = \pm 1$. The ground state for an odd number of electrons is unique, and has spin $s = 0$. Along with ground states, it is possible to create polarized excited states with a total spin $s > 1$. An example for $n = 2$, with $s = 2$, is depicted in Fig. 3.2 (c). It must be stressed that, because of the degeneracy of states with opposite spin and equal number of electrons, the excited state with all spins reversed ($s = -2$) is perfectly allowed as well. In the absence of an external magnetic field, because of this energetic degeneracy *no net polarization of the dot can be achieved in the stationary transport limit*. Finally, it is possible to excite collective charge or spin density waves inside the dot. Consider the action of the operator $b_\sigma^\dagger(\pi/a)$ over the ground state for $n = 2$ extra electrons (from now on, we will drop the "extra" label)

$$b_\sigma^\dagger(\pi/a)\,|2, 0, \{0, 0, \ldots\}, \{0, 0, \ldots\}\rangle = |2, 0, \{0, 0, \ldots\}, \{1, 0, \ldots\}\rangle \ .$$

Browsing through the definitions of the bosonic creation operators (sections 2.2.4, 2.2.2), the explicit form of this operator is

$$b_\sigma^\dagger(\pi/a) = \frac{1}{\sqrt{2}}\left[\rho_{+,+}(\pi/a) - \rho_{+,-}(\pi/a)\right] \tag{3.12}$$

where $\rho_{+,s}(\pi/a) \equiv \sum_p c_{+,p+\pi/a,s}^\dagger c_{+,p,s}$. Since the confinement imposes a momentum quantization inside the dot in units of π/a, the only possible action of the operator $\rho_{+,-}(\pi/a)$ on the ground state of $n = 2$ is to create the state in Fig. 3.2 (d), while the operator $\rho_{+,+}(\pi/a)$ creates a state similar to the latter, but with the topmost spins reversed. As it is clear from (3.12), the action of $b_\sigma^\dagger(\pi/a)$ on the aforementioned ground state creates an entangled excited state with total spin $s = 0$, with the two components described above. It is important to point out that charge or spin excitations with a higher momentum can

be created using operators $b_\nu^\dagger(q > \pi/a)$, as well as multiple excitations with different momenta, induced by operators of the general form

$$\prod_\nu \prod_{l_q^\gamma} \left[b_\nu^\dagger(q) \right]^{l_q^\gamma}.$$

3.3   Sequential tunneling

Let us now turn to the study of the transport properties of the LL quantum dot described in the previous sections. In the rest of this thesis I will concentrate on the *sequential tunneling regime*, thus neglecting cotunneling effects. This poses some restriction on the temperature range where the obtained results are valid: the coherent tunneling contributions can be neglected if $k_B T \gg \delta E$ [68], where δE is the level broadening due to higher order tunneling processes. For the case of noninteracting leads ($g_0 = 1$), this broadening is simply proportional to the tunneling rate prefactor (3.38). Since the broadening is only slightly renormalized for weakly interacting leads [68] and since this is the case of interest for the rest of the part, we assume the bound $k_B T \gg \delta E$. The first step towards the calculation of the stationary current and differential conductance in the sequential regime will be the set-up of a master equation for the occupation probabilities of the dot. In order to write the master equation, we first of all need to know which are the relevant dot states for a given set of parameters of the dot. In the low-temperature regime $\delta E < k_B T < \varepsilon_0$, the source-drain voltage V basically fixes the set of such states. In the following, we will stick to the regime $eV < E_\rho$. This assumption, together with $E_\rho > E_\sigma, \varepsilon_{\rho,\sigma}$, ensures that *at most two charge states n and n + 1 are involved in the transport process*. This does not rule out, of course, the possibility to create excited states in the dot as discussed in the previous section, since it is still possible to have $\varepsilon_\sigma, \varepsilon_\rho, E_\sigma < eV$. In section 3.3.1 we will introduce the master equation and the calculation for the tunneling rate with nonrelaxed excited states in the quantum dot. In section 3.3.2 we will approach the opposite limit of infinitely short relaxation time for the collective excitations in the dot, and modify the master equation in order to employ a phenomenological relaxation for the "spin-polarized" excited states. This latter regime is the one we will use in the following of this part.

3.3.1   Non-relaxed collective excitations

The dot states have the form $|n, s, C_n\rangle$ where C_n represents the set of occupation numbers for the charge and spin density waves of the state with a given n,s. The occupation probability for such a state will be denoted by P_{n,s,C_n}. The master equation reads

$$\partial_t P_{n,s,C_n}(t) = \sum_{n'} \sum_{s'=s\pm 1} \sum_{C_{n'} \neq C_n} P_{n',s',C_{n'}}(t) \Gamma_{|n',s',C_{n'}\rangle \to |n,s,C_n\rangle} \qquad (3.13)$$

$$-P_{n,s,C_n}(t)\Gamma_{|n,s,C_n\rangle \to |n',s',C_{n'}\rangle} \, ,$$

with $n' = n, n + 1$. Since we will deal with stationary transport properties, the l.h.s. must be put to zero. Thus, one is left with a set of linear equations. In order to proceed, we still need to calculate the *transition rates* $\Gamma_{|n,s,C_n\rangle \to |n',s',C_{n'}\rangle}$.

To the lowest order in H_t, this can be done by means of the golden rule. We start from

$$\Gamma^{(\lambda)}_{|i\rangle \to |f\rangle}(\Delta E) = \int dt \, e^{i(E_f - E_i)t} |\langle f|H_t|i\rangle|^2 \tag{3.14}$$

where $\Delta E = E_f - E_i$ and $E_{i,f}$ are the total energy of the initial/final states and we have introduced the shorthand notation $|i, f\rangle$ for the final and initial states of the *system*. They can be factorized in dot, left and right leads parts as

$$
\begin{aligned}
|i\rangle &= |n_d, s_d, C_{n_d}\rangle_i \cdot |n_L, s_L, C_{n_L}\rangle_i \cdot |n_R, s_R, C_{n_R}\rangle_i \\
|f\rangle &= |n_d, s_d, C_{n_d}\rangle_f \cdot |n_L, s_L, C_{n_L}\rangle_f \cdot |n_R, s_R, C_{n_R}\rangle_f .
\end{aligned}
$$

In a sequential tunneling event, the dot charge and spin must obey the selection rules already encoded in the master equation, namely $n_{d,f} = n_{d,i} \pm 1$ and $s_{d,f} = s_{d,i} \pm 1$. This requires a corresponding variation in either the left or the right lead: $n_{\lambda,f} = n_{\lambda,i} \pm 1$, $s_{\lambda,f} = s_{\lambda,i} \pm 1$, with $\lambda = L, R$. Therefore, one is left with 8 classes of events grouped accordingly to the table 3.1. For each of these

Δn	Δs	λ	**Type of event**
+1	+1	L	In ↑
+1	-1	L	In ↓
-1	+1	L	Out ↓
-1	-1	L	Out ↑
+1	+1	R	In ↑
+1	-1	R	In ↓
-1	+1	R	Out ↓
-1	-1	R	Out ↑

Table 3.1: Table of the eight possible classes of events depending on the type of tunneling process, determined by $\Delta n = n_{d,f} - n_{d,i}$, $\Delta s = s_{d,f} - s_{d,i}$, and the tunneling barrier λ.

events, one still has to specify $C_{n_{d,i}}$ and $C_{n_{d,f}}$. However, since we will perform a thermal average over the collective modes of the leads, it is not necessary to specify $C_{n_{L/R,i}}$ and $C_{n_{L/R,f}}$ in the rate. Let us sketch out in detail the calculation for the specific case of the transition with $\Delta n = 1$ and $\Delta s = 1$ (see table 3.1) on the barrier $\bar{\lambda}$. The only term in the tunneling Hamiltonian that gives a nonzero matrix element is (dropping the overbar on λ) $t^*_\lambda \psi^{(d)\dagger}_+(x_\lambda)\psi^{(\lambda)}_{+,+}(x_\lambda)$. Factorizing the initial and final states one obtains for the squared modulus of the matrix element in (3.14)

$$|t_\lambda|^2 \quad \cdot \left| \langle n_\lambda - 1, s_\lambda - 1, C_{n_\lambda - 1}|\psi^{(\lambda)}_+(x_\lambda)|n_\lambda, s_\lambda, C_{n_\lambda}\rangle \right|^2 \tag{3.15}$$

$$\cdot \left| \langle n_d + 1, s_d + 1, C_{n_d + 1}|\psi^{(d)\dagger}_+(x_\lambda)|n_d, s_d, C_{n_d}\rangle \right|^2 .$$

Recalling the structure of the Fermionic operators for open boundary conditions (2.50), we reabsorb the normalization factors inside $|t_\lambda|^2$ and contract the ladder operator between initial and final states. We are left with (to avoid con-

fusion, we have relabeled $\xi_\nu^{(d,\lambda)}$ the bosonic fields for the dot/lead)

$$|t_\lambda|^2 \left| \langle C_{n_\lambda-1}|e^{i[\xi_\rho^{(\lambda)}(x_\lambda)+\xi_\sigma^{(\lambda)}(x_\lambda)]}|C_{n_\lambda}\rangle \right|^2 \left| \langle C_{n_{\rm d}+1}|e^{-i[\xi_\rho^{(d)}(x_\lambda)+\xi_\sigma^{(d)}(x_\lambda)]}|C_{n_{\rm d}}\rangle \right|^2 \quad (3.16)$$
$$= |t_\lambda|^2 \varphi_\lambda \varphi_{\rm d} \,.$$

We plug (3.16) into (3.14), performing a sum over leads plasmonic final states and a thermal average over plasmonic leads initial states. We separate explicitly the total energy in the dot and leads contributions $E_{i,f} \equiv E_{i,f}^{(\rm d)} + E_{i,f}^{(\lambda)}$ and obtain

$$\Gamma_{|i\rangle \to |f\rangle}^{(\lambda)}(\Delta E) = |t_\lambda|^2 \varphi_{\rm d} \int {\rm d}t\, e^{i\left[E_f^{(\rm d)}-E_i^{(\rm d)}\right]t} \sum_{i,f} \frac{e^{-\beta E_i^{(\lambda)}}}{\mathcal{Z}} e^{i\left[E_f^{(\lambda)}-E_i^{(\lambda)}\right]t} \varphi_\lambda \qquad (3.17)$$

with $\beta^{-1} = k_{\rm B}T$. After some algebraic rearrangement we obtain (having defined $\xi^{(\lambda)}(x;t) \equiv \xi_\rho^{(\lambda)}(x,t) + \xi_\sigma^{(\lambda)}(x,t)$ as a shorthand notation)

$$\Gamma_{|i\rangle \to |f\rangle}^{(\lambda)}(\Delta E) = |t_\lambda|^2 \varphi_{\rm d} \int {\rm d}t\, e^{i\Delta E t} e^{-W_\lambda(t)} \qquad (3.18)$$

where

$$e^{-W_\lambda(t)} = \left\langle e^{-i\xi^{(\lambda)}(x_\lambda;t)} e^{i\xi^{(\lambda)}(x_\lambda;0)} \right\rangle_{\rm th} \qquad (3.19)$$

is the result of the trace over the lead collective excitations. By virtue of the bosonization language, this correlation function is easily evaluated The energy difference ΔE simply reads

$$\Delta E = \Delta E_{\rm coll.} + E_\rho \left(n_{\rm d} - n_{\rm g} + \frac{1}{2} \right) + E_\sigma \left(s_{\rm d} + \frac{1}{2} \right) - eV \frac{C_{\rm L} + C_{\rm g}/2}{C_\Sigma}$$

with $\Delta E_{\rm coll.}$ the difference of the energies of the collective charge and spin modes in the final/initial states. The factor $W_\lambda(t)$ can be explicitly evaluated

$$W_\lambda(t) = \int {\rm d}\omega\, \frac{J_\lambda(\omega)}{\omega^2} \left\{ \coth \left(\frac{\beta\omega}{2} \right) [1 - \cos(\omega t)] + i\sin(\omega t) \right\} \qquad (3.20)$$

and we have defined the leads spectral density

$$J_\lambda(\omega) = \frac{\omega}{g} e^{-\omega/\omega_{\rm c}} \,. \qquad (3.21)$$

Here, the effective interaction parameter $g^{-1} = (1 + g_0^{-1})/2$ for the leads and a cutoff energy $\omega_{\rm c}$ have been introduced. With the same procedure, it is possible to calculate all the tunneling rates entering the master equation (3.13). It turns out that the factor $W_\lambda(t)$ is independent of the barrier and of the spin. We can work out explicitly (3.18) obtaining

$$\Gamma_{|i\rangle \to |f\rangle}^{(\lambda)}(\Delta E) = \frac{|t_\lambda|^2}{\Gamma(g^{-1})} \varphi_{\rm d} e^{\beta\Delta E/2} \left| \Gamma \left(\frac{1}{2g} + i\frac{\beta\Delta E}{2\pi} \right) \right|^2 \left(\frac{2\pi}{\beta\omega_{\rm c}} \right)^{g^{-1}-1} \qquad (3.22)$$

with

$$\Delta E = \Delta E_{\rm coll.} + E_\rho \left[(n_{\rm d,i} - n_{\rm g}) \Delta n + \frac{1}{2} \right] + E_\sigma \left[s_{\rm d,i} \Delta s + \frac{1}{2} \right] - \frac{eV}{2} \left[\frac{\delta C}{C_\Sigma} \mp 1 \right] \Delta n \qquad (3.23)$$

where the sign $+ (-)$ refers to an event occurring on the left (right) barrier.

3.3.2 Fully relaxed collective excitations

Up to now, the excited states of the dot have been considered as infinitely stable states. Despite this is consistent with the fact that these are exact eigenstates of the dot Hamiltonian, in realistic systems this is usually not the case. A certain degree of relaxation, due to the coupling to phonons [14, 70] or spin-orbit interaction is in principle to be expected for the *excited* states of the dot. Also, the contribution of the neglected higher order tunneling terms can contribute to the relaxation of high-spin states. Although is very difficult to analyze microscopically these relaxation processes, very recently Khaetskii and Nazarov [69] have pointed out that in 1D quantum dots the relaxation processes that involve a spin-flip relaxation occur to much longer time scales than the ones which do not involve a total spin change. In the following, we will take into account the relaxation of collective modes. We will proceed as follows

1. we will assume an infinitely fast relaxation of the collective excitations, i.e. the CDWs and SDWs relax to the corresponding ground state before the next tunneling event occurs. This assumption will be commented later in this section;

2. In section 3.3.3 we will modify the master equation introducing a *phenomenological relaxation time* for the spin-polarized excited states, which we will subsequently treat as an external parameter.

We can implement the infinitely fast relaxation for the collective excitations as follows: suppose we can factorize the probability P_{n,s,C_n} as

$$P_{n,s,C_n} = P_{n,s}\pi_{C_n} \ . \tag{3.24}$$

We now make the assumption of thermal independent probability distributions for charge and spin collective excitations

$$\pi_{C_n} = \mathcal{Z}_\rho^{-1}\mathcal{Z}_\sigma^{-1}e^{-\beta\varepsilon_\rho[C_n]}e^{-\beta\varepsilon_\sigma[C_n]} \ . \tag{3.25}$$

where we recall C_ν is a placeholder for a particular set of occupation numbers $\{l_q^\rho\}, \{l_q^\sigma\}$ for given n and s, $\varepsilon_\nu[C_n] = \sum_q l_q^\gamma q\varepsilon_\nu$ and the $\mathcal{Z}_\nu$ are defined as

$$\mathcal{Z}_\nu = \sum_{\{l_q^\gamma\}} e^{-\beta\sum_q l_q^\gamma q\varepsilon_\nu} \ .$$

Plugging (3.24) in (3.13) and summing over all the initial state collective excitations configurations, in the stationary regime we obtain the *effective master equation*

$$\sum_{n'}\sum_{s'=s\pm1} P_{n',s'}\left[\sum_{\substack{C_{n'}\neq C_n \\ C_n\neq C_{n'}}} \pi_{C_{n'}}\Gamma_{|n',s',C_{n'}\rangle\to|n,s,C_n\rangle}\right] = \tag{3.26}$$

$$P_{n,s}\sum_{n'}\sum_{s'=s\pm1}\left[\sum_{\substack{C_{n'}\neq C_n \\ C_n\neq C_{n'}}} \pi_{C_n}\Gamma_{|n,s,C_n\rangle\to|n',s',C_{n'}\rangle}\right] \ .$$

Note that the only degrees of freedom we are left with, are the total charge n and total spin s. We can define an *effective* tunneling rate as

$$\Gamma^{(\lambda)}_{|n,s\rangle\to|n',s'\rangle} = \sum_{\substack{C_{n'}\neq C_n \\ C_n\neq C_{n'}}} \pi_{C_n} \Gamma^{(\lambda)}_{|n,s,C_n\rangle\to|n',s',C_{n'}\rangle} . \tag{3.27}$$

Explicitly, the effective tunneling rate reads

$$\Gamma_{|n,s\rangle\to|n',s'\rangle} = |t_\lambda|^2 \int \mathrm{d}t\, e^{i\left[E_f^{(0)}-E_i^{(0)}\right]t} e^{-W_\lambda(t)} \sum_{\substack{C_{n_\mathrm{d}+1}\neq C_{n_\mathrm{d}} \\ C_{n_\mathrm{d}}\neq C_{n_\mathrm{d}+1}}} \pi_{C_{n_\mathrm{d}}} e^{i\Delta E_\mathrm{coll.}} \varphi_\mathrm{d} . \tag{3.28}$$

Performing some algebraic rearrangement, we treat the last term in (3.28) in the same way as we did for the collective excitations in the leads. We obtain

$$\Gamma^{(\lambda)}_{|n,s\rangle\to|n',s'\rangle}(\Delta E') = |t_\lambda|^2 \int \mathrm{d}t\, e^{i\Delta E't} e^{-W_\lambda(t)} e^{-W_\mathrm{d}(t)} \tag{3.29}$$

where

$$e^{-W_\mathrm{d}(t)} = \left\langle e^{-i\xi^\mathrm{d}(x_\lambda;t)} e^{i\xi^\mathrm{d}(x_\lambda;0)} \right\rangle_\mathrm{th} \tag{3.30}$$

is now the result of the trace over the dot collective modes. The energy difference $\Delta E' = E_f^{(0)} - E_i^{(0)}$, which takes into account only the zero-modes contributions and the applied voltages, now reads

$$\Delta E' = E_\rho \left[\left(n_{\mathrm{d},i} - n_\mathrm{g}\right) \Delta n + \frac{1}{2} \right] + E_\sigma \left[s_{\mathrm{d},i}\Delta s + \frac{1}{2} \right] - \frac{eV}{2} \left[\frac{\delta C}{C_\Sigma} \mp 1 \right] \Delta n$$

With the definition of the *dot spectral density*

$$J_\mathrm{d}(\omega) = \omega \sum_\nu \frac{\varepsilon_\nu}{2g_\nu} \sum_{m=1}^\infty \delta(\omega - m\varepsilon_\nu) e^{-\omega/\omega_\mathrm{c}} . \tag{3.31}$$

we have

$$W_\mathrm{d}(t) = \int \mathrm{d}\omega\, \frac{J_\mathrm{d}(\omega)}{\omega^2} \left\{ \coth\left(\frac{\beta\omega}{2}\right) \left[1 - \cos\left(\omega t\right)\right] + i\sin\left(\omega t\right) \right\} . \tag{3.32}$$

Since the term $\exp\left[-W_\mathrm{d}(t)\right]$ can be factorized as $\exp\left[-W_\rho(t)\right] \exp\left[-W_\sigma(t)\right]$, where $\exp -W_\nu(t)$ is clearly periodic with period $2\pi/\varepsilon_\nu$, we can perform a double Fourier transformation to obtain

$$e^{-W_\nu(t)} = \sum_n a_\nu(n) e^{-in\varepsilon_\nu t} . \tag{3.33}$$

The weights $a_\nu(n)$ are evaluated in appendix A. Plugging (3.33) into (3.29) we finally have

$$\Gamma^{(\lambda)}_{|n,s\rangle\to|n',s'\rangle}(\Delta E) = \Gamma_0^{(\lambda)} \sum_{p=-1}^\infty \sum_{q=-1}^\infty a_\rho(p) a_\sigma(q) \gamma\left(\Delta E - p\varepsilon_\rho - q\varepsilon_\sigma\right) \tag{3.34}$$

with

$$a_\nu(q) = a_\nu^{(0)}(q) + \frac{e^{-\beta \varepsilon_\nu}}{2g_\nu} \left[a_\nu^{(0)}(q+1) + a_\nu^{(0)}(q-1) - 2a_\nu^{(0)}(q) \right]. \qquad (3.35)$$

Here, we have defined the zero-temperature weights

$$a_\nu^{(0)}(q) = \frac{\Gamma\left(1/2g_\nu + q\right)}{\Gamma\left(1/2g_\nu\right) q!} \theta(q), \qquad (3.36)$$

the leads contribution

$$\gamma(x) = \frac{1}{2\pi} e^{-\beta x/2} \left| \Gamma\left(\frac{1}{2g} + i\frac{\beta x}{2\pi}\right) \right|^2 \left(\frac{2\pi}{\beta \omega_c}\right)^\alpha, \qquad (3.37)$$

and the prefactor

$$\Gamma_0^{(\lambda)} = \prod_\nu \left(1 - e^{-\frac{\varepsilon_\nu}{\omega_c}}\right)^{\frac{1}{2g_\nu}} \frac{2\omega_c G_\lambda}{e^2 \Gamma(1+\alpha)}. \qquad (3.38)$$

Here, $\Gamma(z)$ represents the Euler gamma function [62]. The *effective* parameter interaction of the leads, $g^{-1} = (1 + g_0^{-1})/2$, the factor $\alpha = g^{-1} - 1$ and the intrinsic barriers conductance

$$G_\lambda = \frac{\pi e^2 |t_\lambda|^2}{\omega_c^2} \qquad (3.39)$$

have been defined. Note that the leads contribution (3.37) simply reduces to a Fermi function for noninteracting leads ($g_0 = 1$). The expression (3.35) holds only up to temperatures $k_B T < \min\{\varepsilon_\rho, \varepsilon_\sigma\}$. In the $T = 0$ limit, we have $a_\nu(q) \equiv a_\nu^{(0)}(q)$, and

$$\gamma(x) = \left(-\frac{x}{\omega_c}\right)^\alpha \theta(-x). \qquad (3.40)$$

 The rate (3.34) is plotted in Fig. 3.3 for an interacting (left) and a noninteracting (right) dot (see caption for parameters). Clearly, if $\Delta E = E_f - E_i$, the rate exhibits a step each time

$$E_f + p\varepsilon_\rho + q\varepsilon_\sigma < E_i.$$

The step-like structure of the rate is due to the reduction to an effective master equation consequent to the strong relaxation hypothesis for the collective modes. Indeed it is *always* possible for an electron, provided with enough energy, to tunnel into an excited state for the dot, with possibly charge and/or spin density waves. However, at very low temperatures $k_B T \ll \varepsilon_\nu$ the collective modes quickly relax before the next tunneling event occurs. In perfect analogy, an electron tunneling outside the dot can leave excited collective modes inside the dot, which promptly relax in the above mentioned limit. Therefore, an excited state is accessible as the *final* state of a transition, but not as the *initial* state. Increasing the temperature, but still for $k_B T < \varepsilon_\nu$, it is possible for a tunneling electron to pick up a single energy quantum from the thermal bath and subsequently excite modes with a slightly-higher energy (see
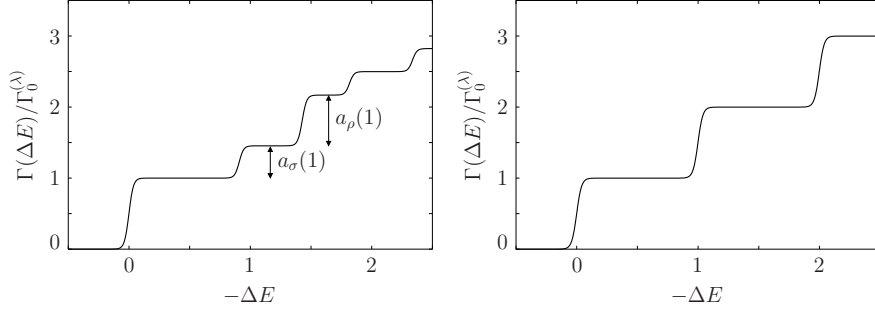
Figure 3.3: Plot of the normalized tunneling rates (3.34) as a function of the tunneling energy $-\Delta E$ (units E_σ) for an interacting dot ($g_\rho = 0.7, g_\sigma = 1.1$) (left) and a noninteracting dot ($g_\rho = g_\sigma = 1$) (right). Other parameters are $k_B T = 0.02 E_\sigma$ and noninteracting leads ($g_0 = 1$).

appendix A). Note that these final excited states relax nevertheless to the thermal bath. In the interacting case, the step height depends on the interaction parameters of the dot. It is crucial to notice that the height of the jumps are in general all different. On the contrary, if the interaction is removed and no spin-charge separation is anymore present inside the dot, the rate has the peculiar structure depicted in Fig. 3.3 (right), where a sequence of identical, unitary steps occur – see appendix B. Notice that the small temperature corrections to the step height are undetectable at the low temperatures considered in the figure. The effects of interactions in the leads is shown in Fig. 3.4. The leads
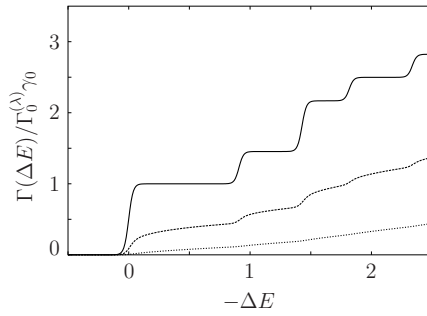
Figure 3.4: Plot of the tunneling rates (3.34), normalized to $\Gamma_0^{(\lambda)} \gamma_0$, where $\gamma_0 = (2\pi/\beta\omega_c)^\alpha$, as a function of the tunneling energy $-\Delta E$ (units E_σ) for an interacting dot ($g_\rho = 0.7, g_\sigma = 1.1$). (left) and a noninteracting dot ($g_\rho = g_\sigma = 1$) (right). The temperature is $k_B T = 0.02 E_\sigma$, $\omega_c = 50 E_\sigma$ and the leads interaction parameter is $g_0 = 1$ ($\alpha = 1$), $g_0 = 0.8$ ($\alpha \approx 0.89$), and $g_0 = 0.6$ ($\alpha = 0.75$) from top to bottom.

interactions smooth out the step-like structure of the tunneling rates, which moreover gets globally depressed – see also the normalization factor used in the figure.

Comments on fully relaxed collective excitations

It is interesting to consider to which extent the two approximations of non-relaxed (Sec. 3.3.1) and fully relaxed (Sec. 3.3.2) reflect on the transport properties of the dot. The presence of excited states becomes evident as differential conductance peaks in the nonlinear ($V > 0$) transport regime, whose position is determined by the energy of the collective modes. Since the dispersion relation of CDWs and SDWs is linear and because of the availability of collective excited states as the final states of a transition in the fully relaxed model, both the "fully relaxed" and the "non-relaxed" approximations may exhibit conductance peaks in the same position. Tunneling rates $\Gamma^{(\lambda)}_{|i\rangle \to |f\rangle}$, analogous to (3.22) but in the context of a *spinless* quantum dot created inside a LL with nonrelaxed plasmonic modes, were recently used by Kim *et al.* [18]. The out-of-equilibrium dynamics of the system was analyzed, the occupation probabilities for the collective excitations were calculated and the differential conductance in the nonlinear regime was obtained. In the opposite limit, Braggio *et al.* [71] considered the possibility of fast relaxation of plasmons induced by extra processes [69] that are not included in the diagonal Hamiltonian of a free LL inside a quantum dot, such as phonon coupling. More recently, the same approach was applied to the case of a 1D quantum dot with spin [66]. The latter approach is equivalent to the one described in this thesis, Sec. 3.3.2, although the tunneling rates were derived with path integral techniques in a system where a *single* LL was pierced by two impurities, thus not allowing to have different interaction constants for the leads and the quantum dot. As Kim *et al* have pointed out [18], the "non-relaxed" and "fully relaxed" approximations do not give qualitatively different results regarding the current-voltage characteristic of the system. However, in a very recent work [72], the presence of stable plasmons in a spinless 1D quantum dot has been shown to affect dramatically its shot noise properties. These results are commented in somewhat more details in section 5.3.3. In the same system, a crossover towards the results of a model with fully relaxed bosonic modes [73], was predicted in the presence of a phenomenological relaxation rate for the plasmons. The two models give the same results if $\gamma_P / \tilde{\Gamma}_0 \gtrsim 1$, where γ_P is a phenomenological relaxation rate of the plasmonic modes and $\tilde{\Gamma}_0^{-1} = \Gamma_0^{(L)^{-1}} + \Gamma_0^{(R)^{-1}}$ (for $g_\rho = g_\sigma = 1$) is a characteristic tunneling rate. In a system with spin, we can expect similar results. For the fully relaxed system to be well established, therefore, one must have $\gamma_{\rho,\sigma} / \tilde{\Gamma}_0 \gtrsim 1$, where now $\gamma_{\rho,\sigma}$ represent the phenomenological relaxation rates of collective charge and spin modes. The relation for γ_σ seems somewhat more difficult to be fulfilled. For semiconductor-based 1D quantum dots[8] one can estimate $\tilde{\Gamma}_0 \approx 10^{11} \, \mathrm{s}^{-1}$ by using a tunnel resistance $R_R \approx 100 \, h/e^2$ and $a \approx 0.2 \, \mu\mathrm{m}$. It is difficult to evaluate microscopically the relaxation rates $\gamma_{\rho,\sigma}$. However, one can estimate [69], using a level spacing of about 1 meV, $\gamma_\sigma \approx 8 \cdot 10^{12} \, s^{-1}$. It can be expected that γ_ρ is even larger. In the rest of the thesis we assume $\gamma_{\rho,\sigma} / \tilde{\Gamma}_0 > 1$ and thus complete relaxation of the bosonic modes.

3.3.3 Spin-flip processes

In analogy with the relaxation of the collective modes described in detail in the last section, we want to consider the possibility of having relaxed "spin-

polarized" excited state (with total spin higher than the ground state), i.e. we want to allow spin-flip transitions inside the quantum dot. As will become clear in the following chapter, the spin-polarized states play a crucial role in the nonlinear transport properties of the quantum dot. Therefore, the spin-flip relaxation is an important tool to characterize the effects induced by these states. We introduce the phenomenological relaxation rate

$$\Gamma^w_{|n,s\rangle \to |n,s'\rangle} = w \left[\delta_{s',s-2} + e^{-\beta E_\sigma(s'^2-s^2)/2} \delta_{s',s+2} \right] \tag{3.41}$$

where w is the effective (phenomenological) spin-flip rate. The master equation

$$\sum_{n'} \sum_{s'=s\pm 1} P_{n',s'} \Gamma_{|n',s'\rangle \to |n,s\rangle} = P_{n,s} \sum_{n'} \sum_{s'=s\pm 1} \Gamma_{|n,s\rangle \to |n',s'\rangle} \tag{3.42}$$

now becomes

$$\sum_{n'} \left[\sum_{s'=s\pm 1} P_{n',s'} \Gamma_{|n',s'\rangle \to |n,s\rangle} + \sum_{s'=s\pm 2} P_{n',s'} \Gamma^w_{|n',s'\rangle \to |n',s\rangle} \right] =$$
$$P_{n,s} \sum_{n'} \left[\sum_{s'=s\pm 1} \Gamma_{|n,s\rangle \to |n',s'\rangle} + \sum_{s'=s\pm 2} \Gamma^w_{|n,s\rangle \to |n,s'\rangle} \right], \tag{3.43}$$

with $n' = n, n+1$. In the following, we will study (3.43) in the nonlinear transport regime.

Transport properties

"The way out of a trap is to study the trap itself." (**B. H. Gunaratana**)

Solving the master equation introduced in chapter 3 with the underlying assumption of totally relaxed collective modes (section 3.3.2), the occupation probabilities for the dot states can be readily obtained. Using these probabilities, it is possible to calculate the stationary current and differential conductance of the system. In this chapter we will analyze both the linear (section 4.2) and the nonlinear (section 4.3) regimes. In the linear regime, the influence of the spin degree of freedom and the interacting leads is analyzed. In the nonlinear regime, we show that spin-charge separation and an asymmetric barriers setup cooperate to trap excited states with total spin higher than the ground state. This, in turns, gives rise to negative differential conductance [17, 19]. The effects of spin-flip relaxation processes and leads interactions on the latter effect are discussed.

4.1 General considerations

In order to deal with transport properties, we must evaluate the current through the quantum dot. To accomplish this task, we first have to solve the master equation (3.43)

$$\sum_{n'} \left[\sum_{s'=s\pm1} P_{n',s'} \Gamma_{|n',s'\rangle \to |n,s\rangle} + \sum_{s'=s\pm2} P_{n',s'} \Gamma^{w}_{|n',s'\rangle \to |n',s\rangle} \right] =$$

$$P_{n,s} \sum_{n'} \left[\sum_{s'=s\pm1} \Gamma_{|n,s\rangle \to |n',s'\rangle} + \sum_{s'=s\pm2} \Gamma^{w}_{|n,s\rangle \to |n,s'\rangle} \right] ,$$

with $n' = n, n+1$. According to the applied source-drain voltage V, to the gate voltage V_g and the temperature $k_B T$, the set $\mathcal{T}$ of relevant states on which (3.43) has to be solved must be considered. Since we have assumed E_ρ to be

the highest energy scale in the dot (see. section 3.2), depending on V and V_{g} at most the two charge states n and $n + 1$ can play a role in the transport properties of the dot. This, however, does not rule out the possibility of populating excited states with high spin: assuming n, the transitions sequence

$$|n, 0\rangle \xrightarrow{\text{In},\pm} |n + 1, \pm 1\rangle \xrightarrow{\text{Out},\mp} |n, \pm 2\rangle$$

is for instance perfectly plausible at high enough V and, as will become clear in section 4.3, plays a determinant role in creating negative differential conductance in the presence of spin-charge separation. It is useful to notice that, because of the constraint $n + s =$ even, it is sufficient to denote the spin s of a state in order to determine also the corresponding charge state n or $n + 1$. Therefore, in the following we will adopt a much lighter notation where only the *spin* of the states will be denoted, unless otherwise required for clarity. In general the master equation is solved numerically and the set $\mathcal{T}$ is determined by means of an iterative procedure which determines also the stability of the solution itself. This allows to explore with great flexibility a wide range of external parameters. Under suitable approximations, analytically manageable solutions can be found. For instance, assume n even and a very low temperature $k_{\mathrm{B}}T \ll E_\sigma$. The set of relevant states, determined by the applied voltage V, is $\mathcal{T} = \{-\bar{s}(V), -\bar{s}(V) + 1, \ldots, 0, \ldots, \bar{s}(V) - 1, \bar{s}(V)\}$ where $\bar{s}(V)$ (which will be denotes $\bar{s}$ from now on) represents the maximum spin of the allowed excites states in the dot. We disregard here spin-flip processes ($w = 0$). Unrolling the master equation, it is easy to check that the following recursive detailed balance relations hold

$$\begin{aligned}
P_0 \Gamma_{0 \to 1} &= P_1 \Gamma_{1 \to 0} \\
P_1 \Gamma_{1 \to 2} &= P_2 \Gamma_{2 \to 1} \\
&\cdots \\
P_{\bar{s}-1} \Gamma_{\bar{s}-1 \to \bar{s}} &= P_{\bar{s}} \Gamma_{\bar{s} \to \bar{s}-1}
\end{aligned}$$

where $\Gamma_{s \to s'} = \Gamma^{(\mathrm{L})}_{s \to s'} + \Gamma^{(\mathrm{R})}_{s \to s'}$ is the total transition rate. Since no magnetic field is present, $P_s \equiv P_{-s}$. Thus we can express all the probabilities up to a normalization constant ($|s| \geq 1$, $|s| \leq \bar{s}$)

$$P_s = P_0 \left(\prod_{q=0}^{s-1} \Gamma_{q \to q+1} \right) \Bigg/ \left(\prod_{q=0}^{s-1} \Gamma_{q+1 \to q} \right) \equiv P_0 \Upsilon_s . \tag{4.1}$$

Imposing the normalization condition, one finds

$$P_0 = \left(1 + 2 \sum_{q=1}^{\bar{s}} \Upsilon_q \right)^{-1} . \tag{4.2}$$

Therefore, for $|s| \geq 1$ we obtain

$$P_s = \left(1 + 2 \sum_{q=1}^{\bar{s}} \Upsilon_q \right)^{-1} \Upsilon_s . \tag{4.3}$$

The stationary current can be calculated on either the right or the left barrier. We choose the right one. The current reads

$$I = e \sum_{n,s} \sum_{q=\pm 1} P_{n,s} \left[\Gamma^{(R)}_{|n,s\rangle \to |n+1,s+q\rangle} - \Gamma^{(R)}_{|n,s\rangle \to |n-1,s+q\rangle} \right] \tag{4.4}$$

where, for ease of notation, we have re-inserted the charge index n.

4.2 Linear transport

4.2.1 Zero temperature

In the $V \to 0$ limit, the dot is in the linear transport regime. In this regime we assume symmetric tunneling barriers: $G_L = G_R$, $C_L = C_R$. In order to have transport in the linear regime at zero temperature, it is necessary to align the dot levels of two n and $n + 1$ electron ground states states. This condition is in general not satisfied, and the dot is said to be *Coulomb blockaded* in its ground state, unless a suitable tuning of the gate voltage V_g is performed (see section 1.4). Recalling the dot total energy in a particular state

$$\mathcal{U}(n, s, l_\rho, l_\sigma) = \frac{E_\rho}{2} (n - n_g)^2 + \frac{E_\sigma}{2} s^2 + l_\rho \varepsilon_\rho + l_\sigma \varepsilon_\sigma \tag{4.5}$$

we define the electrochemical potential of the quantum dot

$$\mu_d(n, s_n) = \mathcal{U}(n+1, s_{n+1}, 0, 0) - \mathcal{U}(n, s_n, 0, 0) \equiv E_\rho \left(n + \frac{1}{2} - n_g \right) + (-1)^n \frac{E_\sigma}{2} . \tag{4.6}$$

Here s_n, s_{n+1} represent the spin of the ground states for n and $n + 1$ electrons respectively. The resonance condition is achieved if $\mu_d(n, s_n) \equiv 0$. Solving for n_g we obtain the zero temperature position of the linear conductance peaks

$$\bar{n}_g^{(0)}(n) = n + \frac{1}{2} + (-1)^n \frac{E_\sigma}{2 E_\rho} . \tag{4.7}$$

As it is clear, the peaks exhibit an even-odd effect. Namely, the distance between two consecutive peaks $\delta(n \leftrightarrow n + 1)$ is given by

$$\delta(n \leftrightarrow n + 1) = 1 + (-1)^{n+1} \frac{E_\sigma}{E_\rho} .$$

The Coulomb blockade region is larger if the number of extra charges in the dot is *odd*, namely if the ground state is spin-degenerate. This even-odd effect, which has been observed in the linear transport of one-dimensional quantum dot created in metallic nanotubes [74,75], is analogous to the shell-filling effect occurring in quantum dots of higher dimensionalities [76]. In the zero-temperature peak, the resonance condition is fulfilled for a peculiar value of the gate voltage, therefore the theoretical shape of the linear conductance peaks is a delta function.

4.2.2 Low temperature

In the case of nonzero temperature, the resonance condition can be fulfilled within a precision of the order of $k_\mathrm{B}T$. Thus, the conductance peaks get broadened. In the low temperature limit, $k_\mathrm{B}T < E_\sigma$, one can disregard the thermal population of all the excited states and consider the ground states for n and $n+1$ electrons only. The linear conductance $\mathcal{G} = \partial I/\partial V$ is then given by

$$G(\xi(n)) = \frac{\beta e^2}{\sqrt{8}} \frac{\Gamma(-\xi(n))e^{-\beta\xi(n)/2}}{\cosh\{[\beta\xi(n)+(-1)^n\log(2)]/2\}} \tag{4.8}$$

with $\Gamma(x) \equiv \sum_\lambda \Gamma^{(\lambda)}(x)$ the sum of the left and right barriers tunneling rates (3.34). We have defined the energetic displacement with respect to the zero-temperature peak position $\xi(n) = E_\rho\left(n_\mathrm{g} - \bar{n}_\mathrm{g}^{(0)}(n)\right)$. Because of the factor $\log(2)$ in the denominator of (4.8), stemming from the spin degeneracy of one of the resonating ground states [77], the conductance peak is not necessarily centered around the zero-temperature position, i.e. $\xi(n) = 0$. Indeed, the peak position in the low temperature regime is given by

$$\bar{n}_\mathrm{g}(n;T) = \bar{n}_\mathrm{g}^{(0)}(n) + (-1)^{n+1}\Phi(g)\frac{k_\mathrm{B}T}{E_\rho} \tag{4.9}$$

and the slope prefactor $\Phi(g)$ is determined by the implicit solution of the equation

$$\mathrm{Im}\left[\psi\left(\frac{1}{2g} + i\frac{\Phi(g)}{2\pi}\right)\right] + \frac{\pi}{2}\tanh\left[\frac{\log(2)+\Phi(g)}{2}\right] \tag{4.10}$$

where $\psi(x)$ denotes the digamma function [62]. With noninteracting leads, one recovers the well known result $\Phi(1) = \log(2)/2$ [78], while for infinitely strong interactions we get $\Phi(0) = \log(2)$. The prefactor Φ is plotted in Fig. 4.1 as a function of g_0. Plugging (4.9) in (4.8), we find that the conductance maximum exhibits the non-universal power-law behavior

$$\mathcal{G}^{\mathrm{max}}(T) = \mathcal{G}_0\left(\frac{k_\mathrm{B}T}{E_\sigma}\right)^{1/g-2}. \tag{4.11}$$

Notice that, at low temperatures, the power law is determined by the interaction parameter of the leads only. A plot of the linear conductance peak at low temperature ($k_\mathrm{B}T = 0.07E_\sigma$) as a function of the energetic displacement $\xi(n)$ and the effective leads interaction parameter g, as in Fig. 4.2, shows the non-monotonic nonlinear behavior (4.11). Figure 4.3 shows four consecutive conductance peaks as a function of n_g. The detuning of the peaks increasing the temperature is evident.

4.2.3 High temperature

Increasing further the temperature, when $k_\mathrm{B}T \gtrsim E_\sigma$ expression (4.8) is no longer valid since the thermally activated population of excited states with $|s| > 1$ is no more negligible. In this case we resort to the numerical solution of the master equation, evaluating numerically the tunneling rates in order to fully take into account the dot spectral density contributions. The results
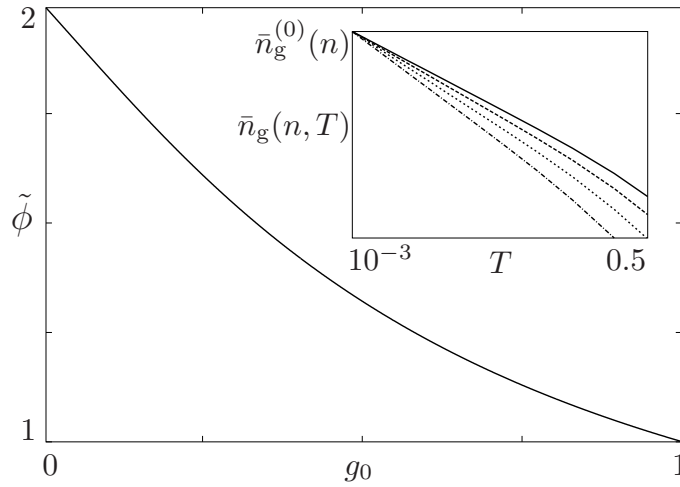
Figure 4.1: Plot of the normalized slope prefactor $\tilde{\Phi}(g_0) = 2\Phi(g_0)/\log(2)$ – see (4.9) – as a function of the leads interaction parameter g_0; Inset: Peak position $\bar{n}_{\mathrm{g}}(n;T)$ as a function of T (units E_σ/k_{B}) in the low temperature $k_{\mathrm{B}}T < E_\sigma$ for various values of g_0: $g_0 = 1$ (solid), $g_0 = 0.8$ (dashed), $g_0 = 0.6$ (dotted), $g_0 = 0.4$ (dash-dotted).
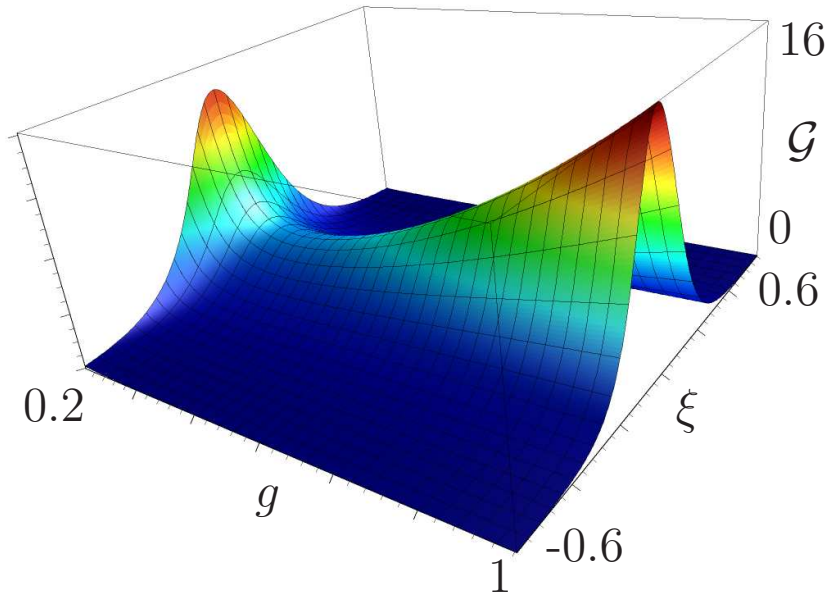
Figure 4.2: Linear conductance (4.8) for $k_{\mathrm{B}}T = 0.07E_\sigma$ in units $e^2\Gamma_0^{(\mathrm{R})}/E_\sigma$ for the transition $n \leftrightarrow n+1$ with n even. Here, $g_\rho = 0.3$ and $g_\sigma = 1$.

65
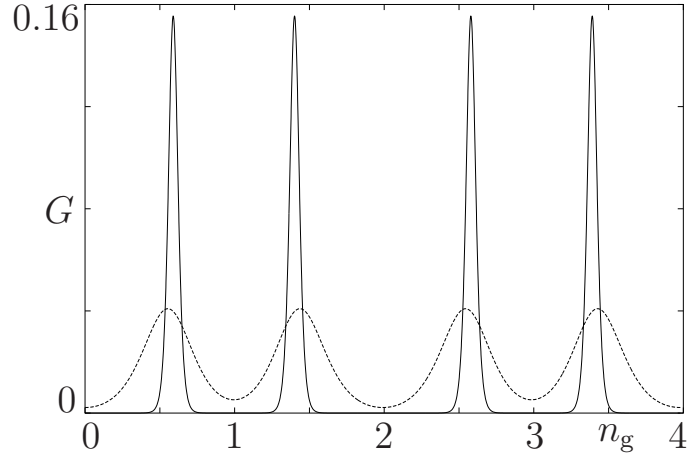
Figure 4.3: Linear conductance (units $e^2\Gamma_0^{(R)}/E_\sigma$) as a function of n_g for $E_\rho = 5E_\sigma$, $g_0 = 0.9$ and $g_\rho = 0.6$. Two different temperatures have been considered: $k_B T = 0.02 E_\sigma$ (solid curve) and $k_B T = 0.5 E_\sigma$ (dotted curve). The alternate movement of the conductance peaks increasing the temperature is clearly visible – see (4.9).
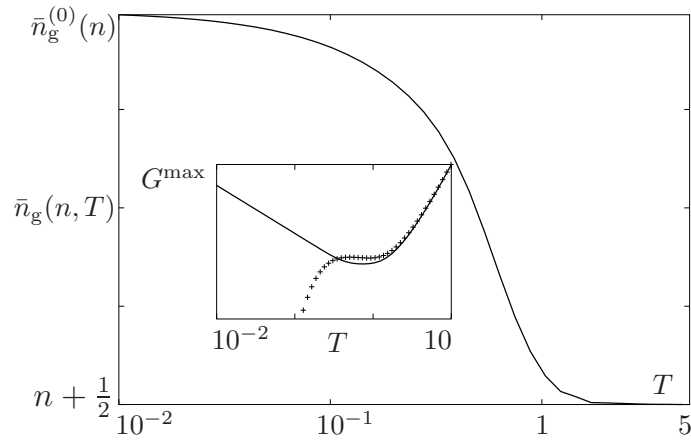
Figure 4.4: Position of the linear conductance peak for n even as a function of the temperature T (units E_σ/k_B for $g_0 = 0.8$, $g_\rho = 0.3$ and $g_\sigma = 1$ extrapolated by the numerical solution of the full master equation. Inset: (solid) double-logarithmic plot of the numerically extrapolated conductance maximum (arbitrary units) as a function of the temperature (units as in the main plot). (crosses) Conductance maximum as extracted by the analytical asymptotic expression (4.16).

are shown in Fig. 4.4. The main plot shows the peak position, extracted from the numerical solution for the conductance, as a function of the temperature T (units E_σ/k_B). For intermediate temperatures $k_B T \lesssim E_\sigma$ the peak position exhibits a deviation from the linear law (4.9) and approaches, in the $k_B T > E_\sigma$ limit, the universal position $n_g = n + 1/2$. This high-temperature result is independent of whether n is even or odd. The inset of Fig. 4.4 (solid line) shows the temperature dependence of the linear conductance peak maximum $\mathcal{G}^{\text{max}}$ in double-logarithmic scale. The low-temperature regime follows the already discussed power law (4.11) while increasing the temperature a crossover to a new power law regime can be clearly observed. In the $k_B T \gg E_\sigma$ regime, it is possible to obtain an analytic expression for the linear conductance of the dot. We assume n even, the factorizability of $P_{n,s} = p(n)\Psi(s)$ and a thermal occupation probability for the spin states

$$\Psi(s) = \begin{cases} Z_e^{-1} e^{-\beta E_\sigma s^2/2} & s \text{ even} \\ Z_o^{-1} e^{-\beta E_\sigma (s^2-1)/2} & s \text{ odd} \end{cases} \tag{4.12}$$

with $Z_e = Z_o = \sqrt{\pi/2\beta E_\sigma}$ as determined from the normalization condition. Summing over the spin states we obtain an effective master equation for $p(n)$

$$p(n)\bar{\Gamma}_{n\to n+1} = p(n+1)\bar{\Gamma}_{n+1\to n} \tag{4.13}$$

where the effective rates are

$$\bar{\Gamma}_{n\to n+1} = \sum_{p=\pm 1} \int ds\, e^{-2\beta E_\sigma s^2} \Gamma_{2s\to 2s+p} \tag{4.14}$$

$$\bar{\Gamma}_{n+1\to n} = \sum_{p=\pm 1} \int ds\, e^{-2\beta E_\sigma (s^2+ps)} \Gamma_{2s+p\to 2s}. \tag{4.15}$$

As a final result, we obtain the approximate solution for the linear conductance

$$\mathcal{G}(\zeta) = \frac{\beta e^2}{2} \frac{\Gamma(\zeta + E_\sigma/2)\Gamma(-\zeta - E_\sigma/2)}{\Gamma(\zeta + E_\sigma/2) + \Gamma(-\zeta - E_\sigma/2)} \tag{4.16}$$

where $\zeta = E_\rho(n - n_g + 1/2)$. For $k_B T \gg E_\sigma$, (4.16) has a maximum around $\zeta = 0$, thus the universal value $\xi = 0$ discussed above. In the same regime, the peak maximum exhibits a power law behavior

$$G^{\text{max}}(T) \propto \begin{cases} T^{1/g+(2g_\sigma)^{-1}-2} & \varepsilon_\sigma \ll k_B T < \varepsilon_\rho \\ T^{1/g+(2g_\sigma)^{-1}+(2g_\rho)^{-1}-2} & \varepsilon_\rho \ll k_B T < E_\rho \end{cases}$$

whose exponent depends also on the interactions parameters in the dot. In Fig. 4.4 the high-temperature power law in the regime $\varepsilon_\sigma < k_B T < \varepsilon_\rho$ is clearly visible. In this parameters region, only the spin density wave excitations contribute to the power law. The asymptotic formula (4.16) is plotted as crossed dots: it is clear that the matching with the numerical data is very good at high temperature.

4.3   Nonlinear transport

4.3.1   Negative differential conductance

Turning to the nonlinear transport ($|V| > 0$) regime, the solution of the master equation and, most important, the evaluation of the current and differential conductance, become extremely involved because of the increasing number of excited states involved in the transport dynamics. In the most general case, we resort to a numerical evaluation of the latter quantities. In the following we will disregard the effect of spin-flip relaxation processes. Their influence will be addressed in section 4.3.5. In Fig. 4.5 (left) we show the results of this
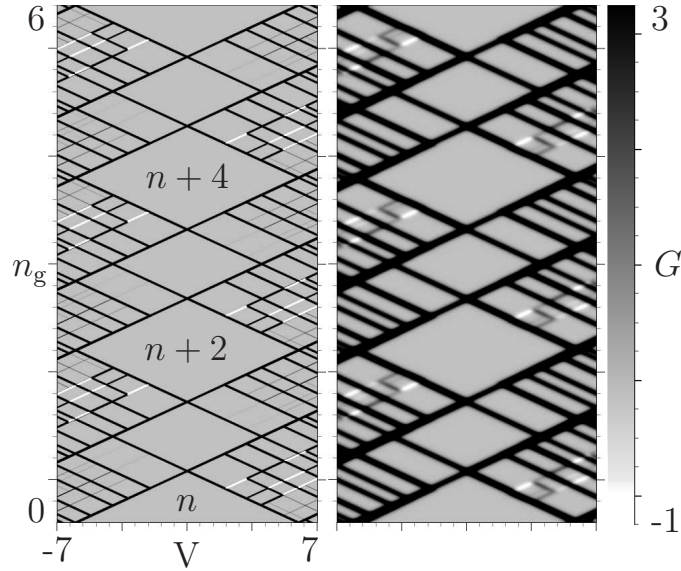
Figure 4.5: Grayscale plot of the numerically evaluated differential conductance G (arbitrary units) as a function of the source-drain voltage V (units E_σ/e) and n_g for n even. Here, $E_\rho = 5E_\sigma$, $g_0 = 1$, $g_\rho = 0.63$, asymmetry $A = G_L/G_R = 100$ and $C_L = C_R$. Left panel: $k_B T = 7.5 \times 10^{-3} E_\sigma$. Right panel: $k_B T = 7.5 \times 10^{-2} E_\sigma$.

calculation in low and intermediate temperature regimes, for an interacting quantum dot with noninteracting leads and asymmetric tunneling barriers, as a grayscale plot. To fix notations, we define the *asymmetry A* of the dot barriers as $A = G_L/G_R$. The plot shows several features which are clearly detectable. Black (white) lines represent positive (negative) differential conductance peaks. In the diamond-shaped zones which develop around $V = 0$, the dot is in the *Coulomb blockade* regime: in the sequential regime the transport here is only thermally activated and the current is exponentially suppressed. The vertexes of the Coulomb diamonds at $V = 0$ correspond to the linear conductance peaks discussed in section 4.2. In the $|V| > 0$ regime, regions of increasing complexity are found, with many intersecting lines denoting differential conductance peaks due to transport involving excited dot states. Most interesting, *negative differential conductance* (NDC) peaks (white lines) can be de-

tected. This behavior will be analyzed in details in the next sections. Looking at the right panel of Fig. 4.5, it is clear that increasing the temperature washes out the fine structure of peaks present at low temperature. However, the most prominent features, such as the negative differential conductance, still survive. In the following we will concentrate mainly on the low ($k_{\rm B}T \ll E_\sigma$) temperature regime. In Fig. 4.6, the differential conductance in the $(V, n_{\rm g})$ plane for
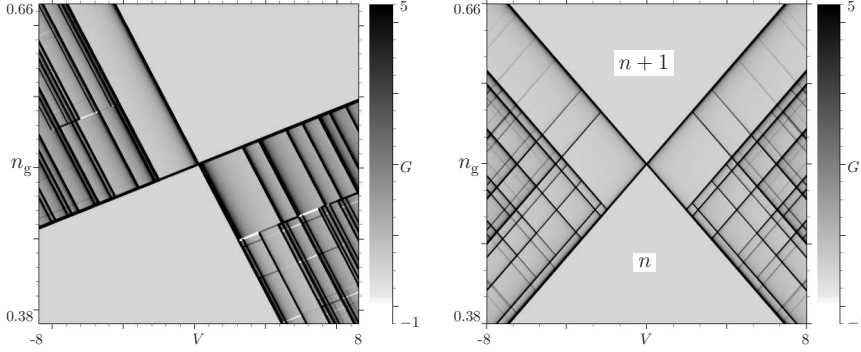
Figure 4.6: Grayscale plots of the differential conductance G (arbitrary units) as a function of V (units E_σ/e) and $n_{\rm g}$ for $n = 0$, $k_{\rm B}T = 10^{-2}E_\sigma$, $E_\rho = 25E_\sigma$, $g_0 = 0.9$, $g_\rho = 0.8$ and $g_\sigma = 1.1$. (Left) Asymmetric tunneling barriers, $A = G_{\rm L}/G_{\rm R} = 50$ and $C_{\rm L}/C_{\rm R} = 5$ with $C_{\rm g}/C_{\rm R} = 0.01$, corresponding to $\eta \approx 0.17$; (Right) Symmetric tunneling barriers $A = 1$, $\eta = 1/2$.

$n = 0$ is shown for an *interacting* quantum dot with slightly interacting leads. For an asymmetric barriers setup, as can be clearly seen in the left part of the figure, many NDC peaks are present in the nonlinear conductance spectrum. However, for an interacting dot with *symmetric* barriers, no NDC features can be detected whatsoever.

Recalling the polarization scheme of the dot, for $V > 0$ electrons flow through the dot from the right lead to left one. Therefore, if $A = G_{\rm L}/G_{\rm R} > 1$, the states $|n, s\rangle$ will have a higher occupation probability in comparison with states $|n+1, s'\rangle$. This creates an effective "trapping" phenomenon which, for sufficiently high barriers asymmetry, can create a bottleneck for the electron transport. As an example, the occupation probabilities for the two ground states for $n = 0$ and $n = 1$, and for the first excited states with $|s| = 2$, are represented in Fig. 4.7 in the case of an interacting dot with $A = 50$. For increasing voltage V, it is clear that the current suddenly drops (around $V = 2.5$) when the occupation probability of the excited states exceeds that of the ground state $s = 0$. Notice that the occupation probability of the states with $|s| = 1$ is, in any case, negligible because $A \gg 1$. For negative voltages $V < 0$, keeping $A > 1$, electrons travel through the dot from the left to the right lead, therefore the role of states with n and $n + 1$ excess electrons is reversed. In the $V < 0$ case of Fig. 4.6 (left panel), where $n = 0$, the first excited states which possibly get trapped are those with $|s| = 3$, thus the NDC can be expected on the $2 \to 3$ transition line. Inspecting the scheme in Fig. 4.9, it is easy to check that for $A = 50$, this is exactly the case. Reversing the asymmetry, i.e. considering the case $0 < A < 1$ (while still keeping $G_{\rm R}$ fixed), for $V > 0$ ($V < 0$) states with
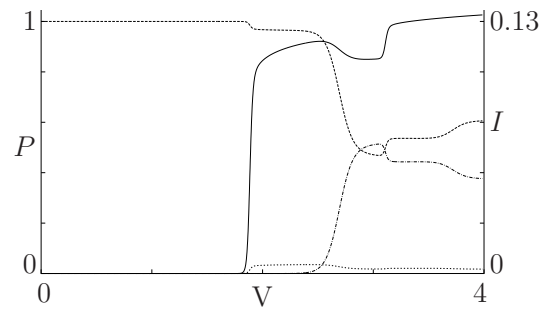
Figure 4.7: Occupation probabilities P_0 (dashed), $P_1 + P_{-1}$ (dotted), $P_2 + P_{-2}$ (dash-dotted) and current I (units $e\Gamma_0^{(R)}$) for an interacting dot with asymmetric barriers and $n = 0$ (parameters as in Fig. 4.6), at $n_g = 0.457$.

$n + 1$ (n) electrons get trapped. In summary, it is possible to expect a trapping of excited states with n extra electrons if $(A - 1)V > 0$, and a trapping of states with $n + 1$ extra electrons if $(A - 1)V < 0$.

Trapping phenomena, however, are not sufficient to induce NDC. In a *non-*
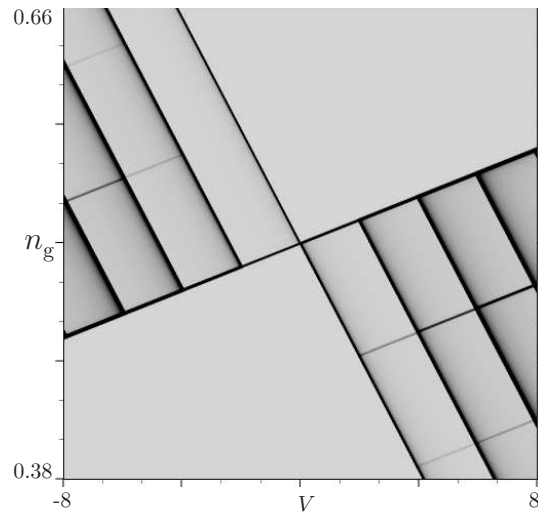
Figure 4.8: Differential conductance G (arbitrary units) as a function of V (units E_σ/e) and n_g for a noninteracting dot with asymmetric barriers ($A = 50$). Other parameters as in Fig. 4.6.

interacting dot, where no traces of spin-charge separation are present, no NDC signatures are found whatsoever – regardless of the strength of the asymmetry. This behavior is confirmed by Fig. 4.8. The interplay between trapping and interactions will be examined in detail in section 4.3.4.

4.3.2   Spectroscopy of excited states

In order to analyze in detail the features of the quantum dot conductance in the nonlinear regime, we must analyze spectroscopically the conductance peaks position in the (V, n_g) plane. In the following we will consider the $T = 0$ case, which is a very good approximation in the low temperature regime. First of all, we concentrate on the excitations involving states with high spin only. The discussion of CDW and SDW traces will be done in the last part of this section. The condition for the transition $|n, s\rangle \leftrightarrow |n + 1, s \pm 1\rangle$ to contribute the current is that the state $|n, s\rangle$ is occupied and that the generalized electrochemical potential $\tilde{\mu}_d(n, s, \pm 1) = \mathcal{U}(n + 1, s \pm 1, 0, 0) - \mathcal{U}(n, s, 0, 0)$

$$\tilde{\mu}_d(n, s, \pm 1) = -\xi(n) + E_\sigma \left[\chi(n) \pm s \right] , \tag{4.17}$$

with $\chi(n) = [1 - (-1)^n]/2$, falls inside the window defined by the electrochemical potentials of the left and right leads $\mu_{L,R}$:

$$\mu_L(V) = -\eta eV \leq \tilde{\mu}_d(n, s, \pm 1) \leq (1 - \eta)eV = \mu_R(V) \tag{4.18}$$

where we have defined the capacitances ratio $0 < \eta < 1$

$$\eta = \frac{C_R + C_g/2}{C_L + C_R + C_g} . \tag{4.19}$$

The transitions between ground states correspond to the lines on the (V, n_g)
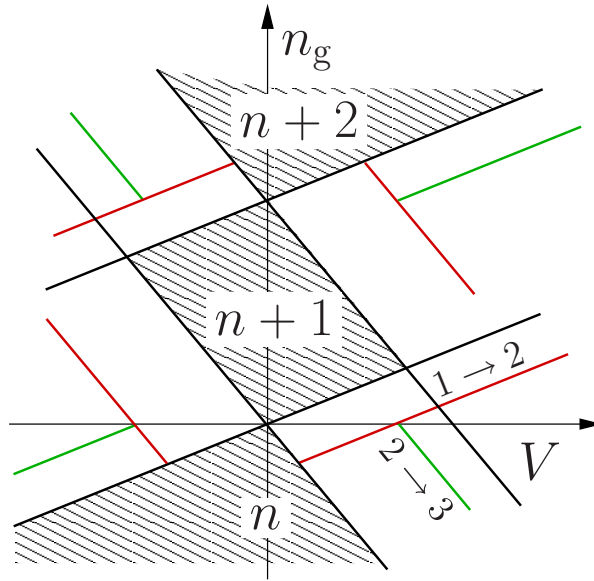
Figure 4.9: Spectroscopic position of the conductance peaks in the (V, n_g) plane for n even and a comparatively small value of E_ρ/E_σ. The red (green) line corresponds to the transition $1 \to 2$ ($2 \to 3$). CDW and SDW traces have been omitted for clarity.

plane

$$n_{\mathrm{g}}^{(+)}(n) = \bar{n}_{\mathrm{g}}^{(0)}(n) + \eta\frac{eV}{E_\rho} \qquad n_{\mathrm{g}}^{(-)}(n) = \bar{n}_{\mathrm{g}}^{(0)}(n) + (\eta - 1)\frac{eV}{E_\rho}\,.$$

These lines partition the plane in regions where a given set of charge states $\{n_{\min}, \ldots, n_{\max}\}$ is involved in the transport. The regions where only one charge state is allowed are the *Coulomb blockade* regions. They are diamond-shaped if $\eta = 1/2$, as it has already been shown in Fig. 4.5, and become skewed as $\eta \neq 1/2$. In Fig. 4.9 the Coulomb diamonds are represented by the hatched regions and the g.s. to g.s. transitions by the black lines. Inside the non-hatched regions, the two ground states are populated and conduction is possible through the dot, therefore excited states of n and $n+1$ electrons can be populated for high enough V. Denoting from now on the transitions with the relevant spins only, and recalling the degeneracy of the s and $-s$ spin states in the dot, the first transitions involving excited states are $s = 1 \leftrightarrow 2$. The position of the corresponding transition lines is obtained considering the extremal solutions of (4.18) with $s = 2$ (n even) or $s = 1$ (n odd). For even n, the solutions are

$$n_{\mathrm{g}} = \bar{n}_{\mathrm{g}}^{(0)}(n) - 2E_\sigma/E_\rho + \eta eV/E_\rho \qquad s : 1 \to 2$$

$$n_{\mathrm{g}} = \bar{n}_{\mathrm{g}}^{(0)}(n) - 2E_\sigma/E_\rho + (\eta - 1)eV/E_\rho \qquad s : 2 \to 1$$

for $V > 0$, while for $V < 0$ we have

$$n_{\mathrm{g}} = \bar{n}_{\mathrm{g}}^{(0)}(n) + 2E_\sigma/E_\rho + (\eta - 1)eV/E_\rho \qquad s : 1 \to 2$$

$$n_{\mathrm{g}} = \bar{n}_{\mathrm{g}}^{(0)}(n) + 2E_\sigma/E_\rho + \eta eV/E_\rho \qquad s : 2 \to 1\,.$$

They are schematically depicted as red lines in Fig. 4.9. These lines cut the plane into two regions, one of which has the states with $s = \pm 2$ occupied. Inside this latter region it is possible to have the transition $s = 2 \to 3$, which is represented by the green line in Fig. 4.9. Following this procedure, a "fishbone"-like structure of interleaved transition lines is generated in the (V, n_{g}) plane. This structure is sketched in Fig. 4.9. Along with "high" spin excited states, neutral CDWs and SDWs can be excited in the transport. For instance, considering all the possible combinations of CDWs and SDWs occurring in the transitions $s : 0 \leftrightarrow 1$ gives rise to the families of lines (we quote here only the $V > 0$ expressions)

$$n_{\mathrm{g}} = \bar{n}_{\mathrm{g}}^{(0)}(n) + (\eta - 1)eV/E_\rho + l_\rho\varepsilon_\rho + l_\sigma\varepsilon_\sigma \qquad s : 0 \to 1$$

$$n_{\mathrm{g}} = \bar{n}_{\mathrm{g}}^{(0)}(n) + \eta eV/E_\rho + l_\rho\varepsilon_\rho + l_\sigma\varepsilon_\sigma \qquad s : 1 \to 0$$

with $l_\nu \in \mathbf{N}$. Similarly, every transition $s \to s'$ can occur through the excitation of collective modes. This gives rise to the intricate structure which can be clearly seen in Fig. 4.5. In the following of the chapter, we will concentrate mainly on the specific region of the (V, n_{g}) plane depicted in Fig. 4.10. The dashed lines in Fig. 4.10 represent the transition $1 \to 0$ involving respectively one SDW (light gray) or one CDW (dark gray). The solid gray lines represent the same excitations occurring in the transition $2 \to 1$. It is important to point
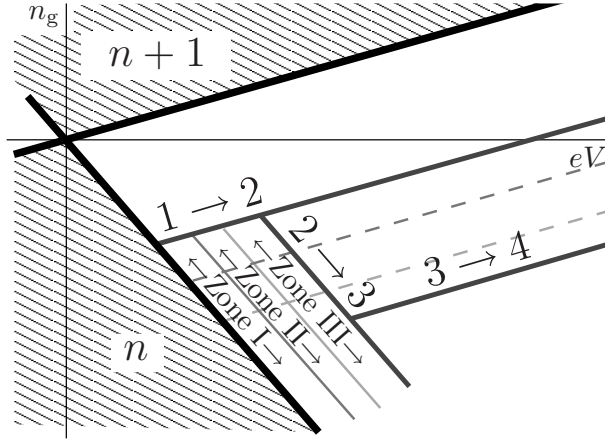
Figure 4.10: Scheme of the transition lines for n even, $V > 0$ and $E_\rho/E_\sigma \gg 1$ in the "5 states region", for an interacting quantum dot with $g_\rho < 1$ and $g_\sigma > 1$.

out that, to the right of the line $1 \to 2$, the state $s = 2$ has a nonzero occupation probability, so that the transitions $2 \to 1$, involving a collective excitation, are detectable as conductance peaks. The width of the zone *I* is proportional to $\varepsilon_\sigma - 2E_\sigma$ and that of zone *II* is proportional to $\varepsilon_\rho - \varepsilon_\sigma$. In the noninteracting limit $g_\nu \to 1$ both the zones shrink down and the rate for the transition $2 \to 1$ exhibits a unitary jump as already discussed in section 3.3.2. In the same fashion, the two dashed lines collapse ontop of the $1 \to 2$ transition line. Zones *I*, *II* and *III* define a "5 states region" since dot states with up to $|s| = 2$ are occupied here.

4.3.3   Noninteracting dot

Before analyzing in more detail the NDC phenomenon occurring in the presence of spin-charge separation, we want to show that without interactions no NDC can develop. We assume to deal with a noninteracting dot with noninteracting leads ($g_0 = 1$), at zero temperature. Since, as it will be shown in the following, interactions in the leads tend to *suppress* the NDC features, the hypothesis $g_0 = 1$ is not restrictive. Moreover, the qualitative picture remains true also in the $T > 0$ case. Referring to Fig. 4.11, several transition lines are shown. In the absence of spin-charge separation, the transition rates exhibit unitary jumps and show peculiar patterns in the (V, n_g) plane. For instance, choosing $\Gamma_0^{(R)}$ as the rates unit, in the zones $\{A_m\}$ we have $\Gamma_{0\to1}^{(R)} = m$ and $\Gamma_{1\to0}^{(L)} = A$ while in the zones $\{B_m\}$ we have $\Gamma_{0\to1}^{(R)} = 1$, $\Gamma_{1\to0}^{(L)} = (m+1)A$, $\Gamma_{1\to2}^{(L)} = mA$ and $\Gamma_{2\to1}^{(R)} = 2$. With a bit of bookkeeping, it is possible to solve analytically the master equation in all the regions $\{A_m\}$, $\{B_m\}$, ... and evaluate the current I in the limit $A \to \infty$, obtained keeping G_R finite. In the $V > 0$ case, the limit described above is the most favorable in order to obtain NDC. The calculated current is shown in Fig. 4.11: the conductance lines parallel to the transition $1 \to 0$ are asymptotically vanishing for $A \to \infty$, while the lines parallel to $0 \to 1$ show
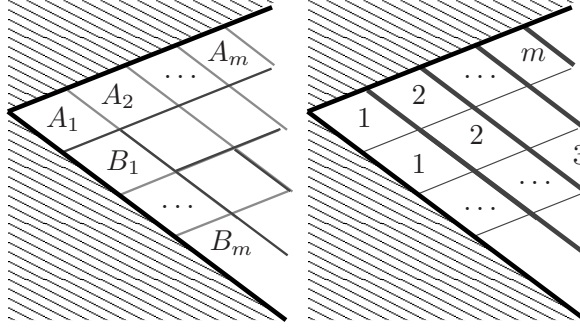
Figure 4.11: Scheme of the transition lines (left panel) and values of the current I in units $e\Gamma_0^{(R)}$ (right panel), for the case of a noninteracting dot with noninteracting leads in the $A \to \infty$ limit (obtained keeping G_R finite), at $T = 0$.

positive differential conductance. This situation is confirmed by the numerical calculation for $A = 50$ (see Fig. 4.8), which already shows a pattern of vanishing lines parallel to the transition $1 \to 0$, and strong positive peaks parallel to the $0 \to 1$ transition. Numerical analysis confirms that these results remain valid increasing the temperature and considering interacting leads.

4.3.4   Five states model

In order to analyze in detail the role of trapping and spin-charge separation in the development of NDC peaks, we will consider the analytically solvable regime where only the states with $|s| \leq 2$ contribute the current for an *even* number of extra electrons n. In the $(V > 0, n_g)$ semiplane, this corresponds to two regions: the stripe bounded by the $1 \to 0$, g.s. to g.s. transition line (bold black line in Fig. 4.10) and the transition line $1 \to 2$, where only the states with $|s| \leq 1$ contribute ("3 states regime"), and the the stripe formed by the zones labeled *I*, *II*, and *III*, where also the states with $|s| = 2$ are involved ("5 states regime"). Within these zones, it is possible to solve analytically the master equation and get an analytical expression for the current I. Assuming no spin-flip relaxation, we obtain

$$I = e \frac{2\Gamma_{0\to1}^{(R)} \left[\Gamma_{1\to0}^{(L)} + \Gamma_{1\to2}^{(L)}\right] \Gamma_{2\to1}^{(R)}}{\Gamma_{1\to0}^{(L)}\Gamma_{2\to1}^{(R)} + 2\Gamma_{0\to1}^{(R)}\left[\Gamma_{2\to1}^{(R)} + \Gamma_{1\to2}^{(L)}\right]} . \tag{4.20}$$

In the 3 states regime, this expression reduces to

$$I_3 = e \frac{2\Gamma_{0\to1}^{(R)}\Gamma_{1\to0}^{(L)}}{2\Gamma_{0\to1}^{(R)} + \Gamma_{1\to0}^{(L)}} .$$

In the most interesting 5 states regime, from (4.20) we can obtain approximated expressions for the differential conductance G. We are mainly interested in the NDC features, which occur in lines parallel to the transitions $1 \to 0$ and $1 \to 2$ (see Figs. 4.6,4.10), therefore we consider only the conductance along these

lines. Moreover, performing the current derivatives, we assume to be away from the crossing of two conductance lines. We get

$$G_p = \frac{e\phi_0}{\mathcal{D}_0^2} \sum_{p=\pm1} \Lambda_p \partial_V \Gamma^{(\text{L})}_{1\to1+p}(V) \tag{4.21}$$

where $\Gamma^{(\text{L})}_{1\to1+p}(V) \equiv \Gamma^{(\text{L})}(\Delta U_{1\to1+p})$ with

$$\Delta U_{1\to0} = E_\rho \left[n_\text{g} - \bar{n}_\text{g}^{(0)}\right] - \eta eV + l_\rho \varepsilon_\rho + l_\sigma \varepsilon_\sigma$$

and $\Delta U_{1\to2} = \Delta U_{1\to0} + 2E_\sigma$. We have defined $\phi_0 = 2\Gamma^{(\text{R})}_{0\to1}\Gamma^{(\text{R})}_{2\to1}$ and

$$\begin{aligned}
\Lambda_p &= \phi_0 + p \left[\Gamma^{(\text{R})}_{2\to1} - 2\Gamma^{(\text{R})}_{0\to1}\right] \Gamma^{(\text{L})}_{1\to1-p} \\
\mathcal{D}_0 &= \Gamma^{(\text{L})}_{1\to0}\Gamma^{(\text{R})}_{2\to1} + 2\Gamma^{(\text{R})}_{0\to1} \left[\Gamma^{(\text{R})}_{2\to1} + \Gamma^{(\text{L})}_{1\to2}\right]
\end{aligned}$$

The derivative $\partial_V \Gamma^{(\text{L})}(V)$ is a positive function which, for $g_0 \approx 1$, exhibits a peak near the $V = 0$ point. Being the transition rates positive functions of the energy, the sign of the conductance is determined by the factor Λ_p. For the transitions $1 \to 2$ (thus $p = 1$), the condition to get NDC can be rephrased as

$$2\Gamma^{(\text{R})}_{0\to1}\Gamma^{(\text{R})}_{2\to1} < \Sigma\Gamma^{(\text{L})}_{1\to0} \tag{4.22}$$

while for the transitions $1 \to 0$ ($p = -1$) we must have

$$2\Gamma^{(\text{R})}_{0\to1}\Gamma^{(\text{R})}_{2\to1} < -\Sigma\Gamma^{(\text{L})}_{1\to2} \tag{4.23}$$

with

$$\Sigma = 2\Gamma^{(\text{R})}_{0\to1} - \Gamma^{(\text{R})}_{2\to1}.$$

It is critical to realize that the factor Σ determines the possibility to achieve NDC: (4.22) can be fulfilled only if $\Sigma > 0$, while (4.23) requires $\Sigma < 0$. In the case of weakly interacting leads, the value of Σ strongly depend on the particular zone under consideration. Assuming $g_0 = 1$ and an interacting dot one can show that, for reasonable values of g_ρ and g_σ, $\Sigma > 0$ in zones *I* and *II*, while $\Sigma < 0$ in zone *III*. In the case of a noninteracting dot, zones *I* and *II* vanish and the entire 5 states region coincides with the zone *III*. For $g_0 \approx 1$ and small temperature, $\Sigma \equiv 0$ bans the possibility of NDC on both the transition lines, regardless the intensity of the trapping induced, for instance, by the asymmetric tunneling barriers. Notice that, for an interacting dot, the NDC on lines $1 \to 2$ can only be observed in zones *I* and *II*, while on lines $1 \to 0$ can only be observed on zone *III*. It is clear that, once the condition on Σ is met, NDC can be obtained by suitably increasing the rates $\Gamma^{(\text{L})}_{1\to0,2}$. This can be achieved either by increasing the barriers asymmetry *A*, or by considering high enough *V* in order to open transitions which involve many collective dot modes. Either way, this means increasing the *escape* rate of the dot, enhancing the aforementioned trapping phenomenon which leads to a bottleneck effect in the transport. For the case of the transition $|n+1,1\rangle \to |n,2\rangle$ we obtain

$$\begin{aligned}
&A > 2 = A_\text{c}^{(1)} &&\text{Zone } I \\
&A > 2(2g_\sigma + 1)/(2g_\sigma - 1) = A_\text{c}^{(2)} &&\text{Zone } II
\end{aligned}$$

while for the transitions $|n+1,1\rangle \rightarrow |n,0,1,0\rangle$ and $|n+1,1\rangle \rightarrow |n,0,0,1\rangle$ we get

$$A > 2\frac{g_\rho + g_\sigma + 2g_\rho g_\sigma}{g_\rho + g_\sigma - 2g_\rho g_\sigma} = A_c^{(3)} \, .$$

We have defined here the critical asymmetries $A_c^{(1)} < A_c^{(2)} < A_c^{(3)}$. Peculiarly, for each transition line in each of the zones there is a critical asymmetry. For noninteracting leads, the $A_c^{(i)}$ given above get renormalized to lower values by the increasing number of CDWs and SDWs involved in $\Gamma_{1\rightarrow0,2}^{(L)}$. If the leads are weakly interacting, the critical asymmetry is a function of the voltage as well, thus along each transition line the critical asymmetry varies. In principle, for interacting leads, the NDC condition could be fulfilled only in one portion of a given zone.

4.3.5 Spin-flip relaxation

As we have seen in the previous section, the NDC can be related to the occupation of excited states with a spin higher than the corresponding ground state. It is interesting to study the interplay between the spin-flip relaxation processes and the trapping phenomenon involved in the NDC. We concentrate specifically on the 5 states region discussed in section 4.3.4. Solving the master equation (3.43) and calculating the differential conductance with the same approximation as in section 4.3.4 we finally get

$$G = \frac{e\phi_w}{\mathcal{D}_w^2} \sum_{p=\pm 1} \Lambda_p^{(w)} \partial_V \Gamma_{1\rightarrow 1+p}^{(L)}(V) \tag{4.24}$$

where

$$\phi_w = 2\Gamma_{0\rightarrow 1}^{(R)} \left[w + \Gamma_{2\rightarrow 1}^{(R)} \right] ,$$

$$\Lambda_p^{(w)} = \phi_w + p \left[\Gamma_{2\rightarrow 1}^{(R)} - 2\Gamma_{0\rightarrow 1}^{(R)} \right] \Gamma_{1\rightarrow 1-p}^{(L)}$$

and

$$\mathcal{D}_w = \Gamma_{1\rightarrow 0}^{(L)} \Gamma_{2\rightarrow 1}^{(R)} + 2\Gamma_{0\rightarrow 1}^{(R)} \left[\Gamma_{2\rightarrow 1}^{(R)} + \Gamma_{1\rightarrow 2}^{(L)} \right] + w \left[\Gamma_{1\rightarrow 0}^{(L)} + \Gamma_{1\rightarrow 2}^{(L)} + 2\Gamma_{0\rightarrow 1}^{(R)} \right] .$$

As discussed previously, the sign of the conductance is determined by $\Lambda_p^{(w)}$, which is now a function of both the asymmetry and the relaxation w. First off, without interactions one has $\Lambda_p^{(w)} > 0$. Let us concentrate now on the $1 \rightarrow 2$ transition where the condition $\Lambda_1^{(w)} \leq 0$ reduces, for $T = 0$, to ($2E_\sigma < V < \varepsilon_\sigma$)

$$\frac{w}{\Gamma_0^L} \leq \left(\frac{2E_\sigma}{\omega_C}\right)^\alpha \left[1 - \frac{1}{2}\left(\frac{eV}{eV - 2E_\sigma}\right)^\alpha - \frac{1}{A}\left(\frac{eV}{2E_\sigma}\right)^\alpha\right] \tag{4.25}$$

with $2\alpha = 1/g_0 - 1$ (we recall ω_C is a cutoff energy). When the equality holds, a critical value w_c for the relaxation rate as a function of the asymmetry (for fixed voltage V) is obtained. For $w > w_c$, one gets positive differential conductance (PDC), while for $w < w_c$ one gets NDC. Thus, the plot of $w_c(A)$ defines a sort of separatrix of the "phase diagram" for the NDC effect in the
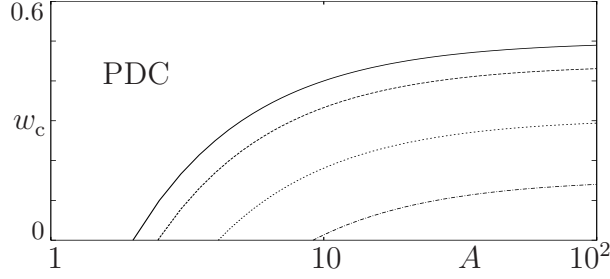
Figure 4.12: Phase diagram for the critical value of the spin-flip relaxation w (units $\Gamma_0^{(L)}(2E_\sigma/\omega_C)^\alpha$) inside zone I of the 5 states region at $T = 0$. Different interaction parameters for the leads have been considered: $g_0 = 1$ (solid), $g_0 = 0.9$ (dashed), $g_0 = 0.75$ (dotted), and $g_0 = 0.65$ (dash-dotted).

plane (w, A). Such a diagram is shown in Fig. 4.12 for different interaction parameters of the leads. The intersections of the separatrices at $w_c = 0$ give the critical asymmetry A_c in zone I as discussed in section 4.3.4. Interactions in the leads increase the critical asymmetry as can be clearly seen. For nonzero relaxation w, the critical asymmetry increases as well. The combined effect of relaxation and leads interactions reduces greatly the parameters region where NDC can be realized. The effect of spin flip relaxation is particularly clear in Fig. 4.13. The NDC peak around $V = 2.25$ is greatly affected by the spin-flip relaxation: a crossover from NDC to PDC is evident. For the parameters in Fig. 4.13, $w_c \approx 0.33$ in units $\Gamma_0^{(L)}(2E_\sigma/\omega_C)^\alpha$. Quite generally, all the conductance peaks with transitions involving states with $|s| = 2$ get depressed, while the other peaks are almost unaffected. It can be expected that in the asymptotically relaxed regime

$$\frac{w}{\Gamma_0^{(L)}} \gg A$$

all the conductance peaks should be positive. Indeed, in this regime one finds

$$G = e\left[\frac{2\Gamma_{0\rightarrow 1}^{(R)}}{\Gamma_{1\rightarrow 0}^{(L)} + \Gamma_{1\rightarrow 2}^{(L)} + 2\Gamma_{0\rightarrow 1}^{(R)}}\right]^2 \sum_{p=\pm 1} \partial_V \Gamma_{1\rightarrow 1+p}^{(L)}(V). \tag{4.26}$$

Comments on the observability of NDC

The NDC phenomenon described above could in principle be observed in transport experiments performed on CEO-based quantum dots [8] or CNTs [20]. The necessary condition to be fulfilled in order to apply the model and to resolve collective excitations signatures is

$$k_B T \ll \varepsilon_0 \ll E_F$$

which can be rephrased as

$$\lambda_T \gg a \gg \lambda_F$$

where $\lambda_T = \pi v_F/k_B T$ is the thermal length and $\lambda_F = 2\pi/k_F$ is the Fermi wavelength. In CEO-based quantum dots, the Fermi energy appears to be relatively
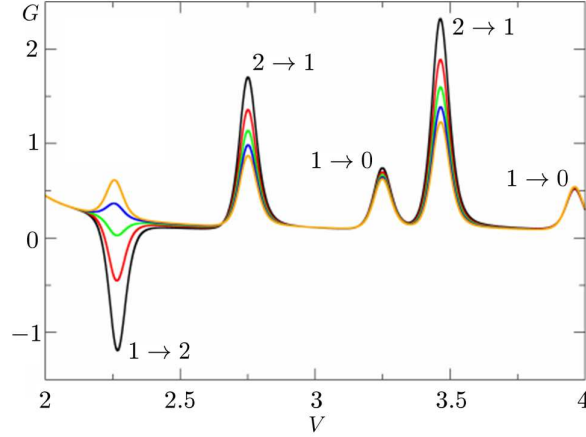
Figure 4.13: Differential conductance G (units $e^2 \Gamma_0^{(R)}/E_\sigma$) as a function of V (units E_σ/e) inside the five states region, for $n_g = 0.485$ and various spin-relaxation rate values (units $\Gamma_0^{(L)}(2E_\sigma/\omega_C)^\alpha$): $w = 0.2$ (black), $w = 0.3$ (red), $w = 0.4$ (green), $w = 0.5$ (blue) and $w = 0.6$ (yellow). The peaks are classified according to the spins involved in the transitions involved. Other parameters are $k_B T = 10^{-2} E_\sigma$, $E_\rho = 25 E_\sigma$, $A = 10$, $\eta = 1/2$, $g_0 = 0.9$, $g_\rho = 0.7$ and $g_\sigma = 1.25$.

low, $E_F \approx 2$ meV, due to the almost complete depletion of the lowest sub-band [79]. A dot level spacing of about 1 meV can be estimated for a quantum dot of length $a \approx 0.2$ μm, with an effective electron mass $m^* \approx 0.07 m_e$ (GaAs). At a first glance, these parameters seem to be outside the above region of validity of the model, although the temperature condition is easily achieved. For a quantum dot of larger size ($a \approx 1$ μm) the situation would be much more favorable. However, because of the accidental nature of the dot inside the CEO channel, a fine tuning of its size does not seem easily achievable. Other semiconductor based quantum dot systems, such as those fabricated by scratching techniques [80], seem more promising. With this technique it could be possible to fabricate an appropriately scaled quantum dot inside a quantum wire. The optimal parameters to be achieved seem to be: a width of the wire of ≈ 50 nm in order to achieve a Fermi energy of a few meV, a distance between the tunnel barriers – implemented via metallic gates – of ≈ 1 μm giving rise to $\varepsilon_0 \approx 0.1$ meV. Experiments should be performed below 1 K. With this technique, the asymmetry of the tunneling barriers could be adjusted with precision.

Carbon nanotubes seem to be even more favorable systems concerning the energy scales, since it is possible to estimate $E_F \approx 2$ eV, $v_F \approx 8 \cdot 10^5$ m/s and a level spacing $\varepsilon_0 \approx 5$ meV [74,75], with temperatures $T \approx 0.1$K. However, in this case the model described above needs to be adjusted since this system is described by means of a four-branch LL [47].

Part III

Interactions and noise

Overview on noise

"All the while the world is turning to noise" (**P. Gabriel**)

In recent years, much attention has been devoted to the statistical analysis of the current fluctuations in mesoscopic system. Initially this study has been confined to the second moment in the current fluctuations distribution, which goes under the name of *noise* [12, 13, 81]. Probably the most paradigmatic example of the effectiveness of the noise as an investigation tool is the direct observation of fractional quasiparticle charges in the fractional quantum hall effect [82]. In this chapter, a quick overview of the properties of noise in electronic systems will be given.

5.1 Generalities

Current fluctuations occur ubiquitously in electron systems. The most important causes of this behavior are the thermal excitation, the fermionic statistics of the carriers and the repulsive interactions among them. The first systematic studies on the noise properties of electronic systems trace back to the 1918, with the seminal work of W. Schottky on vacuum tubes [83]. Schottky pointed out that in these systems two intrinsic sources of time-dependent fluctuations are present: the thermal noise due to the thermal agitation of electrons, and the shot noise due to their granular nature. The fluctuations of current around its average value $\langle I \rangle$

$$\delta I(t) = I(t) - \langle I \rangle$$

can be characterized by means of the correlation function

$$\langle \delta I(t + \tau) \delta I(\tau) \rangle .$$

For an ergodic system, the ensemble average $\langle \ldots \rangle$ can be replaced by a time average. Furthermore, if the average is taken over a time longer than the average correlation time, the correlation function is invariant for a time shift. The

noise spectral density $S(\omega)$, therefore, can be defined as the Fourier transform

$$S(\omega) = \int_{-\infty}^{\infty} dt \, e^{i\omega t} \langle \delta I(t) \delta I(0) \rangle . \tag{5.1}$$

The *thermal noise* [84, 85] S_{th} is an equilibrium property: by means of the fluctuation-dissipation theorem it can be related to the linear conductance $G = I/V$ ($V \to 0$) by the expression $S_{\text{th}} = 4k_{\text{B}}TG$, which is independent of the frequency up to $\omega \approx k_{\text{B}}T$. Being an equilibrium property, the thermal noise is not a very useful investigation tool, bringing essentially the same information as the linear conductance. When out-of-equilibrium regimes are considered, the noise strongly deviates from the thermal value and brings valuable informations about the mechanisms underlying the transport. For instance, in the case of saturated thermionic valves, the main source of current fluctuations is due to the stochastical emission of electrons from the hot cathode. This emission is essentially a classical, *uncorrelated Poisson process*. In this case, the noise is given by the celebrated Schottky formula

$$S_{\text{pois}} = 2e\langle I \rangle \tag{5.2}$$

where e is the charge of the electron and $\langle I \rangle$ the average current. In mesoscopic systems, usually the fluctuations of electrons are strongly correlated: in the stationary limit ($\omega \to 0$), the *Fano factor*

$$F = \frac{S(\omega = 0)}{2e\langle I \rangle} \tag{5.3}$$

is commonly used to express the deviations from the uncorrelated regime. In the following, we will discuss several examples of low-dimensional mesoscopic systems where peculiar signatures due to electrons statistics and interactions can be detected in the properties of current fluctuations.

5.2   The Hanbury-Brown and Twiss experiment

The statistics of the particles in a beam determines, to a great extent, its current fluctuations. Consider the three sources in Fig. 5.1, characterized by the same average number of emitted particles $\langle n \rangle$ and in statistical equilibrium. The source (a) is completely uncorrelated and follows the Poisson statistics: the variance of the emitted particles is given by $\langle (\Delta n)^2 \rangle \equiv \langle \Delta n \rangle^2$. The sources (b),(c) emit respectively bosonic and fermionic particles

$$\langle n \rangle_{\text{B,F}} = \frac{1}{e^{(E-\mu)/k_{\text{B}}T} \mp 1}$$

with variance $\langle (\Delta n)^2_{\text{B,F}} \rangle = \langle n \rangle_{\text{B,F}} \left(1 \pm \langle n \rangle_{\text{B,F}} \right)$. It is possible to define the Fano factor of the source as $F_{\text{src}} = \langle (\Delta n)^2_{\text{src}} \rangle / \langle n_{\text{src}} \rangle$: then,

$$F_{\text{src}} = \begin{cases} 1 + \langle n_{\text{B}} \rangle & \text{Bosonic source} \\ 1 & \text{Uncorrelated source} \\ 1 - \langle n_{\text{F}} \rangle & \text{Fermionic source} \end{cases}.$$
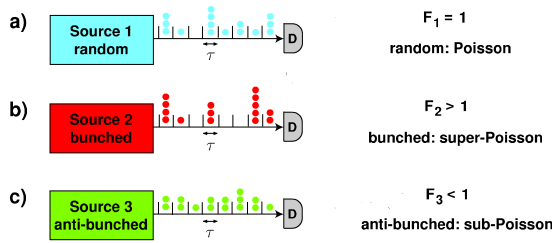
Figure 5.1: Three different types of particle sources. (a) Random source with pure Poissonian statistics; (b) "bunched" source; (c) "anti-bunched" source. All the three sources are characterized by the same average number of emitted particles: the variance, however, distinguishes among them (after [86]).

The first source emits completely uncorrelated particles. A bosonic one has a natural tendency to emit "bunches" of particles, which give rise to increased variance and Fano factor. On the contrary, a fermionic source emits "anti-bunched" particles, giving rise to a highly ordered sequence of emission events in time and comparatively small fluctuations which depress the Fano factor. The anti-bunching is a direct consequence of the Fermi-Dirac statistics of electrons. The average particle current of a source can be defined as $i = n/T$, where T is the time over which averaging occurs and n is the number of particles emitted in the time T. A Fano factor described in terms of the beam currents can be derived : in the stationary limit analogous results are obtained. An experi-
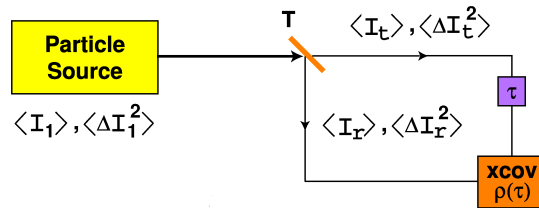
Figure 5.2: Scheme of a "Hanbruy-Brown and Twiss-like" experiment. The beam of a source with Fano factor F_1 is split in two, reflected and transmitted, beams with probability T and $1 - T$. The two beams are cross-correlated after a relative delay τ is imposed (after [86]).

mental setup to determine the Fano factor of a particle source is schematically depicted in Fig. 5.2: the current I_1 from a source is divided by a beam splitter in a reflected I_r and a transmitted I_t beam. After being delayed for a time τ, the two beams are cross-correlated and the cross-covariance $\rho(\tau)$ is evaluated as

$$\rho(\tau) = \frac{\langle \Delta I_r(0) \Delta I_t(\tau) \rangle}{\sqrt{\langle (\Delta I_r)^2 \rangle \langle (\Delta I_t)^2 \rangle}} \; .$$

For $T = 1/2$ and $\tau = 0$ one has the important result $\rho(0) = (F_1 - 1)/(F_1 + 1)$ [86], where F_1 is the Fano factor of the source. This approach has been employed by Hanbury-Brown and Twiss (HBT) using as a source a high-pressure mercury lamp [87]. As expected, they found a positive cross-correlations $\rho(0)$, signalling the bunching of photons giving a super-Poissonian Fano factor for the source. Non-thermal sources of light have subsequently been employed, where the statistical properties of the beam fluctuations deviate from the ones discussed above: for instance in the case of laser light the fluctuations can be suppressed down to the Poissonian limit. A single-photon emitter consisting in a laser-triggered quantum dot has been shown [88] to produce strongly anti-bunched photons. Very recently, a HBT experiment with electron beams has been performed in the solid state [89, 90]. In the following we describe briefly the experiment by Oliver *et al.* [89]. The scheme of this experiment is de-
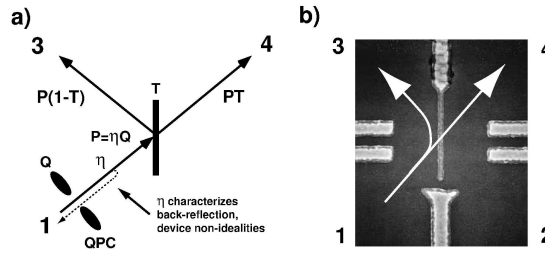
Figure 5.3: The Hanbury-Brown and Twiss experiment with electrons. a) Schematical description of the apparatus. A quantum point contact QPC with transmission probability Q is used as a monochromatic source of electrons which are divided by the beam splitter T, with transmission probability T. The backscattering of electrons in the QPC is described by the suppression factor $0 < \eta < 1$. The reflected (I_3) and transmitted (I_4) currents are cross-correlated. b) SEM image of the actual experimental setup, with metallic gates (light gray) defining the four channels. the central gate is used to create the beam splitter. The gate 2 is not used in the experiment (After [89]).

picted in panel a) of Fig. 5.3: a quantum point contact (QPC) with up to one open transverse mode is exploited as a monochromatic source of electrons with transmission probability Q and Fano factor $1 - Q$ [12]. The beam is divided by a splitter T (transmission probability T) into a a reflected (I_3) and transmitted (I_4) beams, which are subsequently cross-correlated. For $T = 1/2$, the zero-delay cross-correlator is theoretically evaluated as $\rho(0) = P/(P - 2)$, where $P = \eta Q$ and $0 < \eta < 1$ is a suppression parameter which takes into account the backscattering inside the QPC. The results are shown in Fig. 5.4. In the regime $P \to 0$, the QPC is almost closed. The cross correlator $\rho(0) \to 0$, signalling a Poissonian Fano factor for the source: almost uncorrelated electrons are emitted. In the $P \to 1$ limit, one single mode in the QPC transmits electrons, whose beam is strongly affected by their Fermionic statistics: a strong antibunching is obtained therefore the beams are anti-correlated and the Fano factor drops way below the Poissonian limit. In any case, however, a tendency to anti-correlations ($\rho(0) < 0$) is present, leading to a suppression of the noise below the Poissonian limit.
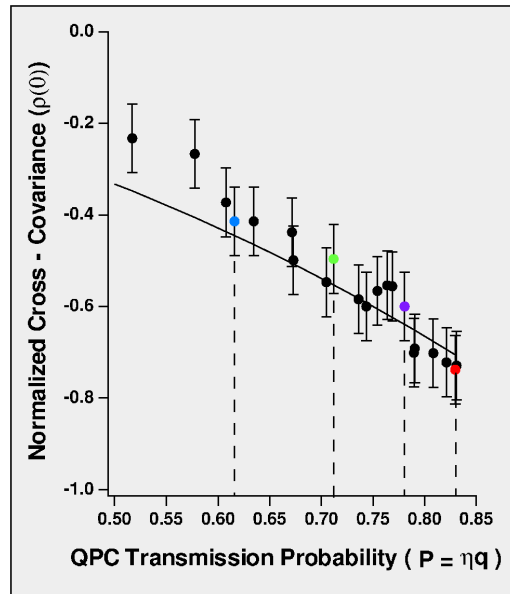
Figure 5.4: Cross-covariance $\rho(0)$ as a function of the effective transmission probability of the QPC $P = \eta Q$. Dots represent the experimental data, while the solid line is the theoretical curve $\rho(0) = P/(P-2)$. (After [89]).

5.3 Noise in double-barrier systems

5.3.1 Noise suppression

Double-barrier systems – such as, for instance, quantum dots – are extremely interesting playgrounds where the noise properties can be studied. In addition to the Fermionic statistics, they show peculiar signatures due to the relevance of interaction effects which affect the transport already at the stationary current level. Quantum dots in the *sequential tunneling* regime show remarkably clear effects due to Coulomb repulsion as for instance the Coulomb-blockade. In these systems, Hershfield *et al.* [91] have studied theoretically the zero-frequency shot noise, also by means of numerical simulations. A similar analysis was undertaken by Korotokov [92], while Hanke *et al.* considered the nonzero frequency limit [93]. In Hershfield's work, a spinless quantum dot was considered by means of a master equation approach. In the thermal regime $eV < k_{\mathrm{B}}T$, the usual result $S = 4k_{\mathrm{B}}TG$ was obtained. In the shot noise regime $eV > \{k_{\mathrm{B}}T, E_{\mathrm{c}}\}$, where E_{c} is the charging energy of the dot, important deviations from the Poissonian regime $S = 2eI$ were found (here, and in the following, we denote the current by I). When only two charge states N and $N + 1$ are relevant to the transport in the dot, one has

$$S = 2eI\frac{\Gamma_+^2 + \Gamma_-^2}{(\Gamma_+ + \Gamma_-)^2} \quad ; \quad I = e\frac{\Gamma_+\Gamma_-}{\Gamma_+ + \Gamma_-} \tag{5.4}$$

where $\Gamma_\pm$ are the input (+, transition $N \rightarrow N+1$) and output (−, transition $N+1 \rightarrow N$) voltage-dependent tunneling rates. The Fano factor is suppressed and the noise attains the minimum value when $\Gamma_+ \rightarrow \Gamma_-$, where $F \rightarrow 1/2$. The shot noise suppression is a direct consequence of the cooperation of the two tunneling barriers together with Coulomb repulsion and Pauli statistics, inducing a strong correlation among the tunneling events. Indeed, suppose the dot is in the state with $N+1$ electrons: no tunneling events will occur on the source barrier unless an electron tunnels outside the dot through the drain barrier. In the extreme asymmetric regime, where the dynamics of the dot is dominated by the most opaque barrier and the additional correlation due to the transparent barrier is not relevant, one obtains $F \rightarrow 1$. In the highly nonlinear transport regime, a similar depression in the shot noise occurs at the onset of each Coulomb staircase step, where a new charge state influences the dynamics of the dot. An experimental verification of these predictions has been performed by Birk *et al.* [94], who considered a metallic grain deposed on a insulator-coated Au substrate. The grain is then contacted by means of a STM
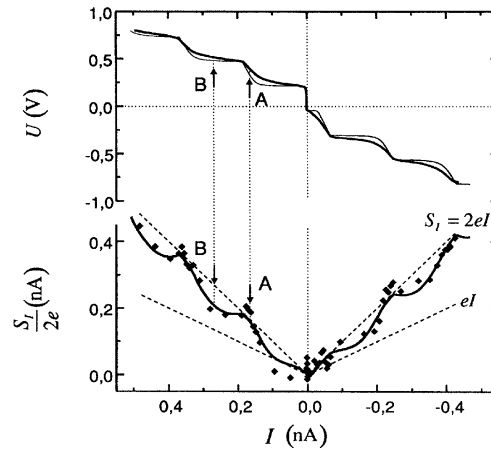
Figure 5.5: (Top panel) Voltage-current curve measured in a metallic-grain SET contacted with a STM tip at 4.2K. The thick line is the experimental observation, while the thin line represents a numerical simulation. The Coulomb staircase, where the *current* increases in steps increasing the voltage, is clearly displayed. (Bottom panel) Zero-frequency shot noise as a function of the current (squares) and numerical simulation (solid line). The arrows spot the maximum and minimum relative values for the noise, the dashed lines represent the $S = 2eI$ and $S = eI$ values. (After [94]).

tip and electons tunnel through the grain forming a SET. Increasing the voltage applied to the tip, a clear evidence of the Coulomb staircase is observed (Fig. 5.5 – top). Correspondingly, the zero-frequency shot noise (Fig. 5.5 – bottom) shows a suppression at the onset of each current step (see the arrow labeled "B", for instance).

5.3.2 Noise enhancement

Despite the Fermionic statistics, noise in double-barrier electronic systems does not always show a suppression below the Poissonian limit. Probably the most famous example of noise enhancement occurring in electronic resonant tunneling structures has been observed by Iannaccone *et al.* [95]. They considered
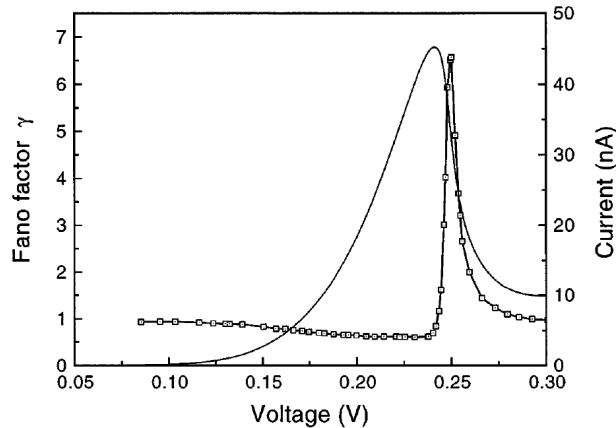
Figure 5.6: Experimental current (solid line) and Fano factor (squares) as a function of the applied voltage in the double-barrier resonant tunneling diode studied by Iannaccone *et al.*. Measurements were performed at the temperature of 77 K. The maximum value of the Fano factor is 6.6, while the minimum is close to 0.5. (After [95])

a double-barrier resonant tunneling diode made by a $GaAs/Al_{0.36}Ga_{0.64}As$ structure, whose $I(V)$ curve exhibits a strong asymmetric peak (Fig. 5.6, solid). In the NDC portion of the curve, a strong super-Poissonian noise is found, with a Fano factor exceeding 6 (Fig. 5.6, squares). The shot noise enhancement has been explained as follows: in the NDC region only the tail of the tunneling density of states of the resonant structure is available, thus the decrease in the current. However, the tunneling of one electron inside the structure from the source terminal dynamically increases the potential of the energy well (Fig. 5.7) shifting the tunneling density of states towards its maximum and increasing the possibility that more electrons tunnel inside the structure from the source lead. Therefore, electrons entering the diode are positively correlated and it is possible to have a strongly enhanced noise. A detailed theoretical analysis of this experiment has been provided by Blanter *et al* [96]. Other works on resonant tunneling structures have recently confirmed the possibility to observe enhanced shot noise [97, 98].

Shot noise enhancement has been theoretically predicted also in quantum dots. As an example, Cottet *et al.* have shown that in a three-terminal quantum dot with ferromagnetic leads [99] or with paramagnetic leads but in the presence of a magnetic field [100], Coulomb interaction is responsible for the appearance of positive cross-correlations among the output currents and/or super-Poissonian Fano factors for the input current noise. The physical mechanism which drives the noise above the Poissonian level is a dynamical spin
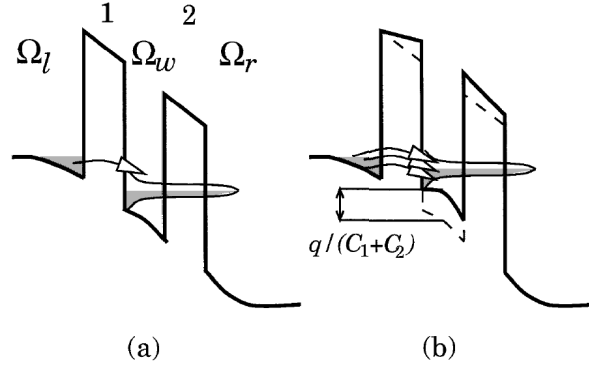
Figure 5.7: The mechanism leading to enhanced shot noise in a resonant tunnel diode. The enhancement is obtained because an electron tunneling into the well (a) from the source terminal raises its potential energy, so that more states are available for tunneling from the source (b). (After [95])

blockade: assuming the dot cannot be doubly-occupied ($eV, k_B T < E_c$), because of the magnetic environment, up and down spins tunnel through the dot with different rates. Those with a lower tunneling rate modulate the transport through the opposite spin-channel, leading to a *bunching of tunneling events*.

Sauret *et al.* [101] recently considered the fluctuations of the spin-resolved current $I_\sigma \equiv I_\uparrow - I_\downarrow$ (where $I_{\uparrow(\downarrow)}$ is the current of electrons with spin $\uparrow$ ($\downarrow$)) and of the spin currents $I_{\uparrow,\downarrow}$. They considered a system without magnetic field or barriers – thus having $\langle I_\sigma \rangle = 0$ – obtaining an interesting results in the case when only two charge states N and $N + 1$ contribute to the transport

$$ S_{\text{charge}} = 2eI \frac{(2\Gamma_+)^2 + (\Gamma_-)^2}{(2\Gamma_+ + \Gamma_-)^2} \quad ; \quad S_{\text{spin}} = 2eI \tag{5.5} $$

where I is the total charge current. While the result for the charge noise S_{charge} is a simple generalization of the Hershfield's formula to the case of a system with a spin-degenerate ground state, the spin noise S_{spin} is strictly poissonian, insensitive to the tunneling barriers details. The result for the spin current can be interpreted as follows: because of the absence of magnetic environment, the electrons coming from the source lead have completely uncorrelated spins. This means that although the next spin can tunnel inside the dot only after the previous has traveled through the drain lead, its spin will be completely uncorrelated. Therefore, from the point of view of the spin-resolved current, no correlation among the barriers is present, in sharp contrast with the result for the charge noise. Allowing the possibility of double dot occupancy, the Pauli exclusion principle implies correlations among the spins tunneling in the dot. As Fig. 5.8 shows, S_{spin} decreases below the Poissonian value, while the charge noise increases.

Finally, we cite the recent result by Thielmann *et al.*, where super-Poissonian shot noise has been theoretically reported in a many-channels molecular quantum dot in the sequential tunneling regime [102].
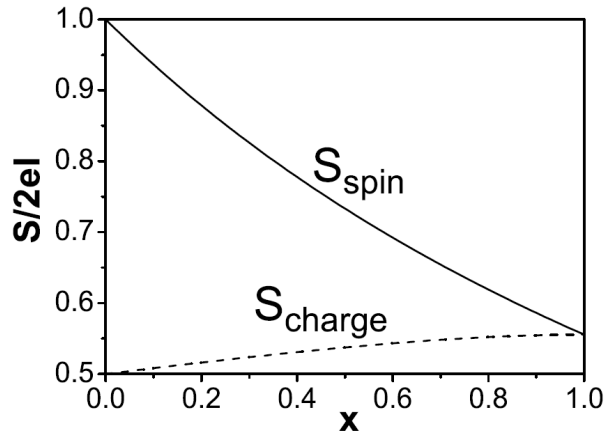
Figure 5.8: Charge (S_{charge}) and spin (S_{spin}) noises as a function of x, the adimensionalized tunneling rate for the transition $N + 1 \rightarrow N + 2$. $x = 0$ means no double occupancy of the dot, $x = 1$ means completely open $N + 1 \rightarrow N + 2$ transition channel. The case $\Gamma_- = 2\Gamma_+$ has been considered. (After [101])

5.3.3 Noise in LL quantum dots

Recently, the zero-frequency shot noise of a one-dimensional quantum dot in the sequential tunneling regime has been extensively studied by Braggio *et al.* [73] and by Kinaret *et al.* [72]. They both considered a one-dimensional spinless LL with interaction parameter g. In this system, two impurity levels emerge above the Fermi level and define a quantum dot. Transport through this system has been considered in the sequential tunneling regime: employing a master equation approach the nonlinear regime has been analyzed. In the two systems, however, radically different assumptions have been made: in [73] the collective excitations of the dot have been assumed to be strongly relaxed, while in [72] nonrelaxed excitations have been assumed and a phenomenological relaxation rate γ_p^{-1} has been introduced in the master equation. Figure 5.9 shows the results by Braggio *et al.* for the Fano factor F in the nonlin-
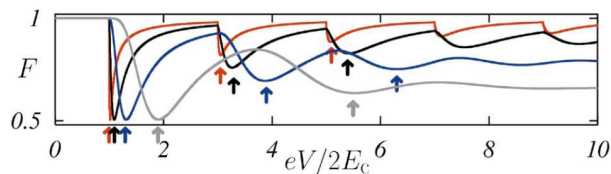
Figure 5.9: (Fully relaxed case) Fano factor F as a function of the transport voltage $eV/2E_c$ at zero temperature for a level spacing $\varepsilon \ll E_c$, strongly asymmetric barriers and different interaction constants: $g = 1$ (red), $g = 0.8$ (black), $g = 0.6$ (blue) and $g = 0.4$ (grey). (After [73])

ear transport regime. A relatively small level spacing $\varepsilon \ll E_c$ has been chosen and strongly asymmetric barriers have been considered. Inside the conduction

region, a sequence of dips are present in the Fano factor, corresponding to an increasing number of charge states contributing to the transport. This result resembles the Hershfield noise suppression: however, non-Fermi liquid correlations give rise to peculiar signatures. For instance, the dip position for an interacting systems exhibits a detuning δV_{dip} around the noninteracting value for sufficiently asymmetric tunneling barriers. This detuning is a complicated function of the interaction parameter g and is clearly detectable in the curves shown in Fig. 5.9. We also notice that increasingly strong interactions lead to a more pronounced suppression of the noise. In the case of nonrelaxed plas-
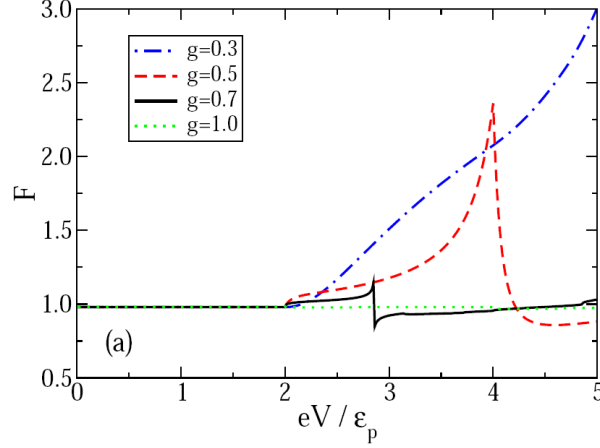
Figure 5.10: (Nonrelaxed case) Fano factor *F* as a function of the transport voltage $eV/\varepsilon_{\mathrm{p}}$ at zero temperature (ε_{p} is the plasmon energy) with asymmetric barriers as in Fig. 5.9 and different interaction parameters: $g = 1$ (green), $g = 0.7$ (black), $g = 0.5$ (red) and $g = 0.3$ (blue). (After [72])

mons, the results are strikingly different. Figure 5.10 shows the behavior of the Fano factor in the nonlinear transport regime for strongly asymmetric barriers. For an interacting system, the Fano factor reaches strong superpoissonian values when the voltage is high enough to open a transport channel involving a plasmon. Increasing the interaction, this effect is even more pronounced. The origin of the noise enhancement can be explained as follows: for sufficiently high voltages, the two transport channels (the asterisk denotes a plasmonic excited state of the dot)

$$N \to N + 1 \to N$$
$$N \to N + 1^* \to N$$

compete in the transport. If one of the two channels modulates the other, a condition might be reached where $F > 1$, in analogy with the effect described in [99, 100]. The fluctuation enhancement is due to the presence of *nonrelaxed* excitations: in Fig. 5.11, the Fano factor for $g = 0.5$ and various values of the phenomenological plasmon relaxation rate γ_{p} is shown. The latter is expressed in units Γ_0, the averate tunneling rate of the system. For sufficiently large relaxation rates, any plasmon excitation induced by electron tunneling relaxes
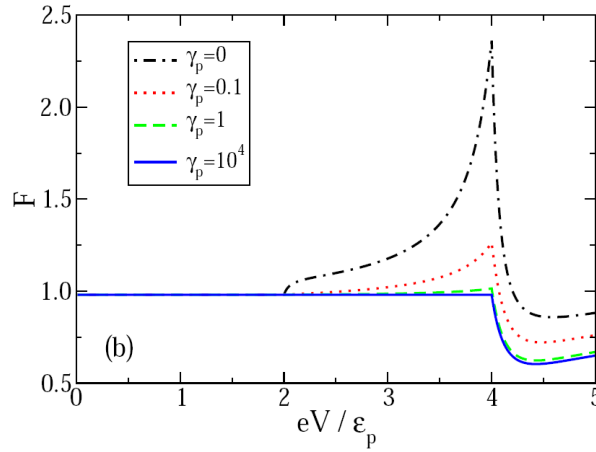
Figure 5.11: (Phenomenological relaxation) Fano factor F as a function of the transport voltage eV/ε_p at zero temperature with asymmetric barriers as in Fig. 5.9 and $g = 0.5$ for different values of the relaxation rate γ_p (units of the average tunneling barrier rate Γ_0): $\gamma_p = 0$ (black), $\gamma_p = 0.1$ (red), $\gamma_p = 1$ (green) and $\gamma_p = 10^4$ (blue). (After [72])

before a subsequent tunneling event. Therefore, as the plasmon relaxation rate increases, the Fano factor recovers the characteristic of the model discussed in [73].

Shot noise in a 1D ring

"Defer no time; delays have dangerous ends." (**W. Shakespeare**)

In this chapter we want to study the shot noise of a one-dimensional quantum ring [21]. Possible experimental realizations of this system include [22, 23]. The 1D ring geometry allows to study the interplay between Fermi statistics, interactions, and Coulomb Blockade. Signatures of this interplay , which were for instance found in the behavior of the linear conductance [103], will reflect in the richness of the interaction-induced noise analyzed below. After a description of the system under investigation (section 6.1), we sketch briefly the technique employed to calculate the noise spectrum (section 6.2) and concentrate on the zero-frequency regime. In section 6.3.1 we present results in the absence of external magnetic flux, while in section 6.3.2 the effects of the latter is briefly investigated. In section 6.3.3 we present an interpretation of the results in terms of a Monte Carlo simulation of the transport dynamics in the system.

6.1 The ring model

The system we want to describe is schematically depicted in Fig. 6.1. It is composed by a one-dimensional quantum ring of radius R, connected to two external leads. The ring will be described by a *spinless* Luttinger liquid (see section 2.2.5) with interaction parameter g. The external leads will be modeled by interacting one-dimensional electron systems, with interaction parameter g_ℓ. For the isolated quantum ring, the Hamiltonian reads

$$H_{\text{ring}} = \frac{E_N}{2}\left(N - N_{\text{g}}\right)^2 + \frac{E_J}{2}\left(J - 2\frac{\Phi}{\Phi_0}\right)^2 + \sum_{n>0} n\varepsilon\, b_n^\dagger b_n\,. \qquad (6.1)$$

where the zero mode $N = N_+ + N_-$ represents the total number of excess charges in the ring and $J = N_+ - N_-$ represents the imbalance between clockwise and anti-clockwise moving charges. We assume the ring is capacitively
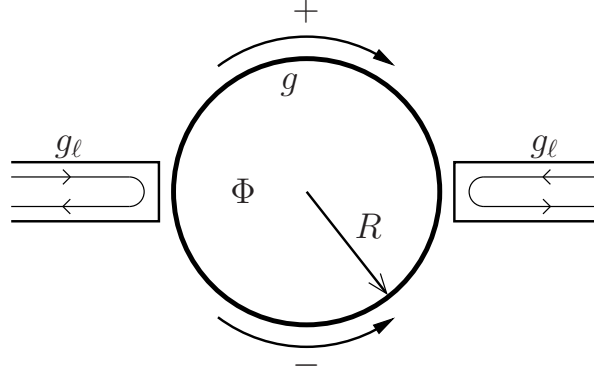
Figure 6.1: Schematic description of the one-dimensional ring under investigation. The ring has radius R and the one-dimensional leads are characterized by the interaction parameter g_ℓ, while the ring by the parameter g. Clockwise "+" and anti-clockwise "-" current components are displayed.

coupled to an external gate which induces an extra charge eN_g. Furthermore, the ring is pierced by an external magnetic flux Φ (we denote the flux quantum $\Phi_0 = h/e$). The zero modes N, J satisfy the condition $N + J =$ even. The charging energy E_N is mainly due to Coulomb interactions. However, being strongly influenced by the external circuit and metallizations, it will be treated as a free parameter which sets the highest energy attainable as in the case of the one-dimensional quantum dot (see chapter 3). The orbital addition energy is $E_J = v_\mathrm{F}/2R \ll E_N$. The last term in (6.1) is the contribution due to bosonic charge density waves, with $b_n^\dagger$ (b_n) the creation (annihilation) operator for an excitation with energy $n\varepsilon$, with $\varepsilon = v/R$ and $v = v_\mathrm{F}/g$ the group velocity of the collective excitations in the ring. The leads Hamiltonian is similar to (6.1) but with a continuous dispersion relation for the CDW modes. The ring and the leads are coupled by a tunneling Hamiltonian which connects the ring and the leads in the tunneling points x_1 and x_2

$$H_\mathrm{t} = \sum_{i=1,2} \left[t_i \psi^{(i)\dagger}(x_i) \psi^{(\mathrm{ring})}(x_i) + \mathrm{h.c.} \right] , \tag{6.2}$$

expressed in terms of the bosonized form of the Fermi operators (see section 2.2.5). In the following we will limit our analysis to the sequential tunneling regime. Within this framework, we will evaluate the charge $I_N^{(i)}$ and magnetization $I_J^{(i)}$ tunneling currents at the i-th barrier, which are related to the clockwise and anti-clockwise contributions $I_+^{(i)}$ and $I_-^{(i)}$ by

$$I_N^{(i)} = I_+^{(i)} + I_-^{(i)}$$
$$I_J^{(i)} = I_+^{(i)} - I_-^{(i)}$$

The charge and angular currents are related to the variations of N and J that occur because of the tunneling. The latter, in particular, can be related to the

ring magnetization. An external source-drain voltage is connected to the external leads in order to drive current in the nonlinear regime: the electrochemical potential in the i-th lead is assumed to be constant and fixed to the value $\mu_i = (-1)^i eV/2$, with a symmetric voltage drop on the tunneling barriers.

6.2 Evaluation of noise

We want to evaluate the frequency-resolved charge and magnetization current noise, defined as the symmetrized correlator ($\nu \in \{N, J\}$)

$$S_\nu^{(ij)}(\omega) = \int_{-\infty}^{\infty} dt \, e^{i\omega t} \langle \Delta I_\nu^{(i)}(t) \Delta I_\nu^{(j)}(0) + \Delta I_\nu^{(i)}(0) \Delta I_\nu^{(j)}(t) \rangle \qquad (6.3)$$

where we have defined the current fluctuations $\Delta I_\nu^{(i)}(t) \equiv I_\nu^{(i)}(t) - \langle I_\nu^{(i)} \rangle$ "centered" around the stationary average values $\langle I_\nu^{(i)} \rangle$. In order to evaluate the average currents and their correlators, we set up a master equation for the occupation probability of the ring states. As in the case of the one-dimensional quantum dot, we assume here the complete relaxation of collective excitations in the LL describing the ring. Therefore, the only dynamical variables are N and J. The master equation reads

$$\partial_t P_{|N,J\rangle}(t) = \sum_{\substack{N'=N\pm1 \\ J'=J\pm1}} \sum_{i=1,2} \left[P_{|N',J'\rangle}(t) \Gamma_{|N',J'\rangle \to |N,J\rangle}^{(i)} - P_{|N,J\rangle}(t) \Gamma_{|N,J\rangle \to |N',J'\rangle}^{(i)} \right]$$

$$(6.4)$$

and is defined over the set of ring states relevant to the transport for given external voltages and magnetic flux. Here, we proceed in very general terms. Later on, we will specify to the relevant case of only two charge states in the ring. We have introduced the tunneling rate through the i-th barrier $\Gamma_{|N,J\rangle \to |N',J'\rangle}^{(i)}$. Since the model and the approximations made insofar are very similar to the ones described in chapter 3, we omit the details and quote only the results. For temperatures $k_B T < \varepsilon$ we obtain the tunneling rates

$$\Gamma_{|N,J\rangle \to |N',J'\rangle}^{(i)}(\Delta E) = \delta_{N'=N\pm1} \delta_{J'=J\pm1} \Gamma_0^{(i)} \sum_{p=-1}^{\infty} a_p \gamma(\Delta E - p\varepsilon) \qquad (6.5)$$

where $\Delta E = E_{|N',J'\rangle} - E_{|N,J\rangle}$ is the energy difference of the considered transition. We have

$$\Gamma_0^{(i)} = \left(1 - e^{-\varepsilon/\omega_c}\right)^{(g+1/g)/2} \frac{2\omega_c G_i}{e^2 \Gamma(1/g_\ell)}, \qquad (6.6)$$

with the intrinsic barriers conductance $G_i = \pi e^2 |t_i|^2 / \omega_c^2$ and

$$a_p = a_p^{(0)} + \frac{1}{2}\left(g + \frac{1}{g}\right) e^{-\beta\varepsilon} \left[a_{p+1}^{(0)} + a_{p-1}^{(0)} - 2a_p^{(0)}\right], \qquad (6.7)$$

where the zero-temperature ring weights are

$$a_p^{(0)} = \frac{\Gamma((g+1/g)/2 + q)}{\Gamma((g+1/g)/2) \, q!} \theta(q). \qquad (6.8)$$

95

The leads contribution $\gamma(x)$ is given by

$$\gamma(x) = \frac{1}{2\pi} e^{-\beta x/2} \left| \Gamma\left(\frac{1}{2g_\ell} + i\frac{\beta x}{2\pi}\right) \right|^2 \left(\frac{2\pi}{\beta \omega_c}\right)^{1/g_\ell - 1}. \tag{6.9}$$

The periodic boundary conditions in the ring modify the structure of the inter-action parameter contribution leading to the appearance of terms of the form $(g + 1/g)/2$. Introducing a labeling for the states $|N, J\rangle \equiv \alpha$, and defining the total transition rate $\Gamma_{\alpha \to \beta} = \Gamma^{(1)}_{\alpha \to \beta} + \Gamma^{(2)}_{\alpha \to \beta}$ we can rewrite the master equation as

$$\partial_t P_\beta(t) = \sum_{\alpha \neq \beta} \left[P_\alpha(t) \Gamma_{\alpha \to \beta} - P_\beta(t) \Gamma_{\beta \to \alpha} \right]. \tag{6.10}$$

which leads to the compact matrix form

$$\partial_t \mathbf{P}(t) = \mathbf{M} \mathbf{P}(t) \tag{6.11}$$

where we have defined the vector $\mathbf{P}$ of the ring states occupation probabilities and the transition matrix $\mathbf{M}$ as

$$M_{\alpha\beta} = \begin{cases} \Gamma_{\beta \to \alpha} & \text{if } N_\alpha = N_\beta \pm 1 \text{ and } J_\alpha = J_\beta \pm 1 \\ -\sum_{\alpha \neq \beta} \Gamma_{\beta \to \alpha} & \text{if } N_\alpha = N_\beta \text{ and } J_\alpha = J_\beta \\ 0 & \text{elsewhere} \end{cases} \tag{6.12}$$

The formal solution of (6.11) is clearly

$$\mathbf{P}(t) = e^{\mathbf{M}t} \mathbf{P}(0)$$

where the vector $\mathbf{P}(0)$ is determined by the boundary condition at $t = 0$. From the definition (6.12) it is clear that for each β

$$\sum_\alpha M_{\alpha\beta} = 0, \tag{6.13}$$

whence it follows promptly

$$\sum_{\alpha,\beta} M_{\alpha\beta} P_\beta(t) = 0 = \partial_t \left(\sum_\beta P_\beta(t) \right)$$

ensuring the normalization of the master equation solution. The sum rule (6.13) warrants the presence of a left and a right eigenvectors with zero eigen-value. While this is not a general rule, the eigenvector belonging to the zero eigenvalue is generally non-degenerate. In the system we are discussing this is precisely the case. therefore, we will assume in the following the existence of a non-degenerate right eigenvector $\mathbf{P}_0$ with zero eigenvalue. Physically, the eigenvector $\mathbf{P}_0$ represents the stationary probability distribution for the occu-pation probabilities of the ring states. In order to calculate the current through the ring, we introduce the matrixes $\mathbf{v}^{(i),\lambda}$, with the index λ referring to the clockwise ($\lambda = +1$) and anti-clockwise ($\lambda = -1$) components of the tunneling current. They are defined as

$$v^{(i),\lambda}_{\alpha\beta} = \begin{cases} \Gamma^{(i)}_{\beta \to \alpha} & \text{if } N_\alpha - N_\beta = (-1)^i \text{ and } J_\alpha - J_\beta = (-1)^i \lambda \\ -\Gamma^{(i)}_{\beta \to \alpha} & \text{if } N_\alpha - N_\beta = (-1)^{i+1} \text{ and } J_\alpha - J_\beta = (-1)^{i+1} \lambda \\ 0 & \text{elsewhere} \end{cases}. \tag{6.14}$$

It is then possible to define matrixes for the charge and magnetization current

$$
\begin{aligned}
\mathbf{v}^{(i),N} &= \sum_{\lambda} \mathbf{v}^{(i),\lambda} \\
\mathbf{v}^{(i),J} &= \sum_{\lambda} \lambda \mathbf{v}^{(i),\lambda} .
\end{aligned}
$$

The stationary average values of charge (I_N) and angular (I_J) currents are easily obtained as ($\nu = N, J$)

$$
\langle I_\nu^{(i)} \rangle = -e\mathrm{Tr}[\mathbf{v}^{(i),\nu}\mathbf{P}_0] \tag{6.15}
$$

(the trace of a vector has been defined as the sum of its components). We define now the zero-modes matrixes **N** and **J**, which are expressed in components by

$$
N_{\alpha\beta} = N_\alpha \delta_{\alpha\beta} \quad ; \quad J_{\alpha\beta} = J_\alpha \delta_{\alpha\beta} ,
$$

satisfying the following commutation relations

$$
[\mathbf{N}, \mathbf{M}] = -\mathbf{v}^{(1),N} + \mathbf{v}^{(2),N} \quad ; \quad [\mathbf{J}, \mathbf{M}] = -\mathbf{v}^{(1),J} + \mathbf{v}^{(2),J} , .
$$

With the aid of these matrixes it is possible to show that the stationary currents are independent of the barriers

$$
\langle I_\nu^{(1)} \rangle = \langle I_\nu^{(2)} \rangle . \tag{6.16}
$$

Following [91], we can use the elements defined above to calculate the correlators involved in (6.3). The general expression reads

$$
\langle I_\nu^{(i)}(t) I_\nu^{(j)}(0) \rangle = e^2 \left[\theta(t) V_{ij}^{\gamma\gamma'}(t) + \theta(-t) V_{ji}^{\gamma\gamma'}(-t) \pm \delta_{i,j=2,1}\delta(t)\tilde{V}_i^\gamma \right] \tag{6.17}
$$

where the sign $+ (-)$ refers to $i = 2$ ($i = 1$),

$$
V_{ij}^{\gamma\gamma'}(t) = \mathrm{Tr}\{\mathbf{v}^{(i),\gamma} e^{\mathbf{M}t} \mathbf{v}^{(j),\gamma'} \mathbf{P}_0\} \tag{6.18}
$$

and

$$
\tilde{V}_i^\gamma = \begin{cases} \mathrm{Tr}\{[\mathbf{N}, \mathbf{v}^{(i),N}]\mathbf{P}_0\} & \text{if } \nu = N \\ \mathrm{Tr}\{[\mathbf{J}, \mathbf{v}^{(i),J}]\mathbf{P}_0\} & \text{if } \nu = J \end{cases} . \tag{6.19}
$$

The equation (6.17) is especially simple if it is possible to spectrally decompose the propagator $\exp(\mathbf{M}t)$ by means of a set of right eigenvectors only. This is the case, when the transport is described by a one-step Markov process, which satisfies the detailed balance principle

$$
M_{\alpha\beta}(\mathbf{P}_0)_\beta = M_{\beta\alpha}(\mathbf{P}_0)_\alpha
$$

so that it is possible to define the symmetrized version $\bar{\mathbf{M}}$ of the matrix $\mathbf{M}$

$$
\bar{\mathbf{M}} = \mathbf{TMT}^{-1} \quad ; \quad (\bar{\mathbf{M}})_{\alpha\beta} = \frac{1}{\sqrt{(\mathbf{P}_0)_\alpha}}(\mathbf{M})_{\alpha\beta}\sqrt{(\mathbf{P}_0)_\beta} . \tag{6.20}
$$

The matrix $\bar{\mathbf{M}}$ has a spectrum of real eigenvalues λ_k ($0 \leq k \leq \dim(\bar{M}) - 1$) with eigenvectors $\mathbf{x}_k$. For many physically relevant systems one has $\lambda_k \leq 0$[104],

with a nondegenerate zero eigenvector, which we choose to label λ_0. By means of the matrix $\mathbf{T}$ we can transform also the current matrices and the stationary eigenvector $\mathbf{P}_0$. Exploiting the representation of the symmetrized propagator over the basis spanned by the $\mathbf{x}_k$ we finally obtain the important expression for (6.17)

$$\langle I_\nu^{(i)}(t) I_\nu^{(j)}(0)\rangle \;=\; e^2\theta(t)\sum_{k\neq 0}\left(\bar{\mathbf{P}}_0^{\mathrm{t}}\bar{v}^{(i),\nu}\mathbf{x}_k\right)e^{\lambda_k t}\left(\mathbf{x}_k^{\mathrm{t}}\bar{v}^{(j),\nu}\bar{\mathbf{P}}_0\right) \tag{6.21}$$

$$+\; e^2\theta(-t)\sum_{k\neq 0}\left(\bar{\mathbf{P}}_0^{\mathrm{t}}\bar{v}^{(j),\nu}\mathbf{x}_k\right)e^{-\lambda_k t}\left(\mathbf{x}_k^{\mathrm{t}}\bar{v}^{(i),\nu}\bar{\mathbf{P}}_0\right) \tag{6.22}$$

$$\pm\; \delta_{i,j=2,1}\delta(t)\bar{\mathbf{P}}_0^{\mathrm{t}}\left[\mathbf{Y},\mathbf{v}^{(i),\nu}\right]\bar{\mathbf{P}}_0 \tag{6.23}$$

with $\mathbf{Y}_\nu = \mathbf{N}\,(\mathbf{J})$ for $\nu = N\,(J)$. After some algebraic rearrangement we rewrite (6.3) as

$$S_\nu^{(ij)}(\omega) = -4e^2\sum_{k\neq 0}C_\nu^{(ij)}(k)\frac{\lambda_k}{\omega^2+\lambda_k^2}\mp 2e^2\delta_{i,j=2,1}\bar{\mathbf{P}}_0^{\mathrm{t}}\left[\mathbf{Y}_\nu,\mathbf{v}^{(i),\nu}\right]\bar{\mathbf{P}}_0 \tag{6.24}$$

with the sign $-$ (+) if $i = j = 2$ (1) and

$$C_\nu^{(ij)}(k) = \left(\bar{\mathbf{P}}_0^{\mathrm{t}}\bar{v}^{(i),\nu}\mathbf{x}_k\right)\left(\mathbf{x}_k^{\mathrm{t}}\bar{v}^{(j),\nu}\bar{\mathbf{P}}_0\right). \tag{6.25}$$

In the stationary $\omega \to 0$ limit, the noise is independent of the barriers indexes

$$S_\nu^{(ij)}(\omega \to 0) \equiv S_\nu \tag{6.26}$$

By means of the symmetrized matrixes, we can express the average stationary currents

$$\langle I_\nu\rangle = -e\bar{\mathbf{P}}_0^{\mathrm{t}}\bar{\mathbf{v}}^{(i),\nu}\bar{\mathbf{P}}_0. \tag{6.27}$$

where we have suppressed the barrier index because of (6.16). The expression (6.24) is analytically manageable only when $\dim(\mathbf{M})$ is small and, generally, only in the $T = 0$ regime. However, it is particularly useful for numerical evaluations with standard numerical tools [105].

6.3 Results

In analogy with what discussed in chapter 4, with $E_N \gg E_J$ only two charge states N and $N+1$ are involved in the transport processes. Exploiting the condition $(-1)^N = (-1)^J$, we need to specify the value of J only in order to fully identify a particular ring state: we identify therefore the labeling discussed in the previous section with $(N, J) \to J$. At low temperature $k_\mathrm{B}T \ll E_J$, to a good approximation only a finite number of states is involved in the transport $J \in \{J_\mathrm{min}, \ldots, J_\mathrm{max}\}$.

6.3.1 Zero magnetic flux

In the case $\Phi = 0$, the states J and $-J$ are degenerate, therefore $J_\mathrm{min} = -J_\mathrm{max}$. In the following, we assume $V > 0$ and N even. We concentrate on the (V, N_g)
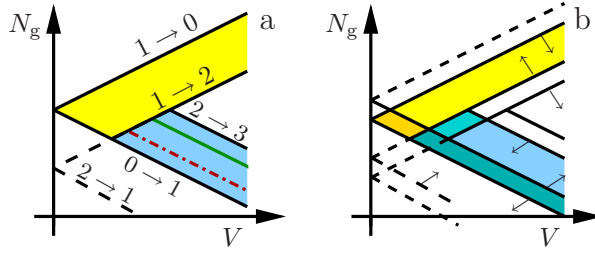
Figure 6.2: (a) Scheme of the relevant transport regions in the (V, N_g) plane for $\Phi = 0$ and N even. Solid lines denote detectable conductance peaks, the involved $|J|$ values are denoted. The black lines represent transitions which do not involve CDWs. The green line represents the transition $2 \to 1$ with the excitation of one CDW. Yellow region: three-states regime $_{\max} = 1$. Cyan region: 5 states regime $J_{\max} = 2$. (b) Same scheme as in (a), for $0 < \Phi < \Phi_0/2$. Each transition line is now split in two (for the sake of simplicity, the CDW-related green lines have been omitted). Arrows indicate the lines evolution increasing Φ.

plane regions where at most $J_{\max} = 2$ – yellow and cyan in Fig. 6.2 (a). The, **M** is a 5×5 tridiagonal matrix. By means of (6.27) and (6.24) we can calculate the average current $\langle I_\nu \rangle$ and the noise $S_\nu^{(ij)}(\omega)$. In the following, unless otherwise specified, we will concentrate on the stationary limit of the noise (6.26). We define the Fano factor for the charge noise and a *generalized* Fano factor for the magnetization noise

$$F_N \equiv \frac{S_N}{2e\langle I_N \rangle} \quad ; \quad F_J \equiv \frac{S_J}{2e\langle I_N \rangle}.$$

The only analytically manageable results in the 5 states regime are those at $T = 0$, which nevertheless describe quite well also the finite-temperature regime $k_B T \approx 0.1 E_J$. We quote them below

$$\langle I_N \rangle = \frac{e}{\tau_0} \frac{(1 + r_1)}{1 + r_1 r_2 + (1 + r_1)\tau_1/\tau_0}, \qquad \langle I_J \rangle = 0 \tag{6.28}$$

$$F_N = 1 + 2 \frac{r_1(1 - r_2)^2 - (1 + r_1 r_2)(1 + r_1)\tau_1/\tau_0}{[1 + r_1 r_2 + (1 + r_1)\tau_1/\tau_0]^2} \tag{6.29}$$

$$F_J = 1 - 2r_1 \frac{1 - r_1}{1 + r_1} \tag{6.30}$$

$$r_1 = \Gamma_{1\to2}^{(1)}/\Gamma_{1\to0}^{(1)}, \quad r_2 = 2\Gamma_{0\to1}^{(2)}/\Gamma_{2\to1}^{(2)} = \tau_2/\tau_0. \tag{6.31}$$

Here, r_1 represents the populating ratio between the states $J = 0$ and $|J| = 2$. For $r_1 > 1$, the transition $1 \to 2$ is favored in comparison to $1 \to 0$. The ratio r_2 represent the escape ratio from $J = 0$ and $|J| = 2$. The stationary occupation probabilities ratio for the states $|J| = 2$ and $J = 0$ can be expressed

as $2P_2/P_0 = r_1 r_2$. Finally, we have defined the dwell times of the ring states

$$\tau_0 = \frac{1}{2\Gamma_{0\to1}^{(2)}} \tag{6.32}$$

$$\tau_1 = \frac{1}{\Gamma_{1\to0}^{(1)} + \Gamma_{1\to2}^{(1)}} \tag{6.33}$$

$$\tau_2 = \frac{1}{\Gamma_{2\to1}^{(2)}} . \tag{6.34}$$

In the case of three states only (yellow region, Fig. 6.2 (a)), $r_1 = 0$ and we re-obtain the well-known results for a quantum dot with a degenerate ground state [101, 104] – see also eq. 5.5

$$F_N = \frac{\tau_0^2 + \tau_1^2}{(\tau_0 + \tau_1)^2} < 1 \quad ; \quad F_J = 1 \tag{6.35}$$

In the five states region (cyan, Fig. 6.2 (a)), on the contrary, new dynamics are found. If the dwell times of the $|J| = 2$ and $J = 0$ are non-degenerate ($r_2 \neq 1$), we can have a superpoissonian charge noise ($F_N > 1$) if the asymmetry $\mathcal{A} \equiv \Gamma_0^{(1)}/\Gamma_0^{(2)} > \mathcal{A}_c$ with

$$\mathcal{A}_c = \frac{2\bar{\Gamma}_{0\to1}^{(2)}}{\bar{\Gamma}_{1\to0}^{(1)} + \bar{\Gamma}_{1\to2}^{(1)}} \frac{(1 + r_1 r_2)(1 + r_1)}{r_1(1 - r_2)^2} . \tag{6.36}$$

Here, we have defined the normalized rates $\bar{\Gamma}_{\alpha\to\beta}^{(i)} \equiv \Gamma_{\alpha\to\beta}^{(i)}/\Gamma_0^{(i)}$. Note that in the $\mathcal{A} \gg \mathcal{A}_c$, one has $\tau_1 \ll \tau_{0,2}$, so that the transport dynamics is dominated by the two latter time scales. Their inhomogeneity, driven by the interactions, is the responsible for the superpoissonian noise of the charge current. On the contrary, F_J depends on r_1 only. It is possible to obtain $F_J > 1$ only with a "populating inversion". Notice that $r_1 > 1$ does not imply an *inversion of population* $P_2 > P_0$. For interaction $0.5 < g < 1$, the region with $J_{max} = 2$ is split by the line $E_{2\to1} = eV/2 + E_N(N_g - 1/2) + 3E_J/2 = \varepsilon$ (green line in Fig. 6.2 (a)), corresponding to the transition $2 \to 1$ involving a CDW in the final state. We denote these regions as *I* and *II*, depending on $E_{2\to1} < \varepsilon$ or $> \varepsilon$. If $g = 1$, the green line collapses ontop the transition $0 \to 1$ and only region *II* is present; if $g < 0.5$ only region *I* is present, because the green line falls outside the cyan zone.

In Fig. 6.3, the values of F_N (a) and F_J (b), calculated along the line $N_g = 1/2 + 0.93 E_J/E_N - eV/2E_N$ (red dash-dot line in Fig. 6.2a), are shown as a function of the offset adimensionalized voltage $(eV - 2.43E_J)/\varepsilon$. Both exhibit clear jumps as a consequence of the excitation of CDW modes in the transitions $|J| = 1 \to J = 0$ and $|J| = 1 \to |J| = 2$. In the absence of interactions ($g = 1 = g_\ell$, magenta curves) the plasmonic modes are degenerate $\varepsilon = 2E_J$. Since $E_{1\to2} = E_{1\to0} + 2E_J$ and $E_{2\to1} = E_{0\to1} + 2E_J$, from (6.5) it is clear that $r_1 < 1$ and $r_2 = 1$, leading always to at most Poissonian noise. With an interacting ring, the degeneracy is lifted ($\varepsilon > 2E_J$) so that it is possible to have $r_2 \neq 1$. In this case it is possible to achieve $F_N > 1$, if $\mathcal{A} > \mathcal{A}_c$. The super-Poissonian charge noise is robust against the leads interactions as can be seen in Fig. 6.3
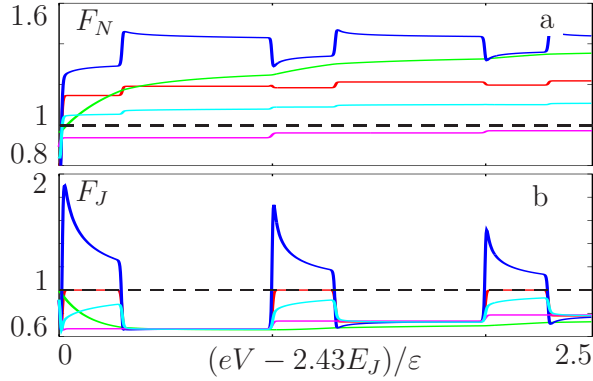
Figure 6.3: Fano factors as a function of $(eV - 2.43E_J)/\varepsilon$, where V varies according to $N_g = 1/2 + 0.93E_J/E_N - eV/2E_N$, with $k_B T = 0.02E_J$ and $\mathcal{A} = 20$. (a) F_N for an interacting ring, $g = 0.7$, and different interactions in the leads: $g_\ell = 1$ (red), 0.9 (cyan), 0.5 (green), 1.2 (blue); magenta: $g = g_\ell = 1$. (b) F_J, parameters and colors as in (a).

(a). In particular, and in striking contrast with the behavior of F_J, the charge noise is not sensitive to the presence of repulsive $g_\ell < 1$ or attractive $g_\ell > 1$ interactions in the leads. On the contrary, for the magnetization noise, it is *crucial* to have $g_\ell > 1$ in order to obtain super-Poissonian values.

For an interacting ring, in region I it is always $r_2 = 1$. Moving along the red dash-dot line $N_g = 1/2 + 0.93E_J/E_N - eV/2E_N$, one can identify two energy regions $\sigma_\pm(n)$

$$\begin{aligned} \sigma_-(n) & \quad \text{if } (n-1)\varepsilon < eV - 2.43E_J < (n-g)\varepsilon \\ \sigma_+(n) & \quad \text{if } (n-g)\varepsilon < eV - 2.43E_J < n\varepsilon. \end{aligned}$$

In these two regions, for r_1 one has

$$r_1 = \begin{cases} 1 & \text{in } \sigma_-(n) \\ n/(n+1) & \text{in } \sigma_+(n) \end{cases}$$

In $\sigma_-(n)$, for $\mathcal{A} \gg \mathcal{A}_c$ and $g_\ell = 1$, the Fano factors reach the asymptotic limits $F_N = 1 + 2/9$ and $F_J = 1$. By tuning the voltage V, one periodically enters the regions $\sigma_+(n)$, where the Fano factor depends on the details of the interactions. For noninteracting leads one has

$$F_N = 1 + \frac{2n(n+\lambda)}{(3n+\lambda)^2}, \quad F_J = 1 - \frac{2n\lambda}{(n+\lambda)(2n+\lambda)}. \tag{6.37}$$

with $\lambda = (g + g^{-1})/2$. For *interacting* leads, one finds smoothened steps in F_N and F_J, with a power law behavior as a function of V. For particularly strong interactions $g \lesssim 0.5$, the smoothening of the step-like structure is almost complete. It is interesting to notice the strong increase of F_N, as compared to the suppression of F_J (green curves). In Fig. 6.4, the critical asymmetry $\mathcal{A}_c$ is plotted in the plane XY, where $X = 1/2 - N_g - 1.5E_J/E_N + eV/2E_N$ and

101
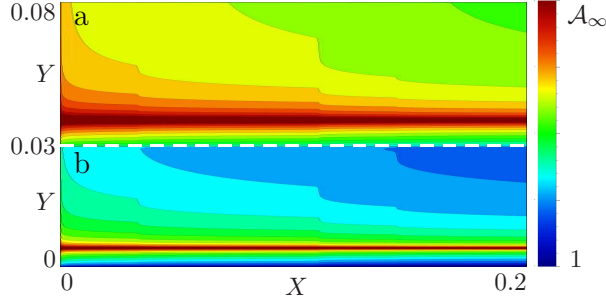
Figure 6.4: Color-contour plot of $\mathcal{A}_c$ for $g = 0.7$, $g_\ell = 0.8$, $k_B T = 0.02 E_J$ in the XY plane (see text). (a) Region I, $\mathcal{A}_\infty = 4100$. (b) Region II, $\mathcal{A}_\infty = 2.6 \, 10^5$.

$Y = -1/2 + N_g - 0.5 E_J/E_N + eV/2 E_N$. Note that $Y = 0$ corresponds to the transition line $0 \rightarrow 1$, $Y = 0.03$ to the line $E_{2\rightarrow 1} = \varepsilon$, and $X = 0$ to the line $1 \rightarrow 2$ (cf. Fig. 6.4 (a)). In the panels (a) and (b), the regions I and II are shown. In both regions, near certain lines parallel to the X axis, for g_ℓ it is possible to have $r_2 = 1$. Here, $\mathcal{A}_c$ diverges and no super-Poissonian charge noise can be achieved. Away from these lines, increasing the voltage, $\mathcal{A}_c$ decreases because of the *increasing number of excited plasmons* present in the output transition. The latter decrease the dwell time τ_1 increasing the "output" rates $\Gamma^{(1)}_{1\rightarrow 0,2}$. For sufficiently high voltages, one can eventually reach the condition $\mathcal{A}_c < 1$.

6.3.2 Non-zero magnetic flux

When $\Phi \neq n\Phi_0/2$ ($n \in \mathbf{Z}$), the degeneracy of the states with $\pm J$ is lifted. As a consequence, the transition lines $J \rightarrow J'$ split in two and move in opposite directions increasing Φ, with a separation proportional to $E_J \Phi/\Phi_0$. In Fig. 6.2 (b) an example of such a situation is shown. The plane (V, N_g) is subdivided in many different regions, in each of which different values of $J_{\min}$ and $J_{\max}$ are found. This makes an analytical diagonalization of the matrix $\bar{\mathbf{M}}$ extremely difficult and we have to resort to numerical evaluations. Many interesting results are found. We restrict our attention on the $0 < \Phi < \Phi_0/2$ regime. The results shown in Fig. 6.5 represent F_N and F_J evaluated along a diagonal line which lies inside zone II at $\Phi = 0$ and are specular with respect to the $\Phi = \Phi_0/2$ when $\Phi_0/2 < \Phi < \Phi_0$. As a whole, the results are periodic, with period Φ_0. Increasing Φ, many moving transition lines cross the diagonal, fixed one. Therefore, it is possible to study the correlation effects on the noise spectrum in a wide range of transport regions. As Fig. 6.5 confirms, the noise exhibits an extremely rich dynamics by tuning the flux. At $\Phi = 0$ one has $\mathcal{A} < \mathcal{A}_c$, so that $F_N < 1$. However, increasing the flux, super-Poissonian charge noise is reached for $\Phi \approx 0.4\Phi_0$, signalling the crossover to a transport regime where $\mathcal{A} > \mathcal{A}_c$. The onset of this region is at $\Phi^* = 0.35\Phi_0$, given by the intersection of the line along where V is varied, $N_g = 1/2 + 1.7 E_J/E_N - eV/2 E_N$, with the upper moving transition line $2 \rightarrow 1$ with one plasmon, $N_g = 1/2 + E_J/2E_N(4/g - 3 + 4\Phi/\Phi_0) - eV/2E_N$, i.e. $\Phi^* = [1.7 + (3 - 4/g)/2]\Phi_0/2$. The possibility of crossing over between
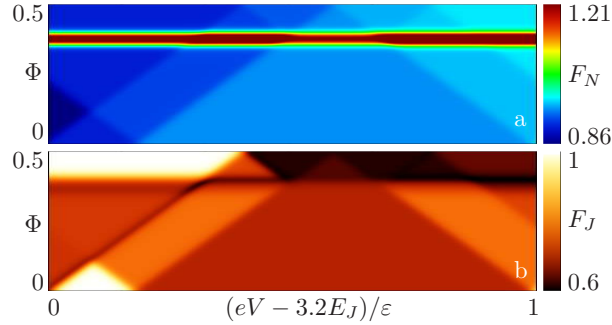
Figure 6.5: Density plot of F_N (a) and F_J (b) as a function of $(eV - 3.2E_J)/\varepsilon$ (voltage moving according to $N_g = 1/2 + 1.7E_J/E_N - eV/2E_N$) and Φ, in units Φ_0. Parameters are: $g = 0.8$, $g_\ell = 1$, $k_B T = 0.02E_J$ and $\mathcal{A} = 20$.

sub- and super-Poissonian behavior as a function of the flux is a signature of the presence of interactions. Indeed, in a noninteracting ring we *always* find sub-Poissonian behavior, regardless of the number of states supporting the transport. Concerning the magnetization noise, interactions in the ring and finite flux are not enough to induce $F_J > 1$ (Fig. 6.5 (b)).

6.3.3 Monte Carlo simulation

As discussed in section 6.3.1, the interaction-induced separation of the time scales τ_0 and τ_2 is responsible for the super-Poissonian behavior of S_N. In order to better understand this mechanism we set-up a BKL Monte Carlo simulation [106] in the $T = 0$ regime. An effective time evolution for the system is modeled by a sequence of discrete steps. At the k-th step, the ring makes the transition $J_k \rightarrow J_{k+1}$. The transition is supposed to be instantaneous, while the average time between the k-th and the $k + 1$-th steps is simply the dwell time $\tau_{|J_k|}$. The situation is schematically depicted in Fig. 6.6. The k-th transition is
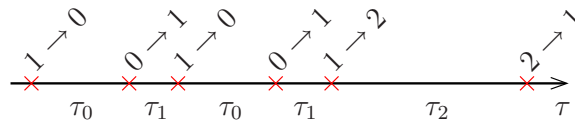
Figure 6.6: Schematic description of the Monte Carlo simulation. The subsequent simulation steps are denoted by red crosses. An example of possible transitions and corresponding dwell times is displayed (see text).

performed according to a conditioned probability given by

$$\Gamma_{J_k \rightarrow J_{k+1}} \Big/ \sum_{J' = J_k \pm 1} \Gamma_{J_k \rightarrow J'}$$

(we omit here the barrier indexes for ease of notation) with $-2 \leq J_k, J', J_{k+1} \leq 2$ and $|J_{k+1} - J_k| = 1$. It is possible to show that the average time spent in each

state converges, in the asymptotic ($k \to \infty$) limit, to the stationary occupation probability as calculated by solving the master equation 6.4 in the $t \to \infty$. In
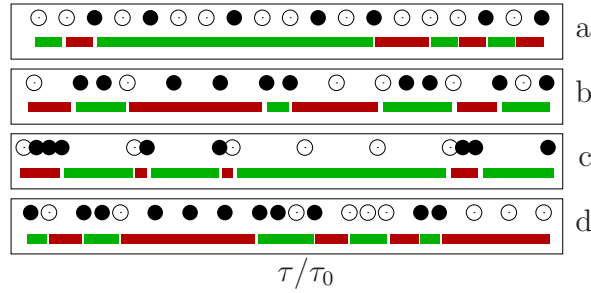
Figure 6.7: Output sequences of a Monte Carlo simulation for tunneling events at junction 2, with $eV = 3E_J$, $N_g = 0.48$, $k_B T = 0.02E_J$ and $\mathcal{A} = 20$. Black (white) dots denote a clockwise (anticlockwise) entering electron. Colored bars are the sequence of the orbital value $|J|$, green: oscillations $0 \to \pm 1 \to 0$; red: oscillations $\pm 2 \to \pm 1 \to \pm 2$; (a) $g = g_\ell = 1$; (b) $g = 0.7$, $g_\ell = 1$; (c) $g = 0.7$, $g_\ell = 0.5$; (d) $g = 0.7$, $g_\ell = 1.2$.

the following, we consider $\mathcal{A} \gg \mathcal{A}_c$, $\Phi = 0$ and $V > 0$ in the 5 states region. Figure 6.7 shows typical outcomes of the simulation, represented as sequences of tunneling events for clockwise (black dots) and anti-clockwise (white dots) electrons tunneling through the input barrier. Since $\tau_1 \ll \tau_{0,2}$, the ring state "oscillates" alternatively around $J = 0$ and $|J| = 2$. The colored bars describe these oscillations: green represents the transitions $0 \to \pm 1 \to 0$, red represents $\pm 2 \to \pm 1 \to \pm 2$. We denote these two sequences as S_0 and S_2. The average time interval between tunneling is τ_0 inside S_0 and τ_2 inside S_2 and. Correspondingly, the average number of transitions in S_0 is $n_0 = (1 + r_1)/r_1$ with an average duration time $T_0 = n_0 \tau_0$, while in S_2 we have $n_2 = (1 + r_1)$ with an average duration time $T_2 = n_2 \tau_2$. It is interesting to notice that T_2 represents the average sequential-tunneling relaxation time of the states $|J| = 2$ [107]. Without interactions, Fig. 6.7 (a), the tunneling events are uniformly distributed since ($\tau_0 = \tau_2$). In the interacting case, the removal of the degeneracy of τ_0 and τ_2 is reflected in a bunching tendency of the tunneling events as can be clearly seen in panels (b,c,d) of Fig. 6.7. The bunching can obviously be present either in S_0 – panels (b,d) – or in S_2 – panel (c). In *all* of these cases we have $F_N > 1$. Quite generally, while with superpoissonian noise we *always* find a bunching of the tunneling events, the converse can be false: if $\mathcal{A} < \mathcal{A}_c$ the bunching might still occur but the interplay of the two barriers with comparable transparency gives rise to negative correlations and a depression of the noise below the Poissonian limit, thus giving $F_N < 1$. The interpretation of F_J is distinctly different (Fig. 6.7 (d)). Here, the time scales $\tau_{0,2}$ do not play any role. The important parameter is the number of events n_2 inside the sequence S_2 in which the ring oscillates around the excited state $J = 2$. The condition $F_J > 1$ is fulfilled only for $n_2 > 2$, *independent of the bunching mechanism*, which in principle could even be absent.

Conclusions

In this thesis, we have investigated the influence of electronic interactions, spin and orbital degrees of freedom in the transport properties of quantum dots and quantum rings created in correlated one-dimensional electron systems. The latter have been described by means of the Luttinger liquid model and the sequential transport regime has been considered by means of a master equation approach. Several important results have been achieved.

The transport properties of a quantum dot are strongly influenced by the presence of the spin degree of freedom and by interactions. In the low-temperature linear transport regime, a spin-induced even-odd effect is found in the conductance peaks position. Increasing the temperature, the peaks positions evolve until equidistant peaks are found. The peaks movement is sensitive to the presence of interacting leads. The conductance peak maxima exhibit a power law scaling as a function of the temperature: in the low temperature regime the exponent is given by the leads interaction parameter only, while in the high temperature regime it gets renormalized by the influence of the interacting quantum dot. In the nonlinear transport regime, an interacting quantum dot shows negative differential conductance (NDC) if an asymmetry in the source and drain tunneling rates develops. Spin-flip relaxation processes and leads interactions tend to deplete the NDC effect: their effect has been analyzed.

In the case of the quantum ring, we have investigated in details the charge and angular current noise in the zero frequency regime. The shot noise of an interacting quantum ring can be driven to super-Poissonian values if tunneling barriers are asymmetric. The angular noise is independent of asymmetry. Both charge and angular noise are sensitive to the presence of interacting leads: the latter in particular can become super-Poissonian only for attractive interactions in the leads. Tuning the external magnetic flux, different transport regimes can be accessed: in an interacting ring, the charge noise exhibits crossover from sub- to super-Poissonian values. An interpretation of the noise in terms of typical transport time scales and bunching of tunneling events has been provided, with the aid of a BKL Monte Carlo simulation.

Thanks. . .

I would like to thank my supervisor, Prof. Dr. Bernhard Kramer, whose help, support and encouragement have been determinant during all my Ph.D.. I am deeply indebted with Prof. Dr. Maura Sassetti, who first of all believed in me and supported my work through many difficulties, teaching me a whole lot of physics in our many endless discussions. During my Ph.D., many friends have been with me: Federico, Alberto, Matteo, Federica, Alessandro, Riccardo, and Eros just to name a few. I would like to thank all the guys in Prof Kramer's group in Hamburg (Alex, Stefan, Stefan, Masayuki, Jun-Ichiro, Kai,. . .) and the people I met at the I. Institut für Theoretische Physik, who made my stay in Hamburg a pleasant experience both scientifically and socially. I would especially like to thank Alex for his precious translation of the abstract. Last, but not least, my parents who enthusiastically encouraged me (and helped me!) to pursue the dream of becoming a Ph.D. and Cristina, who has always been by my side with love and (almost infinite) patience. . .

Dot correlation function

Plugging the quantum dot spectral density (3.31) into (3.32) we obtain $W_{\mathrm{d}}(t) = W_{\mathrm{d}}^{(\rho)}(t) + W_{\mathrm{d}}^{(\sigma)}(t)$

$$W_{\mathrm{d}}^{(\nu)}(t) = \sum_{m_\nu=1}^{\infty} \left\{ \coth\left(\frac{\beta m_\nu \varepsilon_\nu}{2}\right) [1 - \cos(m_\nu \varepsilon_\nu t)] + i\sin(m_\nu \varepsilon_\nu t) \right\} \frac{e^{-m_\nu \varepsilon_\nu / \omega_{\mathrm{c}}}}{2g_\nu m_\nu}. \tag{A.1}$$

After some algebra, we can rewrite $\exp[-W_{\mathrm{d}}(t)]$ as

$$e^{-W_{\mathrm{d}}(t)} = \prod_\nu K_\nu e^{-W_{\nu,+}(t)} e^{-2W_{\nu,0}(t)} e^{-W_{\nu,-}(t)} \tag{A.2}$$

where

$$K_\nu = \left(1 - e^{-\varepsilon_\nu / \omega_{\mathrm{c}}}\right)^{1/2g_\nu} \tag{A.3}$$

and

$$W_{\pm,\nu}(t) = -\frac{1}{2g_\nu} \sum_m \frac{\coth(\beta m_\nu \varepsilon_\nu / 2) \mp 1}{2m} e^{\pm im\varepsilon_\nu t} \tag{A.4}$$

$$W_{0,\nu}(t) = \frac{1}{2g_\nu} \sum_m \frac{1}{m} e^{-m\beta\varepsilon_\nu}. \tag{A.5}$$

Since the charge and spin sectors are completely independent and factorized, in the following I will omit the ν index. The calculation is rather straightforward in the $T \to 0$ limit. In this case, we have $W_0(t) = W_+(t) = 0$ and we are left with

$$e^{-W_-(t)} \equiv \sum_{p=0}^{\infty} \frac{1}{p!} \left[\sum_{m=1}^{\infty} X_m e^{-im\varepsilon t} \right]^p, \quad X_m = \frac{1}{2g} \frac{1}{m}. \tag{A.6}$$

Analyzing (A.6) one realizes that it can be re-grouped exactly as a Fourier expansion:

$$e^{-W_-(t)} = \sum_{p=0}^{\infty} a_p^{(0)} e^{-ip\varepsilon t}. \tag{A.7}$$

In order to obtain the p-th coefficient $a_p^{(0)}$ one has to collect all the terms with an energy $p\varepsilon$ in the exponential. The first five terms read

$$e^{-W_-(t)} = \quad 1 + X_1 e^{i\varepsilon t} + \left[X_2 + \tfrac{1}{2!}X_1^2\right] e^{2i\varepsilon t} + \left[X_3 + \tfrac{1}{2!}2X_1X_2 + \tfrac{1}{3!}X_1^3\right] e^{3i\varepsilon t} \quad \text{(A.8)}$$
$$+ \left[X_4 + \tfrac{1}{2!}\left(2X_1X_3 + X_2^2\right) + \tfrac{1}{3!}3X_1^2X_2 + \tfrac{1}{4!}X_1^4\right] e^{4i\varepsilon t} + \dots .$$

Looking carefully at each term in the expansion some conclusion can be drawn. The p-th term corresponds to the *emission* of collective mode quanta in the dot, whose energy sums up to $p\varepsilon$. Since we are dealing with $T = 0$, only the *emission* of bosons is allowed. Each term has a prefactor whose structure is deeply connected with the integer partitions theory. The k-th *integer partition* of an integer n is defined as the decomposition

$$n = \sum_{i=1}^{l_k} n_i$$

where $0 < n_i \leq n$ are integer numbers. The "length" of the decomposition is represented by l_k. As an example, a possible partition of 7 is $7 = 3 + 2 + 1 + 1$ and has length 4. A closed formula for the number $p(n)$ of partitions of n is not known ,although asymptotic forms and recursive relations can be found [108]. A *Ferrers graph* for the k-th decomposition is a tableau with l_k lines: each n_i entering the decomposition is represented as n_i dots in a line, and the lines are stacked ontop of each other in reverse lexicographic order. The Ferrers graph
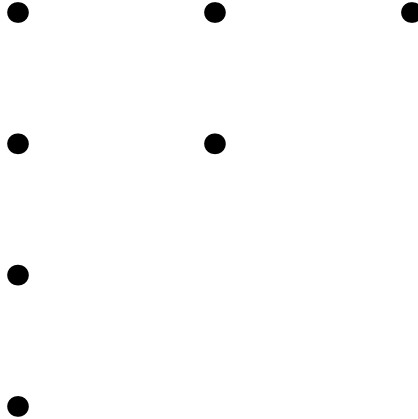
Figure A.1: The Ferrers graph for the partition $7 = 3 + 2 + 1 + 1$.

for the decomposition $7 = 3 + 2 + 1 + 1$ is given in Fig. A. With the aid of the Ferrers graph is easy to generate all the possible partitions for a given integer, thus allowing to generate each term in the coefficients $a_n^{(0)}$. We obtain

$$a_n^{(0)} = \sum_{k=1}^{p(n)} P[\pi_k] \frac{1}{l_k!} \prod_{i=1}^{l_k} X_{n_i} \equiv \sum_{k=1}^{p(n)} P[\pi_k] \frac{1}{l_k!} \left(\frac{1}{2g}\right)^{l_k} \prod_{i=1}^{l_k} \frac{1}{n_i} \quad \text{(A.9)}$$

where $P[\pi_k]$ is the number of possible permutations of the partition π_k. Note that, from a physical point of view, l_k represents the *number of emitted bosons*,

while n_i represents their momentum (in units π/a). The sum over all the partitions (including the corresponding permutations number), thus, takes into consideration all the possible emission sequences at a given energy $n\varepsilon$. Notice, in particular, that the excitation with the highest momentum has the lowest exponent for the term $(2g)^{-1}$ while the excitation with the lowest momentum has the highest exponent. By studying the prefactors for increasing n, it is possible to demonstrate by induction that

$$a_n^{(0)} = \frac{\Gamma(1/2g + n)}{\Gamma(1/2g)\, n!}\theta(n)\,. \tag{A.10}$$

The contribution of the single events is now buried into the rather compact form (A.10). The Fourier expansion of $\exp\left[-W_{\mathrm{d}}(t)\right]$ at zero temperature thus reads

$$e^{-W_{\mathrm{d}}(t)} = \left(1 - e^{-\varepsilon/\omega_{\mathrm{c}}}\right)^{1/2g} \sum_{n=0}^{\infty} a_n^{(0)} e^{-in\varepsilon t} \tag{A.11}$$

Considering the case $T > 0$, the procedure becomes rather cumbersome. In the following, we will consider the limit $k_{\mathrm{B}}T < \varepsilon$ only. We expand $W_\pm(t)$ to the lowest order in $\exp\left[-n\beta\varepsilon\right]$

$$W_+(t) \approx -\frac{1}{2g}\sum_n \frac{e^{-n\beta\varepsilon}}{n}e^{im\varepsilon t}$$

$$W_-(t) \approx -\frac{1}{2g}\sum_n \frac{1 + e^{-n\beta\varepsilon}}{n}e^{-im\varepsilon t}$$

and consider

$$e^{-W_+(t)}e^{-2W_0(t)}e^{-W_-(t)}\,. \tag{A.12}$$

From now on, we will systematically retain the lowest order in temperature, namely $\exp\left[-\beta\varepsilon\right]$, in all the expressions we will consider. This automatically truncates the expansion for the first two exponentials in (A.12)

$$e^{-W_+(t)} \approx 1 + e^{-\beta\varepsilon}X_1 e^{i\varepsilon t}\,, \tag{A.13}$$

$$e^{-2W_0(t)} \approx 1 - 2e^{-\beta\varepsilon}X_1\,. \tag{A.14}$$

The Taylor series for $exp[-W_-(t)]$ is

$$\sum_{q=0}^{\infty}\frac{1}{q!}\left(\frac{1}{2g}\right)^q\left[\sum_{n=1}^{\infty}\frac{1 + e^{-n\beta\varepsilon}}{n}e^{-in\varepsilon t}\right]^q\,, \tag{A.15}$$

thus terms of the form

$$\left(\frac{1}{2g}\right)^{q'}\frac{\left(1 + e^{-n\beta\varepsilon}\right)^{q'}}{n^{q'}}e^{-iq'n\varepsilon t} = X_n^{q'}\left[\sum_{k=0}^{q'}\frac{q'!}{k!(q'-k)!}e^{-\beta n(q'-k)\varepsilon}\right]e^{-inq'\varepsilon t} \tag{A.16}$$

arise. Retaining only the term $\exp\left[-\beta\varepsilon\right]$ one obtains, for $n = 1$,

$$X_1^{q'}\left(1 + q'e^{-\beta\varepsilon}\right)e^{-iq'\varepsilon t}\,, \tag{A.17}$$

while for $n \geq 2$

$$X_n^{q'} e^{-inq'\varepsilon t} , \tag{A.18}$$

Thus, one can formally use the expansion (A.8), replacing $X_1^{q'}$ with (A.18). We obtain

$$\left[1 + e^{-\beta\varepsilon} X_1 e^{i\varepsilon t}\right] \left[1 - 2e^{-\beta\varepsilon} X_1\right] \left[\sum_p a_p^{(0)} e^{-ip\varepsilon t} + e^{-\beta\varepsilon} f(t)\right] \tag{A.19}$$

where $f(t)$ stems from (A.18). Expanding the products, we have

$$\sum_p a_p e^{-ip\varepsilon t} + X_1 e^{-\beta\varepsilon} \left[\sum_p a_p^{(0)} e^{-i(p-1)\varepsilon t} - \sum_p 2a_p^{(0)} e^{-ip\varepsilon t} + \sum_p a_{p-1}^{(0)} e^{-ip\varepsilon t}\right] \tag{A.20}$$

since, exploiting the explicit form of $f(t)$, the term $X_1 f(t)$ reads

$$X_1 f(t) = e^{-i\varepsilon t} + X_1 e^{-2i\varepsilon t} + \left[X_2 + \frac{1}{2!} X_1^2\right] e^{-3i\varepsilon t} + \dots .$$

Therefore, grouping the terms according to the excitation energy, the Fourier expansion at low temperature now reads

$$e^{-W_{\mathrm{d}}(t)} = \left(1 - e^{-\varepsilon/\omega_{\mathrm{c}}}\right)^{1/2g} \sum_{n=-1}^{\infty} a_n e^{-in\varepsilon t} \tag{A.21}$$

where

$$a_n = a_n^{(0)} + \frac{e^{-\beta\varepsilon}}{2g} \left[a_{n+1}^{(0)} + a_{n-1}^{(0)} - 2a_n^{(0)}\right] . \tag{A.22}$$

Two considerations are in order. First off, the sum in (A.22) starts from $n = -1$. Physically it corresponds to a tunneling process which occurs *absorbing* one energy quantum from the collective dot excitations. Secondly, the Fourier weights get renormalized at finite temperature. In particular, it is interesting to notice the term

$$\frac{e^{-\beta\varepsilon}}{2g} \cdot a_{n+1}^{(0)} \equiv a_{-1} a_{n+1}^0$$

which is due to tunneling events which simultaneously absorb one energy quantum from the collective modes, and excite $n + 1$ quanta.

Noninteracting rates steps

We want to calculate the rates steps in the noninteracting case ($g_\rho = g_\sigma \equiv 1$) for the one-dimensional quantum dot. First off, we consider the $T = 0$ case. Since $\varepsilon_\rho = \varepsilon_\sigma \equiv \varepsilon_0$, the rate can be rewritten as

$$\Gamma(\Delta E) = \sum_{q_\rho=0}^{+\infty} \sum_{q_\sigma=0}^{+\infty} a_\rho^{(0)}(q_\rho) a_\sigma^{(0)}(q_\sigma) \gamma(\Delta E - q_\rho \varepsilon_\rho - q_\sigma \varepsilon_\sigma) \equiv \sum_{l=0}^{\infty} A_l^{(0)} \gamma(\Delta E - l\varepsilon_0)$$

with

$$A_l^{(0)} = \sum_{q=0}^{l} a^{(0)}(q) a^{(0)}(l - q), \quad a^{(0)}(q) = a_\rho^{(0)}(q) = a_\sigma^{(0)}(q).$$

After the shift $q = p - l/2$, we have

$$A_l^{(0)} = \frac{1}{\pi} \sum_{p=-\frac{l}{2}}^{\frac{l}{2}} \frac{\Gamma\left[\frac{1}{2} + (p - l/2)\right] \Gamma\left[\frac{1}{2} - (p - l/2)\right]}{\Gamma\left[1 + (p - l/2)\right] \Gamma\left[1 - (p - l/2)\right]} = \sum_{p=-\frac{l}{2}}^{\frac{l}{2}} \frac{\tan\left[\frac{\pi}{2}(l - 2p)\right]}{\frac{\pi}{2}(l - 2p)} = 1$$

where we have used the useful identities [62]

$$\Gamma\left(\frac{1}{2} + ix\right) \Gamma\left(\frac{1}{2} - ix\right) = \frac{\pi}{\cosh(\pi x)}; \quad \Gamma(1 + ix)\Gamma(1 - ix) = \frac{\pi x}{\sinh(\pi x)}.$$

Therefore, the rates exhibit unitary jumps in the $T = 0$, noninteracting, limit. Turning to $0 < k_B T < \varepsilon_0$, we now have

$$\Gamma(\Delta E) = \sum_{l=-1}^{\infty} A_l \gamma(\Delta E - l\varepsilon_0).$$

With the aid aid of Mathematica$^{\text{TM}}$ we find

$$A_l = \sum_{q=-1}^{l+1} a(q) a(l - q) = 1 - 2e^{-\beta\varepsilon_0} + \frac{3}{2} e^{-2\beta\varepsilon_0}, \quad a(q) = a_\rho(q) = a_\sigma(q).$$

if $l \geq 0$, and for $l = -1$

$$A_{-1} = 2a(0)a(-1) = e^{-\beta \varepsilon_0} .$$

Monte Carlo convergence

We want to show that the Monte Carlo algorithm described in section 6.3.3 converges to the stationary occupation probability as calculated from the Master equation (6.4). We define a five-dimensional "state vector" $\mathbf{R}$ whose components

$$\mathbf{R} = \{R_{-2}, R_{-1}, R_0, R_1, R_2\}$$

represent the simulation probability density of the states $J = -2 \ldots 2$. The *evolution matrix* $\mathbf{Q}$ (not to be confused with the transition matrix $\mathbf{M}$ in the master equation) is defined as

$$\mathbf{Q} = \begin{pmatrix} 0 & r & 0 & 0 & 0 \\ 1 & 0 & 1/2 & 0 & 0 \\ 0 & 1-r & 0 & 1-r & 0 \\ 0 & 0 & 1/2 & 0 & 1 \\ 0 & 0 & 0 & r & 0 \end{pmatrix} . \tag{C.1}$$

At each step of the simulation, the matrix $\mathbf{Q}$ represents the transition probabilities among the ring states. Here, we have defined $r = \Gamma^{(1)}_{1 \to 2} / \left(\Gamma^{(1)}_{1 \to 0} + \Gamma^{(1)}_{1 \to 2} \right)$, the conditional probability for the transition $1 \to 2$, $1 - r$ is the conditional probability for the process $1 \to 0$, $1/2$ is the conditional probability for the transitions $0 \to \pm 1$, while 1 represents the forced transition $\pm 2 \to \pm 1$. The simulation evolves from an initial state $\mathbf{R}_0$ according to

$$\mathbf{R}_{k+1} = \mathbf{Q}\mathbf{R}_k . \tag{C.2}$$

Note that, at each step k, it holds

$$R = \mathrm{Tr}\{\mathbf{R}_k\} = \mathrm{Tr}\{\mathbf{R}_0\}$$

so the "evolution" does not affect the normalization of $\mathbf{R}$. We choose an initial condition $\mathbf{R}_0$ so that $R = 1$. For each step of the simulation, to each elementary process is associated an average time scale as shown in table C.1 We treat

Transition	Time scale
$-2 \rightarrow -1$	τ_2
$-1 \rightarrow -2$	τ_1
$-1 \rightarrow 0$	τ_1
$0 \rightarrow -1$	τ_0
$0 \rightarrow 1$	τ_0
$1 \rightarrow 0$	τ_1
$1 \rightarrow 2$	τ_1
$2 \rightarrow 1$	τ_2

Table C.1: Table of the average time scales for the processes involved in the Monte Carlo simulation.

these time scales as a cost function: at each simulation step the ring "pays" an amount of time determined by the occupied state. We introduce a cost matrix **C** defined as

$$C_{JJ'} = \tau_{|J|}\delta_{J,J'}$$

with $-2 \leq J, J' \leq 2$. The vector $\mathbf{f}_k$, whose components represent the total average "cost" up to the k-th simulation step, satisfies the recursive relation

$$\mathbf{f}_{k+1} = \mathbf{f}_k + \mathbf{C}\mathbf{R}_k. \tag{C.3}$$

Physically, the averaged cost $\left(\bar{\mathbf{f}}_k\right)_J = (\mathbf{f}_k)_J / \text{Tr}\{\mathbf{f}_k\}$ simply represents the average time spent in the J-th state. Because of the system ergodicity, in the asymptotic regime $k \rightarrow \infty$, this time simply represents the total occupation probability of the ring states. To show this, we apply the method of the z transform [109]: transforming and combining (C.2) with (C.3), we obtain

$$\tilde{\mathbf{f}}(z) = \frac{1}{z-1}\mathbf{C}\left[\mathbf{1} - \frac{1}{z}\mathbf{Q}\right]^{-1}\mathbf{R}_0$$

which must be anti-transformed. After lengthy but straightforward calculations we finally obtain

$$\lim_{k \rightarrow \infty} \left(\bar{\mathbf{f}}_k\right)_{J=0} = \frac{(1-r)\tau_0}{(1-r)\tau_0 + \tau_1 + r\tau_2} \equiv P_{J=0}$$

$$\lim_{k \rightarrow \infty} \left(\bar{\mathbf{f}}_k\right)_{J=\pm 1} = \frac{1}{2}\frac{\tau_1}{(1-r)\tau_0 + \tau_1 + \tau_2} \equiv P_{J=\pm 1}$$

$$\lim_{k \rightarrow \infty} \left(\bar{\mathbf{f}}_k\right)_{J=\pm 2} = \frac{1}{2}\frac{r\tau_2}{(1-r)\tau_0 + \tau_1 + \tau_2} \equiv P_{J=\pm 2}$$

which correspond to the stationary solution of the 5 states master equation.

Bibliography

[1] R. P. Feynman, Engineering & Science **23**, 22 (1960).

[2] *Intel Pentium Processor Extreme Edition 840*, Intel (2005).

[3] K. von Klitzing, G. Dorda, M. Pepper, Phys. Rev. Lett. **45**, 494 (1980).

[4] D. C. Tsui, H. L. Störmer, A. C. Gossard, Phys. Rev. Lett. **48**, 1559 (1982).

[5] E. Ulrichs, G. Biese, C. Steinbach, C. Schüller, and D. Heitmann, Phys. Rev. B **56**, R12760 (1997).

[6] L. P. Kouwenhoven, D. G. Austing, and S. Tarucha, Rep. Prog. Phys. **64** (2001).

[7] M. A. Kastner, Rev. Mod. Phys. **64** (1992).

[8] O. M. Auslaender, A. Yacoby, R. De Picciotto, K. W. Baldwin, L. N. Pfeiffer, K. W. West, Phys. Rev. Lett. **84** 1764 (2000).

[9] S. J. Tans, M. H. Devoret, H. J. Dai, A. Thess, R. E. Smalley, L. J. Geerligs and C. Dekker, Nature **386**, 474 (1997).

[10] J. Park, A. N. Pasupathy, J. I. Goldsmith, C. Chang, Y. Yaish, J. R. Petta, M. Rinkoski, J. P. Sethna, H. D. Abruña , P. L. McEuen, D. C. Ralph, Nature **417**, 722 (2002).

[11] W. Liang, M. P. Shores, M. Bockrath, J. R. Long, H. Park, Nature **417**, 725 (2002).

[12] Ya. M. Blanter and M. Büttiker Phys. Rep. **336**, 1 (2000).

[13] *Quantum Noise in Mesoscopic Physics*, Ed. Y. V. Nazarov (Nato-ASI 97,Kluwer Academic Publishe, 2003).

[14] J. Voit, Rep. Progr. Phys. **58**, 977 (1995).

[15] D. G. Polyakov, and I. V. Gornyi, Phys. Rev. B **68**, 035421 (2003).

[16] Yu. V. Nazarov, and L. I. Glazman, Phys. Rev. Lett. **91**, 126804 (2003).

[17] F. Cavaliere, A. Braggio, J. T. Stockburger, M. Sassetti, and B. Kramer, Phys. Rev. Lett. **93**, 036803 (2004).

[18] J. U. Kim, I. V. Krive, and J. M. Kinaret, Phys. Rev. Lett. **90**, 176401 (2003).

[19] F. Cavaliere, A. Braggio, M. Sassetti, and B. Kramer, Phys. Rev. B **70**, 125323 (2004).

[20] H. W. Ch. Postma, T. Teepen, Z. Yao, M. Grifoni, and C. Dekker, Science **293**, 76 (2001).

[21] F. Cavaliere, F. Haupt, R. Fazio, and M. Sassetti, Phys. Rev. B *in press*; cond-mat/0412346.

[22] R. Martel, H. R. Shea, and P. Avouris, J. Phys. Chem. B **103**, 7551 (1999).

[23] U. F. Keyser, C. Fühner, S. Borck, R. J. Haug, M. Bichler, G. Abstreiter, and W. Wegscheider, Phys. Rev. Lett. **90**, 196601 (2003).

[24] J. Millman, *Microelectronics*, McGraw-Hill Education - Europe (1987).

[25] H. Bruus, K. Flensberg, *Introduction to Quantum field theory in condensed matter physics* (Lecture notes, Copenhagen, 2001).

[26] B. J. van Wees, H. van Houten, C. W. Beenakker, J. G. Williamson, L. P. Kouwenhoven, D. van der Meer, and C. T. Foxon, Phys. Rev. Lett. **60**, 848 (1988).

[27] R. Landauer, IBM J. Res. Develop. **1**, 223 (1957).

[28] M. Büttiker, Phys. Rev. Lett. **57**, 1761 (1986).

[29] M. Büttiker, IBM J. Res. Develop. **32**, 317 (1988).

[30] C. Dekker, Physics Today, May, **22** (1999).

[31] H. W. Kroto, J. R. Heath, S. C. O'Brien, R. F. Curl and R. E. Smalley, Nature **318**, 162 (1985).

[32] S. Iijima, Nature 354, **56** (1991).

[33] *Carbon nanotubes* ed. by M. S. Dresselhaus, G. Dresselhaus, Ph. Avouris, (Topics in Applied Physics 80, Springer Verlag, Berlin, 2001).

[34] P. R. Wallace, Phys. Rev. **71**, 622 (1946).

[35] J. Kyriakidis, M. P. Ladriere, M. Ciorga, A. S. Sachrajda, and P. Hawrylak, Phys. Rev. B **66**, 035320 (2002).

[36] G. L. Ingold, Yu. V. Nazarov, in *Single Charge Tunneling*, ed. by H. Grabert and M. H. Devoret, (NATO ASI Series B Vol. 294. Plenum Press, New York, 1992).

[37] L. P. Kouwenhoven, N. C. van der Vaart, A. T. Johnson, W. Kool, C.J.P.M. Harmans, J. C. Williamson, A. A. M. Staring, C. T. Foxon, Z. Phys. B **85**, 367 (1991).

[38] T. Fujisawa, D. G. Austing, Y. Tokura, Y. Hirayama, and S. Tarucha, Phys. Rev. Lett. **88**, 236802 (2002).

[39] D. Weinmann, W. Häusler, and B. Kramer, Phys. Rev. Lett. **74**, 984 (1995).

[40] K. Jauregui, W. Husler, D. Weinmann, and B. Kramer, Phys. Rev. B **53**, R1713 (1996).

[41] A.K. Huettel, H. Qin, A.W. Holleitner, R.H. Blick, K. Neumaier, D. Weinmann, K. Eberl, and J.P. Kotthaus, Europhys. Lett. **62**, 712 (2003).

[42] D. Weinmann, *Quantum transport in nanostructures*, Dissertation zur Erlangug des Doktorgrades des Fachbereichs Physik der Universität Hamburg (1994).

[43] L. N. Pfeiffer, H. L. Stormer, K. W. Baldwin, K. W. West, A. R. Goni, A. Pinczuk, R. C. Ashoori, M. M. Dignam, W. J. Wegscheider, Crystal Growth **849**, 127 (1993).

[44] A. Yacoby, H. L. Stormer, Ned S. Wingreen, L. N. K. W. West, Phys. Rev. Lett. **77**, 4612 (1996).

[45] A. Yacoby, H. L. Stormer, K. W. Baldwin, L. N. Pfeiffer, K. W. West, Solid State Commun. **101**, 77 (1997).

[46] C. W. J. Beenaker, Phys.Rev. B **44**, 1646 (1991).

[47] R. Egger, and A. O. Gogolin, Phys. Rev. Lett. **79**, 5082 (1997).

[48] D. Pines, P. Nozieres, *The theory of quantum liquids, Vol. 1*, (W. A. Benjamin Inc, New York, 1966).

[49] A. J. Schofield, Contemporary Physics **40**, 95 (1999).

[50] D. L. Goodstein, *States of matter*, (Dover, 1985).

[51] L. D. Landau, *Sov. Phys. JETP* **3**, 920 (1957); L. D. Landau, *Sov. Phys. JETP* **5**, 101 (1957); L. D. Landau, *Sov. Phys. JETP* **8**, 70 (1958).

[52] S. Tomonaga, Prog. Theor. Phys. **5**, 544 (1950).

[53] J. M. Luttinger, J. Math. Phys. **4**, 1154 (1963).

[54] F. D. M. Haldane, J. Phys. C **14**, 2585 (1981).

[55] T. Giamarchi, *Quantum Physics in One Dimension* (Oxford University Press, 2004).

[56] R. de L. Kronig, Physica **2**, 968 (1935).

[57] A. S. Davydov, *Quantum Mechanics* (Addison-Wesley, Reading, MA, 1965).

[58] J. Lee, S. Eggert, H. Kim, S.-J. Kahng, H. Shinohara, and Y. Kuk, Phys. Rev. Lett. **93**, 166403 (2004).

[59] O. M. Auslaender, A. Yacoby, R. de Picciotto, K. W. Baldwin, L. N. Pfeiffer, K. W. West, Science **295**, 825 (2002).

[60] Y. Tserkovnyak, B. I. Halperin, O. M. Auslaender, and A. Yacoby, Phys. Rev. Lett. **89**, 136805 (2002).

[61] O. M. Auslaender, H. Steinberg, A. Yacoby, Y. Tserkovnyak, B. I. Halperin, K. W. Baldwin, L. N. Pfeiffer, and K. W. West, Science **308**, 88 (2005).

[62] "Handbook of mathematical functions with Formulas, Graphs and Mathematical Tables", Ed. by M. Abramowitz, and I. A. Stegun, Dover Publications, Inc., New York (1964).

[63] M. Fabrizio, and A. O. Gogolin, Phys. Rev. B **51**, 17827 (1995).

[64] A. E. Mattsson, S. Eggert, and H. Johannesson, Phys. Rev. B **56**, 15615 (1997).

[65] J. Voit, Y. Wang, and M. Grioni, Phys. Rev. B **61**, 7930 (2000).

[66] A. Braggio, M. Sassetti, and B. Kramer, Phys. Rev. Lett. **87**, 146802 (2001).

[67] T. Kleimann, F. Cavaliere, M. Sassetti, and B. Kramer, Phys. Rev. B. **66**, 165311 (2002).

[68] A. Furusaki, Phys. Rev. B **57**, 7141 (1998).

[69] A. V. Khaetskii and Yu. V. Nazarov, Phys. Rev. B **61**, 12639 (2000); A.V. Khaetskii, Yu.V. Nazarov, Phys. Rev. B **64**, 125316 (2001).

[70] J. Fabian, S. Das Sarma, J. Vac. Sci. Technol. B. **17**, 1708 (1999).

[71] A. Braggio, M. Grifoni, M. Sassetti, and F. Napoli, Europhys. Lett. **50**, 236 (2000).

[72] J. U. Kim, J. M. Kinaret, M. -S. Choi, cond-mat/0403613 (2004).

[73] A. Braggio, R. Fazio, and M. Sassetti, Phys. Rev. B **67**, 233308 (2003).

[74] D. H. Cobden, M. Bockrath, P. L. McEuen, A. G. Rinzler, R. E. Smalley, Phys. Rev. Lett. **81**, 681 (1998).

[75] D. H. Cobden, J. Nygård, Phys. Rev. Lett. **89**, 046803 (2002).

[76] S. Tarucha, D. G. Austin, T. Honda,R. J. van der Hage, L. P. Kouwenhoven, Phys. Rev. Lett. **77**, 3613 (1996).

[77] E. Bonet, M. M. Deshmukh, and D. C. Ralph, Phys. Rev. B **65**, 045317 (2002).

[78] G. Usaj, and H. U. Baranger, Phys. Rev. B **64**, 201319 (2001).

[79] T. Kleimann, M. Sassetti, B. Kramer, and A. Yacoby, Phys. Rev. B **62**, 8144 (2000).

[80] H. W. Schumacher, U. F. Keyser, U. Zeitler, R. J. Haug, and K. Eberl, Appl. Phys. Lett. **75**, 1107 (1999).

[81] A. van der Ziel, *Noise* (Chapman and Hall, London, 1955).

[82] L. Saminadayar, D. C. Glattli, Y. Jin, and B. Etienne, Phys. Rev. Lett. **79**, 2526 (1997); R. de Picciotto, M. Reznikov, M. Heiblum, V. Umansky, G. Bunin and D. Mahalu, Nature (London) **389**, 162 (1997).

[83] W. Schottky, Ann. Phys. (Leipzig) **57**, 541 (1918).

[84] J. B. Johnson, Phys. Rev. **29**, 367 (1927).

[85] H. Nyquist, Phys. Rev. **32**, 110 (1928).

[86] W. D. Oliver, "The generation and detection of electron entanglement" - Ph. D. dissertation (2003).

[87] R. Hanbury Brown, and R. Q. Twiss, Nature **177**, 27 (1956); R. Hanbury Brown, and R. Q. Twiss, Nature **178**, 1046 (1958); E. Purcell, Nature **178**, 1449 (1958).

[88] C. Santori, M. Pelton, G. Solomon, Y. Dale, and Y. Tamamoto, Phys. Rev. Lett. **86**, 1502 (2001).

[89] W. D. Oliver, J. Kim, R. C. Liu, and Y. Yamamoto, Science **284**, 299 (1999).

[90] M. Henny, S. Oberholzer, C. Strunk, T. Heinzel, K. Ensslin, M. Holland, and C. Schönenberger, Science **284**, 296 (1999).

[91] S. Hershfield, J. H. Davies, P. Hyldgaard, C. J. Stanton, and J. W. Wilkins, Phys. Rev. B **47**, 1967 (1993).

[92] A. N. Korotkov, Phys. Rev. B **49**, 10381 (1994).

[93] U. Hanke, Yu. M. Galperin, K. A. Chao, and N. Zou, Phys. Rev. B **48**, 17209 (1993).

[94] H. Birk, M. J. M. de Jong, and C. Schönenberger, Phys. Rev. Lett. **75**, 1610 (1995).

[95] G. Iannaccone, G. Lombardi, M. Macucci, and B. Pellegrini, Phys. Rev. Lett. **80**, 1054 (1998).

[96] Ya. M. Blanter, M. Buttiker, Phys. Rev. B. **59**, 10543 (1999).

[97] S. S. Safonov, A. K. Savchenko, D. A. Bagrets, O. N. Jouravlev, Yu. N. Nazarov, E. H. Linfield, and D. A. Ritchie, Phys. Rev. Lett. **91**, 136803 (2003).

[98] A. Nauen, F. Hohls, J. Koenemann, and R. J. Haug, Phys. Rev. B **69**, 113316 (2004).

[99] A. Cottet, W. Belzig, and C. Bruder, Phys. Rev. Lett. **92**, 206801 (2004).

[100] A. Cottet, and W. Belzig, Europhys. Lett. **66**, 405 (2004).

[101] O. Sauret, and D. Feinberg, Phys. Rev. Lett. **92**, 106601 (2004).

[102] A. Thielmann, M. H. Hettler, J. König, and G. Schön, Phys. Rev. B **71**, 045341 (2005).

[103] J. M. Kinaret, M. Jonson, R. I. Shekhter, and S. Eggert, Phys. Rev. B **57**, 3777 (1998).

[104] D. A. Bagrets and Yu. V. Nazarov, Phys. Rev. B **67**, 085316 (2003).

[105] M. Galassi *et al.*, GNU Scientific Library Reference Manual (2nd Ed.), ISBN 0954161734.

[106] A.B. Bortz, M.H. Kalos, and J.L. Lebowitz, J. Comput. Phys. **17**, 10 (1975).

[107] X. Waintal, and P. W. Brouwer, Phys. Rev. Lett. **91**, 247201 (2003).

[108] Norman L. Biggs, *Discrete mathematics* (Oxford Science Publications, 1985).

[109] E. I. Jury, *Theory and Applications of the Z-Transform Method* (Wiley, New York) (1964).

During my Ph.D. I have been co-author of 10 publications

6 papers published on international reviews

- T. Kleimann, F. Cavaliere, M. Sassetti, and B. Kramer,
  Theory of measuring the Luttinger g of a one-dimensional quantum dot,
  Phys. Rev. B **66**, 165311 (2002);

- F. Cavaliere, A. Braggio, J. T. Stockburger, M. Sassetti, and B. Kramer,
  Negative Differential Conductance Induced by Spin-Charge Separation,
  Phys. Rev. Lett. **93**, 036803 (2004);

- F. Cavaliere, A. Braggio, M. Sassetti, and B. Kramer,
  Spin effects in transport through non-Fermi-liquid quantum dots,
  Phys. Rev. B **70**, 125323 (2004);

- M. Sassetti, F. Cavaliere, and B, Kramer,
  Transport properties of quantum wires,
  Solid State Commun. **131**, 647 (2004);

- B. Kramer, K. Dittmer, S. Debald, J. Ohe, F. Cavaliere, and M. Sassetti,
  Spin transport through nanostructures,
  Materials Science (Poland) **22**, 445 (2004);

- F. Cavaliere, F. Haupt, R. Fazio, and M. Sassetti,
  Shot noise in charge and magnetization currents of a quantum ring,
  Phys. Rev. B *in press*; cond-mat/0412346;

3 book chapters written upon invitation

- M. Sassetti, A. Braggio, F. Cavaliere, T. Kleimann, and B. Kramer,
  Electron Transport in Quantum Wires,
  in the proceedings of the International School of Physics "Enrico Fermi",
  "Quantum Phenomena in Mesoscopic Systems", Course **CLI**, p. 249, B. Altshuler; V. Tognetti Eds., IOS press (2003);

- M. Sassetti, A. Braggio, and F. Cavaliere,
  Spin transport properties of a quantum dot,
  in "*The Anderson Transition and its Ramifications - Disorder, Phase Coherence, and Electron Interactions*", Lecture Notes in Physics, Vol. **630**, p. 259, T. Brandes; S. Ketteman Eds., Springer Verlag, Berlin (2004);

- A. Braggio, F. Cavaliere, M. Sassetti and B. Kramer,
  Correlations and spin in transport through quantum dots,
  in *"Fundamental Problems of Mesoscopic Physics Interactions and Decoherence"*, Proceedings of the NATO Advanced Research Workshop, held in Granada, Spain, 6-12 September 2003. Series : NATO Science Series II: Mathematics, Physics and Chemistry, Vol. **154**, I. V. Lerner; B. L. Altshuler; Yu. Gefen Eds., (2004);

1 conference proceeding contribution (with referral)

- A. Braggio, F. Cavaliere, M. Sassetti and B. Kramer,
  Spin transport in quantum dots: effects of non-Fermi liquid correlations,
  in the Proceedings of the "26th International Conference on the Physics of Semiconductors, Edinburgh 2002", J. Davies, and A. Long Eds., Institute of Physics Publishing, University of Glasgow, UK (2003);

List of Figures

Contents